Mapping Melt Pond Bathymetry on Arctic Sea Ice by Means of Optical Remote Sensing

Dissertation

zur Erlangung des Doktorgrades
der Mathematisch-Naturwissenschaftlichen Fakultät
der Christian-Albrechts-Universität zu Kiel

vorgelegt von

Marcel König

Kiel, 2021

Erste Gutachterin: Prof. Dr. Natascha Oppelt

Zweiter Gutachter: Dr. Peter Gege

Termin der mündlichen Prüfung: 30. April 2021

Zum Druck genehmigt: 30. April 2021

gez. Prof. Dr. Frank Kempken, Dekan

Acknowledgments

At this point I would like to thank everybody who contributed to finalizing this dissertation in one way or another.

First and foremost, I thank my adviser Natascha Oppelt for her trust in my work, her patience, constant support, constructive feedback and discussions, and the opportunity to participate in this adventure.

Peter Gege, thank you for the scientific advice, your patience and support on the Arctic sea ice and on the telephone. Just like on our trip to the Alps, you were a great help in climbing this mountain, and one of the best bunkmates.

To my doctor-brother Niels Fuchs, thank you for the great times. You are one of the best bunkmates and I am looking forward to our next cruises with Polarstern or Nobile. PS115.2 would have been a disaster without you, Heike and the Sea Shepherds.

To my co-authors, thank you Martin Hieronymi for pushing me into the first publication and for loud laughter in the lab, and Gerit Birnbaum for believing in the Aisa and all the hours you spent in the helicopter.

I also thank all colleagues and friends I was happy to share some time with at the EOM lab: Katja Kuhwald and Florian Uhl, who paved my way into research, Felix Linhardt and Mingfeng Wang, who share the fascination for the Arctic, Sebastian Riedel, Alireza Taravat and all the student assistants. You guys made the late shifts easy for me. Cheers to Matthias Wagner, I am glad we shared the four years in Kiel.

I would also like to thank all my friends, colleagues and staff at the Department of Geography, and especially Sinja Dittmann, Claudia Wolff, Philipp Saggau, Frauke Lindenstruth, Jonas Hein, Silja Klepp, Jörn Fleischmann, Alan Haberland, Lars Michelsen, Antje Berger and Julia Becker. A special thanks to Joshua Kiesel, for constructive coffee breaks, inspiring walks, and for sharing anger, frustration, fascination and motivation.

I thank all friends, colleagues and the crews of PS106 and 115.2 who made these research cruises unforgettable experiences.

Thanks to Birgit Heim from AWI Potsdam for providing remote access to ATCOR-4, Rüdiger Röttgers from HZG for helping with the water analytics, and Sebastian Rößler for assistance with the Aisa data. A very special thanks to Jan-Henrik Perplies: If there was a PhD in customs, you would deserve it!

I would also like to thank Kiel University Library, Graduate Center and ISOS for financial supports and the repertoire of helpful courses. Special thanks to Avan Antia for always having an open ear and keeping things running. You are doing a great job!

To all my friends who have supported me over the years and to my family: Mama, Papa and Pascal, Oma Maja and Opa Bruno, Rainer and Claudia, and everyone from the König and Herges families. Thank you for your love, support and believing in me - you made me achieve this.

Finally, thank you Theresa. You have always been my bastion of calm and I would have never achieved this without you!

Abstract

The last decades saw an increasingly rapid decrease of Arctic sea ice with associated consequences for the climate, ecosystems and human activities on local, regional and global scales. The magnitude of sea ice loss observed exceeded predictions of sea ice and climate models. This deficiency and disagreements between different model outputs indicate that some sea ice processes are not yet entirely understood. Improving our understanding of how the Arctic sea ice changes requires regular, intercomparable large-scale observations of essential sea ice parameters, which are only possible by means of remote sensing. One of the main drivers of Arctic sea ice loss is the ice-albedo-feedback mechanism which is strongly influenced by the presence and evolution of melt ponds. Contemporary remote sensing products quantify melt ponds almost exclusively in terms of coverage. A comprehensive understanding of the spatio-temporal evolution of melt ponds, however, also requires monitoring of pond depth, which is an important parameter in sea ice models.

This thesis presents a new method to derive the depth of melt ponds on Arctic sea ice by means of optical remote sensing and is based on a uniquely comprehensive dataset of field based observations and remote sensing data. Firstly, a new method to retrieve melt pond depth from optical field data with unprecedented accuracy is presented. The newly developed method rests upon the log-scaled remote sensing reflectance at 710 nm as a function of depth, is largely independent from bottom albedo, and addresses varying sun zenith angles, making it particularly suitable for remote sensing applications. Secondly, the new method is applied to atmospherically corrected hyperspectral airborne imagery to map two-dimensional melt pond bathymetry. Retrieved bathymetries are in good agreement with field observations and confirm the method's large independence from bottom albedo but results indicate that precise atmospheric correction is a challenge in the Arctic sea ice environment. Thirdly, five different atmospheric correction algorithms for satellite imagery are compared for their applicability over Arctic sea ice using the example of Sentinel-2 data. Comparisons with field data question the suitability of most algorithms for application in this environment in their current state but we found potential for further development.

Findings of the dissertation indicate that the new method enables accurately mapping the bathymetry of melt ponds on Arctic sea ice from hyperspectral remote sensing data with subject to precise atmospheric correction. This thesis may serve as a first step towards an operational remote sensing-based monitoring of melt pond depth on Arctic sea ice.

Kurzfassung

Der Rückgang des arktischen Meereises hat sich in den letzten Jahrzehnten beschleunigt, mit Folgen für das Klima, Ökosysteme und menschliche Aktivitäten auf lokaler, regionaler und globaler Ebene. Dabei überstieg das Ausmaß die Vorhersagen von Meereis- und Klimamodellen. Dies und Unstimmigkeiten zwischen Modellergebnissen zeigen, dass einige Meereisprozesse noch nicht vollständig verstanden sind. Um unser Verständis des sich verändernden arktischen Meereises zu verbessern, bedarf es regelmäßiger, vergleichbarer großräumiger Beobachtungen wesentlicher Meereisparameter, die nur mit Hilfe von Fernerkundung möglich sind. Einer der Haupttreiber des Meereisverlustes ist der Eis-Albedo-Feedbackmechanismus, der stark durch Schmelztümpel beeinflusst wird. Bisher quantifizieren Fernerkundungsprodukte Schmelztümpel fast ausschließlich in Bezug auf ihre Fläche oder Form. Ein umfassendes Verständnis ihrer räumlich-zeitlichen Entwicklung erfordert jedoch auch Beobachtungen der Tümpeltiefe, die ein wichtiger Parameter in Meereismodellen ist.

Diese Arbeit stellt eine neue Methode zur Ableitung der Tiefe von Schmelztümpeln auf dem arktischen Meereis mittels Fernerkundung vor und basiert auf einem einzigartig umfassenden Datensatz aus Feld- und Fernerkundungsdaten. Zunächst wird eine neue Methode zur Ableitung der Schmelztümpeltiefe aus optischen Daten vorgestellt. Die Methode basiert auf der logarithmierten Remote Sensing Reflectance bei 710 nm als Funktion der Tiefe, ist weitgehend unabhängig von der Albedo des Tümpelbodens und berücksichtigt Veränderungen des Sonnenzenithwinkels, weshalb sie besonders gut für Fernerkundungsanwendungen geeignet ist. Im Anschluss wird die neue Methode auf atmosphärenkorrigierte hyperspektrale Luftbilder angewendet, um die Bathymetrie von Schmelztümpeln zu kartieren. Die Ergebnisse stimmen gut mit Feldbeobachtungen überein und bestätigen die weitgehende Unabhängigkeit der Methode von der Bodenalbedo, zeigen allerdings auch, dass eine präzise Atmosphärenkorrektur im arktischen Meereis eine Herausforderung darstellt. Danach werden am Beispiel von Sentinel-2 Daten fünf Atmosphärenkorrekturen für Satellitendaten auf ihre Anwendbarkeit über arktischem Meereis untersucht. Vergleiche mit Felddaten stellen die Eignung der meisten Algorithmen in ihrem jetzigen Zustand für die Anwendung in dieser Umgebung in Frage, jedoch gibt es auch Potenzial für Weiterentwicklungen.

Die Ergebnisse der Dissertation zeigen, dass die neu entwickelte Methode bei präziser Atmosphärenkorrektur eine genaue Kartierung der Bathymetrie von Schmelztümpeln auf dem arktischen Meereis mit hyperspektralen Fernerkundungsdaten ermöglicht. Diese Arbeit ist ein möglicher erster Schritt hin zu einem operationellen fernerkundungsbasierten Monitoring der Tiefe von Schmelztümpeln auf dem arktischen Meereis.

Contents

List of Figures

List of Tables

List of Acronyms

AC atmospheric correction

ANN artificial neural network

AOP apparent optical property

AOT aerosol optical thickness

ATCOR Atmospheric and Topographic Correction

ATLAS Advanced Topographic Laser Altimeter System

ATM Airborne Topographic Mapping

AVHRR Advanced Visible High Resolution Radiometer

BOA bottom of atmosphere

BRDF bidirectional reflectance distribution function

CCD charge-coupled device

CDOM colored dissolved organic matter

CHIME Copernicus Hyperspectral Imaging Mission for the Environment

Chl-a chlorophyll-a concentration

CHRIS Compact High Resolution Imaging Spectrometer

DEM digital elevation model

EnMAP Environmental Mapping and Analysis Program

ENVI Exelis Visual Information Solutions Inc.

EOM Earth Observation and Modelling Lab

ESA European Space Agency

ETM+ Enhanced Thematic Mapper

FODIS Fiber Optic Downwelling Irradiance Sensor

FOV field of view

FWHM full width half-maximum

FYI	first-year ice
GCM	global climate model
GLT	geographic lookup table
GNSS	Global Navigation Satellite System
GPS	Global Positioning System
HICO	Hyperspectral Imager for the Coastal Ocean
HISUI	Hyperspectral Imager SUIte
HySI	HYperspectral Short-wave Infrared radiometer
HyspIRI	Hyperspectral InfraRed Imager
HypXIM	Hyperspectral X IMagery
ICESat	Ice, Cloud and Land Elevation Satellite
IMU	inertial measurement unit
IOP	inherent optical property
L7	Landsat 7
L8	Landsat 8
LFI	landfast ice
LiDAR	light detection and ranging
LST	local solar time
LUT	look up table
MAE	mean absolute error
MERIS	Medium Resolution Imaging Spectrometer
MESMA	multiple endmember spectral unmixing
MIZMAS	Marginal Ice-Zone Modeling and Assimilation System
MODIS	Moderate Resolution Imaging Spectroradiometer
MODTRAN	Moderate Resolution Atmospheric Radiance and Transmittance Model
MOSAiC	Multidisciplinary drifting Observatory for the Study of Arctic Climate
MPF	melt pond fraction
MSI	MultiSpectral Instrument
MSS	Multispectral Scanner System
MYI	multi-year ice

NASA	National Aeronautics and Space Administration
NDMI	normalized difference melt index
NIR	near-infrared wavelength region of the electromagnetic spectrum
NTM	national technical means of verification
OIB	Operation IceBridge
OLCI	Ocean and Land Colour Instrument
OLI	Operational Land Imager
PAR	photosynthetically active radiation
PBIAS	percentage bias
PCA	principal component analysis
PRISMA	PRecursore IperSpettrale della Missione Applicativa
PSU	Practical Salinity Unit
RGB	red-green-blue color space
RMSE	root mean squared error
RMSD	root mean squared difference
ROI	region of interest
ROV	remotely operated vehicle
RV	research vessel
S-2	Sentinel-2
S-3	Sentinel-3
SAR	synthetic aperture radar
SeaWiFS	Seaviewing Wide Field-of-view Sensor
SHALOM	Space-borne Hyperspectral Applicative Land and Ocean Mission
SHEBA	Surface Heat Budget of the Arctic Ocean
SIMEC	SIMilarity Environment Correction
SMOS	Soil Moisture and Ocean Salinity
SNAP	Sentinel Application Platform
SNR	signal-to-noise ratio
SOS	Successive Order of Scattering
SPEAR	Spectral Processing Exploitation and Analysis Resource

SWIR short-wave infrared wavelength region of the electromagnetic spectrum

SYI second-year ice

SZA sun zenith angle

THOR Tactical Hyperspectral Operations Resource

TOA top of atmosphere

UAV unmanned aerial vehicle

UTC Coordinated Universal Time

VIS visible wavelength region of the electromagnetic spectrum

VZA view zenith angle

WASI Water Color Simulator

WV water vapor

6SV Second Simulation of a Satellite Signal in the Solar Spectrum-Vector

Chapter 1

Introduction

The Arctic sea ice is an important feature of the Earth system. It plays a critical role in the Earth's climate system and is a key indicator of the state of global climate, as it is both sensitive to warming and plays a role in amplifying climate change (Maslowski et al., 2012). The Arctic sea ice cover is cooling the northern polar region by reflecting a great portion of incoming solar radiation back into space. It regulates exchanges of momentum, heat, and moisture between ocean and atmosphere (Stroeve and Notz, 2018) and influences wind systems, weather patterns and ocean currents on a global scale (Olsen et al., 2011; Vihma, 2014). Covering a great portion of the northern hemisphere, the Arctic sea ice is one of the Earth's most extensive biomes (Arrigo, 2014) hosting a food web of specialized species, ranging from primary producers such as micro algae and bacteria to top predators such as fish, birds, seals, whales, and polar bears, that are critically depending on the ice cover (Shokr and Sinha, 2015, p. 17). The presence of sea ice further affects the livelihood, culture and identity of indigenous and non-indigenous people and regulates human activities such as resource extraction, shipping and tourism in the Arctic Ocean (Olsen et al., 2011).

The Arctic sea ice is an extremely dynamic environment. Its spatio-temporal distribution in the northern hemisphere is seasonally variable with extents ranging from ~ 4 million km^2 in September to ~ 15 million km^2 in March (Thomas et al., 2019). Moreover, the sea ice coverage is regionally governed by land masses, local climate and ocean currents (Horner et al., 1992, p. 417).

During the last few decades the Arctic has warmed considerably faster than the rest of the globe (Stroeve and Notz, 2018), a phenomenon known as Arctic amplification, which is directly related to a rapid decline in Arctic sea ice (Dai et al., 2019) with "far-reaching consequences for climate, ecology and human activities alike" (Notz and Stroeve, 2016).

Since the beginning of satellite observations, the extent of summer Arctic sea ice has almost halved (Notz and Stroeve, 2018), with an increasing rate of decline now being 13.1 % per decade, relative to the 1981 to 2010 average (National Snow & Ice Data Center, 2020a). This trend is emphasized by the recent records of the five lowest sea ice minimum extents in 2007, 2012, 2016, 2019, and 2020 (National Snow & Ice Data Center, 2020b). The loss of winter sea ice extent is less pronounced but has also accelerated from 2.4 % per decade in the period of 1979 to 1999 to 3.4 % per decade after 2000 (Stroeve and Notz, 2018).

One driver of sea ice loss is a lengthening of the melt season (Landy et al., 2015). Stroeve and Notz (2018) assessed that for the Arctic as a whole the melt season has extended by 40 days over the the last 40 years. In addition to the decline in Arctic sea ice extent, the ice is also getting thinner, which is associated with a rapid loss of old multi-year ice (MYI) and an increasing proportion of first-year ice (FYI) in the total ice cover (Nghiem et al., 2007; Maslanik et al., 2007; Comiso, 2012). MYI now covers less than one-third of the Arctic Ocean (Kwok, 2018), with the fraction of winter sea ice older than five years in April shrinking from 30 % in 1984 to only 2 % in 2018 (Stroeve and Notz, 2018). The loss of old MYI and the increasing proportion of FYI in the total ice cover has resulted in reduced surface roughness, a thinner snow cover and increased melt pond coverage (Nicolaus et al., 2012). The associated effects resulted in a 16 % increase in solar heat input between 2003 and 2008, which is ten times the contribution of earlier melt onset over the same period (Landy et al., 2015).

One of the main drivers of Arctic sea ice melt is the ice-albedo feedback mechanism that strongly influences the heat and mass balance of the ice and upper ocean (Pithan and Mauritsen, 2014). Surface melt reduces the albedo of sea ice, i.e., it increases the absorption of solar radiation, which causes heating and further enhances ice melt (Curry et al., 1995). This positive feedback is one of the reasons for the strong reaction of the Arctic to a rise in global mean temperature and the accelerated warming compared to other regions (Stroeve and Notz, 2018).

An important driver of the ice-albedo feedback mechanism is the formation and evolution of melt ponds that substantially affect the heat and mass balance of Arctic sea ice (Taylor, 2004). Melt ponds have a considerably lower albedo than snow and ice, resulting in increased absorption and transmission of solar radiation (e.g. Perovich et al., 2002; Light et al., 2008; Nicolaus et al., 2012). Absorption of solar radiation and associated heating of pond water enhances melt rates beneath ponds by a factor of 2–3 compared to bare ice (Fetterer and Untersteiner, 1998). Transmitted solar radiation causes heating of the upper ocean layer facilitating bottom and lateral ice melt (Inoue et al., 2008b; Itoh et al., 2011). The presence of melt ponds increases transmittance of photosynthetically active radiation (PAR) through the ice up to a factor of ~ 4 (Arrigo et al., 2012; Light et al., 2015; Nicolaus et al., 2012; Ehn et al., 2011; Itoh et al., 2011), which enables massive phytoplankton blooms under Arctic sea ice (Arrigo et al., 2012; Horvat et al., 2017), thus, having a significant impact on the Arctic ecosystem (Frey et al., 2011).

Sea ice models and global climate models (GCMs) underestimate the decline of the September Arctic sea ice minimum extent, which can be explained by a lack of understanding regarding physical sea ice processes and parameters. One of the largest uncertainties is the understanding and representation of the spatio-temporal behavior of melt ponds (e.g., Stroeve et al., 2007; Flocco et al., 2012).

1.1 Melt ponds on Arctic sea ice

The seasonal evolution of Arctic sea ice is characterized by profound changes of its physical state that manifest in the formation and evolution of melt ponds during Arctic summer (e.g., Perovich, 2002). Melt ponds are dynamic sea ice features that exhibit a considerable spatio-temporal variability. Due to their strong influence on the sea ice energy balance and the associated consequences, melt ponds are an important parameter in sea ice and climate models and their monitoring is subject to numerous remote sensing studies.

1.1.1 Dynamics

The spatio-temporal evolution of melt ponds is influenced by numerous parameters. When referring to the onset of melt as the starting point, these can be separated in preexisting parameters that shape the boundary conditions of melt pond evolution, and environmental parameters that define how ponds evolve over the melt season.

The spatial distribution and evolution of melt ponds is governed by the preexisting topographic relief of the ice defined by deformation and aging processes (Eicken et al., 2004) that control snow depth distribution (Sturm, 2002), lateral pond spreading, and ice permeability (Polashenski et al., 2012; Webster et al., 2015). These parameters explain the different appearance of melt ponds on different ice types.

Snow depth distribution controls the local availability of melt water and is strongly influenced by ice surface topography. The pre-existent hummocky topographic relief of MYI traps drifting snow in troughs between ridges and hummocks, thereby favoring a variable snow cover (Sturm et al., 2000). Deformed FYI may also effectively trap drifting snow but the majority of FYI is undeformed, facilitating a rather homogeneous snow depth distribution (Sturm, 2002) characterized by the formation of rift beds and snow dunes (Petrich et al., 2012; Webster et al., 2015).

After melt onset the evolution of melt ponds is controlled by surface topography and sea ice permeability. Melt water collects at the deepest point of the local topography, where the permeability of ice is smaller than the inflow rate of melt water, and outflow pathways are limited (Polashenski et al., 2012). MYI is characterized by a low permeability that retains melt water at the ice surface and its comparably rough surface topography limits lateral pond spreading (Webster et al., 2015). Permeability of FYI is higher than that of MYI and the low surface relief of undeformed FYI enables lateral spreading of melt water around snow rift bed forms, which determine melt water distribution during pond formation. Where melt water covers the ice surface, higher ablation rates shape the ice surface topography and define subsequent spatial pond evolution (Petrich et al., 2012), which causes the development of a hummocky topography over the melt season (Scharien and Yackel, 2005).

The morphology of melt ponds, i.e., their size, shape, coverage and depth, is controlled by local topography and may range between less than one and ten-thousands of m^2 covering large areas or forming complex networks (e.g., Hohenegger et al., 2012; Wright et al., 2020). As a consequence of the described dependencies, melt ponds on MYI are usually smaller and deeper than on FYI, commonly covering less than 40 % of the ice surface (Nicolaus et al., 2012) with terminal depths mostly less than 1.0 m (Untersteiner, 1961). The smooth surface relief of undeformed FYI in contrast facilitates the formation of extensive shallow melt ponds that may cover up to 80 % (Nicolaus et al., 2012; Fetterer and Untersteiner, 1998), 90 % (Perovich et al., 2011), or even 95 % (Holt and Digby, 1985) of the ice surface at the beginning of the melt period, with depths mostly shallower than 50 cm (Morassutti and Ledrew, 1996; Yackel et al., 2000). In contrast to drifting pack ice, landfast ice (LFI) that is attached to the coast or the seafloor may be exposed to mechanical forces, such as wind, waves, and tides, causing strong deformation. The amount of deformation controls snow depth variability and earlier freeze-up of LFI prolongs the period for snow accumulation and metamorphism compared to drifting pack ice, which affects local availability of melt water and melt pond characteristics (Webster et al., 2015). The loss of old MYI accompanied by the increasing fraction of FYI and reduction of sea ice residence time in the Arctic Ocean facilitates increasing melt pond coverage, which results in a large-scale decrease of sea ice albedo (Eicken et al., 2004). Recent observations of Wright et al. (2020), however, indicate that the relationship between ponding and ice type is more complex than previously thought. Figures 1.1 and 1.2 illustrate melt pond variability on FYI and MYI.

The seasonal evolution of melt ponds on sea ice can be divided into the four general stages: (1) formation, (2) drainage, (3) persistence, and (4) refreezing (Eicken, 2002; Polashenski et al., 2012). When air temperatures exceed 0 °C the overlaying snow covering the Arctic sea ice begins to melt. Following the law of gravity, meltwater accumulates in local depressions on relatively impermeable ice, rapidly floods the overlaying snow and forms visible pools then referred to as melt ponds (Eicken et al., 2004; Scharien and Yackel, 2005; Polashenski et al., 2012). Melt ponds at this stage form above sea level and may cover significant fractions of the sea ice surface (Polashenski et al., 2012). Because this stage coincides with peak input of solar energy over wide areas of the Arctic, its duration can strongly impact the seasonal energy balance (Polashenski et al., 2012). In the second stage percolation of water through the ice (Eicken, 2002) as well as horizontal transport and outflow through macroscopic flaws (Scharien and Yackel, 2005) leads to increased drainage of water and pond surfaces drop close to sea level, resulting in a decrease in pond coverage. In the third stage pond surfaces remain near sea level as ponds are connected to the ocean underneath and outflow pathways are no longer limiting. Many ponds at this stage melt through and the bottom ice may decay entirely. Pond coverage in this stage

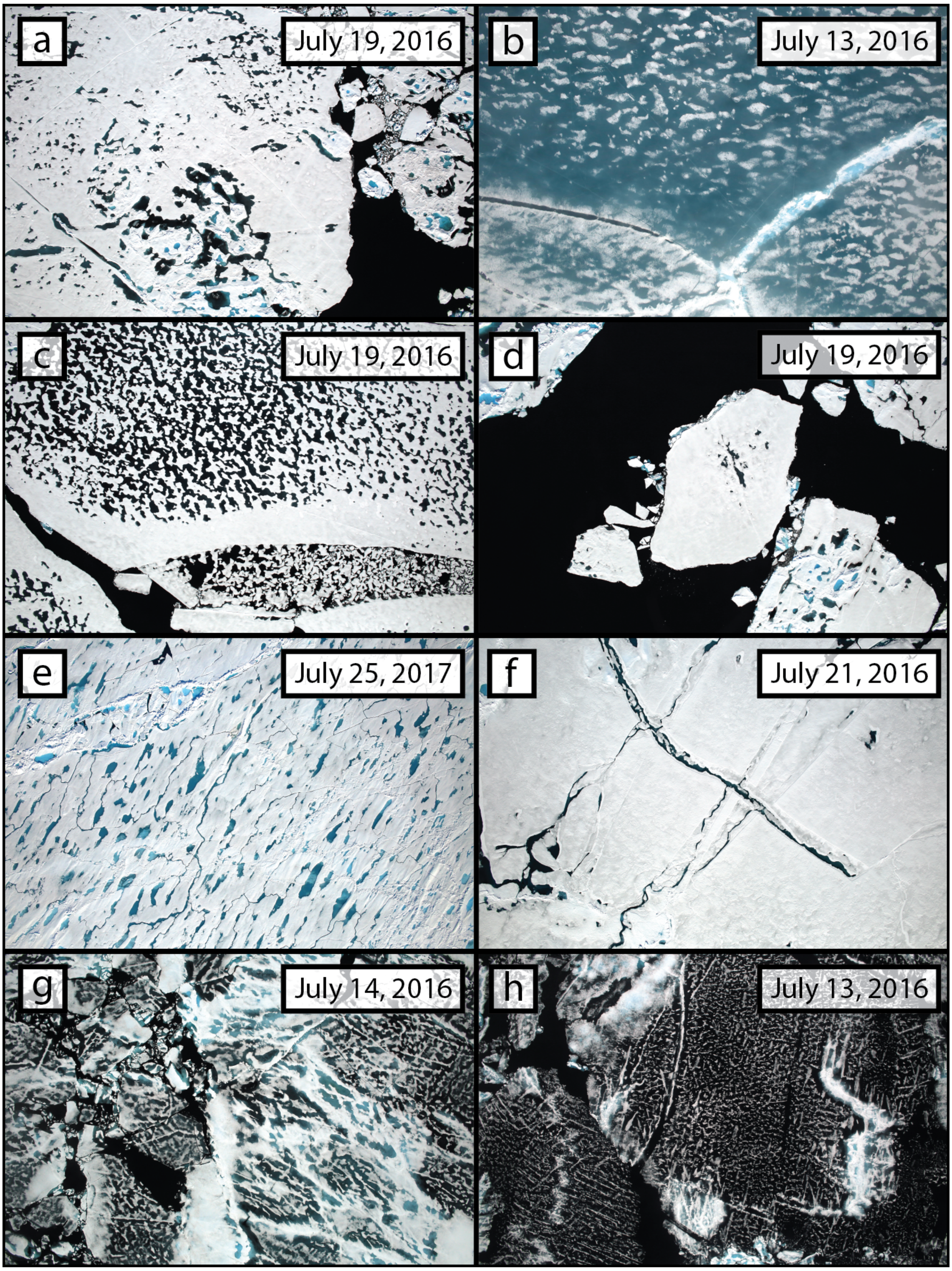

Figure 1.1: Melt ponds on FYI from Wright et al. (2020). True color RGB imagery from Operation IceBridge. Each image is approximately 600 m by 400 m. See Wright et al. (2020) for further details.

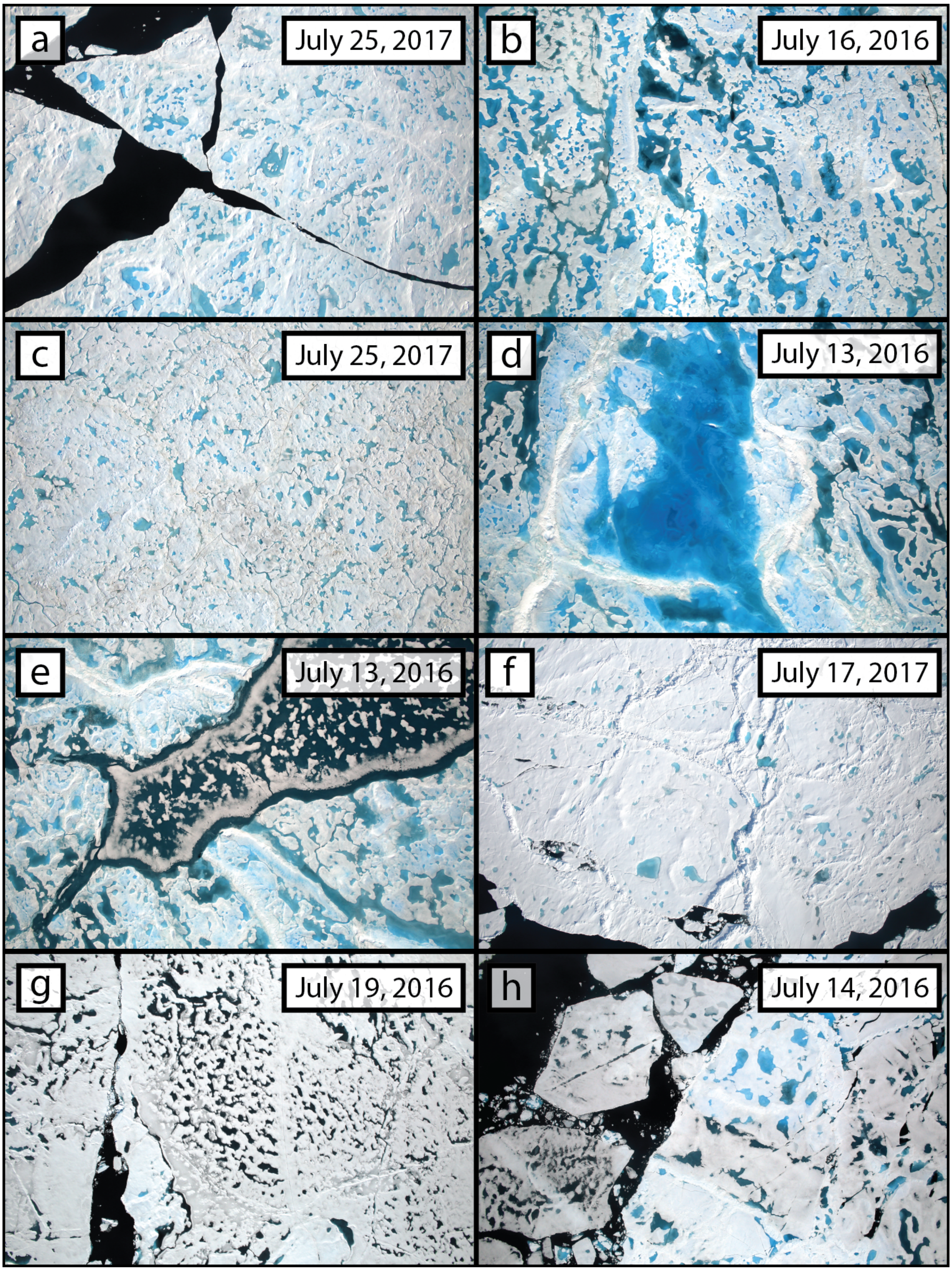

Figure 1.2: Melt ponds on MYI from Wright et al. (2020). True color RGB imagery from Operation IceBridge. Each image is approximately 600 m by 400 m. See Wright et al. (2020) for further details.

increases due to lateral melt or decreasing ice freeboard and associated surface flooding which result from overall thinning of the ice and a corresponding reduction of buoyancy (Polashenski et al., 2012). The fourth stage is either the refreezing of ponds or ice breakup. Note that this stage is not restricted to the end of the melt season but may be induced anytime air temperature drops below freezing point (Polashenski et al., 2012; Landy et al., 2014). Snow collecting on the newly formed ice cover may temporarily reduce the albedo effects of melt ponds (Grenfell and Perovich, 2004), which vanish entirely as soon as a thick snow cover establishes on a permanent ice over at the end of the melt season.

The spatio-temporal evolution of melt ponds on sea ice, i.e., onset, duration and sequence of the different stages, is governed by the initial snow and sea ice characteristics and their temporal response to environmental forcings and parameters, whereby the initial sea ice parameters were themselves controlled by environmental forcings that have previously governed sea ice formation and weathering. The environmental drivers that control the formation and evolution of sea ice include numerous forcings and parameters, e.g., air temperature, precipitation, (e.g., Flato and Brown, 1996), wind stress (e.g., Vihma et al., 2012), cloud cover (e.g., Liu et al., 2009), and atmospheric depositions (Light et al., 1998), river discharge and salinity of ocean surface water (Macdonald et al., 1999), sediment load (Light et al., 1998), water temperature, currents, tides, and waves (Webster et al., 2015). These factors vary regionally and on different spatial and temporal scales, which introduces a considerable variability in the spatio-temporal evolution of melt ponds on sea ice.

Our understanding of melt pond behavior primarily rests upon *in situ* field studies (Buckley et al., 2020), with most observations coming from first-year LFI and drifting MYI, where field campaigns are logistically feasible (Webster et al., 2015). Substantial advances in the understanding of the temporal evolution of melt pond characteristics came from the year-long Surface Heat Budget of the Arctic Ocean (SHEBA) field campaign in the Beaufort Sea (Uttal et al., 2002; Perovich et al., 2002; Perovich, 2002), which provided data for melt pond parameterization in modeling efforts (e.g., Curry et al., 2001; Taylor, 2004; Light et al., 2008; Skyllingstad et al., 2009; Pedersen et al., 2009; Scott and Feltham, 2010; Flocco et al., 2010; Holland et al., 2012). Webster et al. (2015) studied melt pond evolution for an entire melt season on drifting FYI and MYI on the 2011 Applied Physics Laboratory Ice Station. They found considerable differences compared to the 1998 SHEBA dataset, that confirm the significant impact of ice type and snow depth distribution on melt pond evolution in the drifting ice pack, and underline the spatio-temporal variability of melt pond evolution. Polashenski et al. (2012) compared field observations from different years, locations, and ice types, which revealed a large spatial and inter-annual variability. Particular differences can be observed between LFI and drifting pack ice resulting from effects of shallow coastal bathymetry, tides, nearshore currents, a fixed orientation to the sun and prevailing winds, and input of dust and warm air from adjacent land (Webster et al., 2015). Scharien and Yackel (2005) observed melt pond fractions (MPFs) ranging from 0 % to 75 % at a single site on undeformed FYI with coverages changing at rates as high as 35 % per day, and concluded that cycles of freezing and thawing, surface hydraulics, precipitation events, and predominant winds affect the spatio-temporal evolution of melt ponds on diurnal, daily, and weekly timescales, particularly on FYI and early in the melt season (Polashenski et al., 2012). Curry et al. (2001) describe hourly heat fluxes including diurnal freeze-thaw cycles complicating melt pond simulations. Eicken et al. (2004) found that short-term millimeter to centimeter changes in pond water level result in remarkable variability in pond fraction and area-averaged albedo within a few days. Landy et al. (2014) observed variations in the timing and/or magnitude of the four stages of melt pond evolution between different field sites on FYI. This large regional and spatio-temporal variability presents a challenge for the realistic representation in sea ice and climate models (Polashenski et al., 2012; Tsamados et al., 2015; Zhang et al., 2018).

1.1.2 Sea Ice Modeling

Despite its strong impact on sea ice albedo, melt pond evolution was not physically treated in GCMs for a long time. Instead, simulation of realistic sea ice extents was reached by tuning albedo parameterizations based on empirical relationships, thus, neglecting the natural variability of the ice surface and the observed range of melt pond albedo (Holland et al., 2012; Flocco et al., 2012; Hunke et al., 2013). As a consequence, GCMs were unable to capture the annual cycle of sea ice albedo (Pedersen et al., 2009). Since then, serious efforts have been made in physically-based representations of melt ponds in large-scale sea ice models (e.g., Pedersen et al., 2009; Flocco et al., 2010, 2012; Holland et al., 2012; Hunke et al., 2013; Lecomte et al., 2015; Zhang et al., 2018).

Results of Flocco et al. (2010, 2012) demonstrate that the physical representation of melt ponds has a strong impact on predicted sea ice thickness and extent. Schröder et al. (2014) used the Flocco et al. (2012) melt pond parameterization in the Los Alamos sea-ice model CICE to simulate the spatial and temporal evolution of melt ponds in the pan-Arctic region for the period 1979–2013 and found that September sea ice extent can be forecasted by May pond fraction with an accuracy of 0.5 million km^2. Their results underline the strong interannual variability and predict an increase of melt pond fraction by 3 % per decade. Zhang et al. (2018) incorporated a melt pond distribution conservation equation into the Marginal Ice-Zone Modeling and Assimilation System (MIZMAS) sea ice-ocean model and studied the spatio-temporal evolution of melt ponds in terms of fraction and volume with a focus on the link to snow and ice melt for the period 1979–2016. However, in contrast to Schröder et al. (2014), they did not observe significant trends in melt pond volume per unit ice area and melt pond area fraction. The diverging results indicate that there are substantial uncertainties in the representation of spatio-temporal melt pond variability in sea ice models (Zhang et al., 2018), likely resulting from knowledge gaps about melt pond evolution and other sea ice-snow interactions. Thus, further studies across the Arctic are warranted to improve the understanding of melt pond evolution, in order to optimize melt pond parameterization in sea ice and climate models (Buckley et al., 2020; Polashenski et al., 2012; Zhang et al., 2018; Hunke et al., 2013).

Field studies, however, are temporally and spatially limited snapshots that can only capture a limited proportion of the spatio-temporal, regional and inter-annual variability of melt pond evolution. Polashenski et al. (2012) and Hunke et al. (2013) therefore stress the demand for basin-wide, long-term, intercomparable data sets of melt pond characteristics for assessing potential feedbacks or trends in the behavior of ponds and for the evaluation of large-scale models. Such observations are only feasible by means of remote sensing.

1.1.3 Remote Sensing

Due to the remoteness and inaccessibility of the Arctic Ocean, *in situ* observations and field campaigns are expensive in logistical and monetary terms. At the same time, on-site investigations are spatially and temporally limited. This hampers the regular generation of Arctic-wide long-term, intercomparable data sets. Satellite remote sensing enables regular observations with large spatial coverage and therefore is the main tool for observations of Arctic sea ice. In addition, remote sensing from aircraft is frequently used to obtain high resolution observations on regional scales. Due to their exceptional role for the sea ice energy balance, melt ponds have long been subject to remote sensing studies that include passive and active sensors, operating in the optical or microwave wavelength region of the electromagnetic spectrum. Most remote sensing products aim to map melt ponds in terms of their two-dimensional representations, e.g., melt pond fraction, distribution or morphology, while approaches to map melt pond depth are rare or have been developed only recently.

1.1.3.1 Melt Pond Fraction and Morphology

Sensors that operate in the microwave wavelength region are frequently used in Arctic remote sensing because they are independent from solar illumination and cloud cover and therefore enable year-round observations (Meier and Markus, 2015). Melting processes on sea ice induce distinct signals, due to the sensitivity of microwave radiation to the surface's dielectric properties, which are strongly influenced by the amount of liquid water at the ice surface (Mortin et al., 2014).

Passive microwave satellite sensors are characterized by high temporal resolution and large spatial coverage, which enable daily coverage of the entire Arctic (Meier and Markus, 2015). Several studies have used passive microwave data to estimate the onset and length of melt (e.g., Markus et al., 2009; Bliss and Anderson, 2014) or MPF (e.g., Tanaka et al., 2016; Tanaka, 2020; Heygster et al., 2020). These estimates, however, are challenged by low spatial resolutions of multiple kilometers and the high absorption of water at all common frequencies used in microwave remote sensing, which prevents a distinction between melt ponds and open water.

Active scatterometers offer a similar coverage and temporal resolution as passive microwave sensors but image reconstruction methods provide enhanced spatial resolution of 4.45 km. These data have previously been used to map seasonal melt-freeze transition over sea ice (Howell et al., 2006; Mortin et al., 2014). Synthetic aperture radar (SAR) instruments have limited spatial coverage and temporal resolution but may provide regional-scale information on MPF at higher spatial resolutions of meters to tens of meters (e.g., Barber and Yackel, 1999; Makynen et al., 2014; Scharien et al., 2018, 2014; Howell et al., 2020). Results of Kim et al. (2013) and Han et al. (2016) indicate potential to map MPF at very high resolution up to 1 m at a local scale with TerraSAR-X, and even submeter resolution with future SAR missions. The strong absorption of liquid water in the microwave wavelength region, however, prevents estimating water depth with these data.

Passive optical remote sensing sensors that acquire short-wave radiation scattered into the sensor from the Earth's surface rely on the sun for illumination. Consequently, observations at high latitudes are restricted in winter months.

Moderate resolution passive optical satellite sensors like the Moderate Resolution Imaging Spectroradiometer (MODIS) and the Ocean and Land Colour Instrument (OLCI) are well established in Arctic remote sensing. Near-polar orbits, large swaths and the use of multiple sensors enable Arctic-wide coverage on a daily basis at spatial resolutions of hundreds of meters. For these reasons, these data are frequently used for calibration and validation of large-scale sea ice models (e.g., Zhang et al., 2018). Because their spatial resolution is much lower than the scale on which most sea ice features exist, each pixel in these data represents a mixture of different surface features, and the fractional retrieval of each surface class requires decomposition of the combined signal. Tschudi et al. (2008) introduced a basin scale MPF product based on linear spectral unmixing of the MODIS surface reflectance product. Rösel et al. (2012) used an artificial neural network (ANN) to speed-up the unmixing process. Yackel et al. (2017) introduced further improvement and considered melt ponds of different colors by means of multiple endmember spectral unmixing. These techniques, however, strongly depend on the representativeness of spectra used for unmixing, and large errors in MPF may be introduced if the actual melt pond reflectance deviates from the spectral database (Lee et al., 2020). Others used physical models or trained machine learning models on high spatial resolution imagery to overcome the limitations of a priori assumptions. Istomina et al. (2015b,a) used a physical model of sea ice and melt ponds (Zege et al., 2015) that does not rely on a spectral database to map MPF with the Medium Resolution Imaging Spectrometer (MERIS) and OLCI. Istomina and Heygster (2017) further improved the approach and stepped away from a pixel-wise approach by integrating air temperature (Mäkynen et al., 2020). Liu et al. (2017) and Lee et al. (2020) proposed MPF retrievals based on multi-layer ANNs and Ding et al. (2020) used an ensemble-based deep neural network. Wright and Polashenski (2020) investigated the applicability of spectral unmixing for the retrieval of MPF from MODIS imagery exemplified by the approach of Rösel et al. (2012). They found that a consistent estimation is not possible "at an accuracy suitable for validating melt pond models or establishing unambiguous long-term trends" (Wright and Polashenski, 2020). The reason is that these techniques rely on the assumptions that spectral signatures of each surface class do not change over time, and that spectral differences between the classes are large, which both are violated to varying degrees. To overcome these limitations, they generated random mixtures of different surface types based on field-observed albedos to train a multi-output random forest regression for unmixing. Although this approach improved MPF retrieval, they conclude that estimating MPF from moderate resolution imagery will always contain ambiguity due to "the similarity of certain pond modalities and open water, especially given atmospheric distortions common in the Arctic" (Wright and Polashenski, 2020).

Higher spatial resolution multispectral sensors such as Landsat 8 (L8) or Sentinel-2 (S-2) are a possible solution for the unmixing problems of moderate resolution sensors. These sensors provide spatial resolutions between 10 and 60 m, which reduces the number of surface classes per pixel. The higher spatial resolution, however, comes at the expense of reduced swath, spatial coverage and temporal resolution. Further, their orbits only enable observations up to $\sim 83°$ North. Holt and Digby (1985) were among the first who qualitatively analyzed Landsat Multispectral Scanner System data to distinguish different surface types. Markus et al. (2002, 2003) demonstrated the potential of Landsat 7 Enhanced Thematic Mapper (ETM+) imagery for the classification of thr sea ice surface. Rösel and Kaleschke (2011) used principal component analysis (PCA) to determine MPF but discovered many limitations for the usage of ETM+ for melt pond observations, including saturation problems of the 8-bit sensor and the long revisit time of 16 days, which reduces the chance for cloud-free image acquisitions. Contemporary higher spatial resolution sensors (MultiSpectral Instrument (MSI) on S-2, Operational Land Imager (OLI) on L8) have improved radiometric resolutions and were proved to be useful for melt pond observations only recently. Li et al. (2020) used linear spectral mixture analysis to assess the fractional coverage of sea ice, melt ponds, and open water from L8 and S-2 imagery and Wang et al. (2020) used PCA to retrieve MPF from S-2 imagery. Wright and Polashenski (2020) postulate that higher resolution satellite imagery provides a good trade-off between spatial resolution, coverage and return period, and recommend using this data to improve moderate resolution MPF products.

Very high spatial resolution optical satellite data are even further limited in swath width and temporal resolution, and some sensors are further limited regarding their spectral resolution. The strong albedo differences between snow and ice, melt ponds, and open water in the visible wavelength region of the electromagnetic spectrum (VIS), however, facilitate a separation of different surface classes in true color RGB or panchromatic imagery. The big advantage of this data, of course, is the very high spatial resolution of centimeters to few meters, which minimizes spectral mixing and enables analyzing melt pond morphology (e.g., size, shape, position). Fetterer and Untersteiner (1998) and Webster et al. (2015) respectively classified panchromatic national technical means of verification (NTM) imagery to study the temporal evolution of MPF over one summer. Very high spatial resolution image classifications (e.g., based on WorldView imagery) are frequently used for calibration and validation of lower spatial resolution MPF products (e.g., Nasonova et al., 2017; Yackel et al., 2017; Ding et al., 2020; Lee et al., 2020; Li et al., 2020; Wright and Polashenski, 2020).

Another tool commonly used for regional observations of melt ponds is airborne remote sensing, with first surveys accomplished as early as 1949 (Hattersley-Smith et al., 1952; Crary, 1958; Hanson, 1961). Until today most imaging systems consist of consumer photo or video cameras (e.g., Perovich and Tucker, 1997; Tschudi et al., 1997; Yackel et al., 2000; Hanesiak et al., 2001; Perovich et al., 2002; Inoue et al., 2008a; Tschudi et al., 2008; Birnbaum et al., 2009; Divine et al., 2015; Mingfeng et al., 2018).

Before the era of computer-based image processing, MPF was estimated with mechanical measuring instruments, e.g., planimeters (Langleben, 1969), or by manually cutting aerial images to separate the different sea ice features and then weighing the extracted scraps of each class (Birnbaum, personal communication). Later, images were classified with commercial software (e.g., Perovich et al., 2002), and today availability of powerful open source tools results in further improvement and automation (e.g., Miao et al., 2015; Wright and Polashenski, 2018; Buckley et al., 2020).

Airborne remote sensing offers a lot of flexibility compared to satellite observations. Depending on flight altitude, airborne imagery facilitates very fine spatial resolutions up to the centimeter scale, which enables extremely detailed observations on pond level. The temporal flexibility of airborne remote sensing enables observations at very high temporal resolution and synchronizing surveys with satellite overpasses. Consequently, these measurements are frequently used to provide areal sea ice information for validation of satellite products (e.g., Markus et al., 2003; Tschudi et al., 2008; Inoue et al., 2008a; Rösel et al., 2012; Lu et al., 2010) or to scale up field observations to regional scales (Hanesiak et al., 2001; Divine et al., 2015; Rösel et al., 2017). In addition, airborne surveys are possible below clouds, provide flexibility regarding flight altitudes, patterns and geometries, and enable simultaneous observations with multiple instruments. Langleben (1971) and Tschudi et al. (2001) combined true color RGB imagery with airborne radiometer measurements to estimate the influence of melt ponds on albedo on regional scales. Holt and Digby (1985) used radar and true color RGB imagery from aircraft to distinguish between several melt stages. An exceptional effort was made by NASA in the course of Operation IceBridge (OIB) (Koenig et al., 2010; Studinger et al., 2010). In between the breakdown of the Ice, Cloud and Land Elevation Satellite (ICESat) in 2009 and the launch of ICESat-2 in 2018, two NASA aircraft were equipped with numerous payloads, including four airborne LiDAR, five radar systems, a gravimeter, a magnetometer, a skin surface temperature sensor and a high resolution stereographic camera system, to continue data collection. Disadvantages of airborne surveys are limited coverage and high cost.

Moderate and low spatial resolution satellite sensors provide Arctic-wide data on MPF on a regular basis, higher spatial resolution provide a good trade-off between spatial resolution, coverage and return period, and high spatial resolution imagery enables observation of morphological characteristics, e.g., pond shape and size, on local and regional scales. The aforementioned studies quantify melt ponds in terms of their areal percentage coverage, two-dimensional morphology or classify melt ponds according to their color. A comprehensive understanding of melt ponds and their temporal evolution, however, requires not only information about their two- but their three-dimensional behavior, i.e., about the evolution of pond depth.

1.1.3.2 Melt Pond Depth

Pond depth influences melt pond albedo and transmittance of shortwave solar radiation into the ice interior and underlying ocean, thus, influencing radiative heating and melting. It is therefore considerably affecting the ice-albedo-feedback mechanism (Ebert et al., 1995; Taylor, 2004; Inoue et al., 2008b; Horvat et al., 2020) and is an important parameter in the treatment of radiative transfer in sea ice models (e.g., Flocco and Feltham, 2007; Flocco et al., 2010, 2012; Holland et al., 2012; Hunke et al., 2013; Lecomte et al., 2011; Pedersen et al., 2009; Zhang et al., 2018). Flocco et al. (2015) found that the depth of melt ponds at the beginning of refreezing governs basal ice growth in winter because deep ponds take longer to freeze and the associated release of latent heat delays basal ice growth. Ehn et al. (2011) observed that melt pond depth influences white ice freeboard, and Zhang et al. (2018) suppose that melt pond volume is more directly related to the energy budget than pond area, and influences freshwater flux at the ocean surface.

Besides the importance for the sea ice energy balance, melt pond depth is also relevant for other reasons. Scharien and Yackel (2005) describe that pond depth influences the formation of wind waves which play a role in the interpretation of radar backscatter. Rozell (2010) describes that the freshwater of melt ponds acts as a hull lubricant, and the evolution of melt ponds decreases ice strength (De Abreu et al., 2001), which both eases the passage of vessels through the ice. Up to date melt pond information, therefore, may help planning ship navigation (Guanter et al., 2016).

Despite its importance, only very few studies have investigated the retrieval of melt pond depth by means of remote sensing. Divine et al. (2016) used stereo-photogrammetry to retrieve small scale sea ice surface topography from low-altitude aerial imagery. Comparisons with *in situ* measurements showed that their approach enables mapping of melt pond bathymetry up to at least 0.3 m with high accuracy (RMSE = 0.04 m). Only recently, a novel technique for bathymetric mapping of melt ponds on sea ice from space became available with the launch of ICESat-2 in 2018. ICESat-2 carries the ATLAS instrument, a photon-counting LiDAR providing a nominal 17 m diameter footprint and a nominal 0.7 m along track point spacing that operates in the green wavelength region (532 nm) (Parrish et al., 2019). Even though the mission was designed for global surface elevation measurement with a primary focus on the cryosphere, the high penetration depth of green light into water enables bathymetry retrieval in shallow water bodies (Magruder et al., 2019; Parrish et al., 2019). Fair et al. (2020) mapped beds of supraglacial lakes as deep as 7 m with estimated uncertainties of 0.12–0.8 m.Only recently, Farrell et al. (2020) and Tilling et al. (2020) showed that ICESat-2 is potentially capable to derive the depth of melt ponds on sea ice. Recorded pond depth by Farrell et al. (2020), however, was higher than usually observed.Tilling et al. (2020) found that smooth ponds are highly reflective resulting in saturation problems. Further, retrieval of pond depth is only possible for pond depths greater than 20 cm and from four examples presented in Tilling et al. (2020) only two ponds featured photon return counts attributed to the pond bottom. Results of these studies are promising but no validation by means of *in situ* measurements has been performed, yet.

LiDAR is an active optical remote sensing technique that operates independently from solar illumination and provides year long observations but is hampered by the presence of clouds. In contrast to the sensors described previously, LiDAR are non-imaging sensors. Instead, single measurements are acquired along the sensor's flight track. This may represent a major disadvantage as the data only represent a one-dimensional profile along the flight track with no information about the two-dimensional bathymetry. Observations with ICESat-2 are further limited by the long return period of 91 days.

While the results presented in Divine et al. (2016), Farrell et al. (2020) and Tilling et al. (2020) are promising, both techniques have their weaknesses, e.g., photogrammetric retrieval of small scale sea ice topography is limited to airborne sensors and LiDAR does not provide two-dimensional bathymetric information. Short-wave passive multi- or hyperspectral remote sensing data in combination with a suitable model may provide an alternative method to map the bathymetry of water bodies.

1.2 A short Introduction to Radiative Transfer

The information medium used in passive short-wave optical remote sensing is light, usually emitted by the sun. It is the alteration of light by scattering and absorption, i.e., the optical properties of a medium, that provide information about its physical characteristics. Optical properties can be divided into apparent optical properties (AOPs) and inherent optical properties (IOPs). While IOPs, i.e., absorption and scattering coefficients, are properties of a medium that depend only on its composition, AOPs depend on a medium's IOPs and, in addition, on the directional structure of the ambient light field. Consequently, reflectances acquired with a remote sensor are an AOP. The relationship between radiances and IOPs is subject to radiative transfer theory, which is the basis for models used for atmospheric correction and bathymetry mapping by means of passive optical remote sensing (Ogashawara et al., 2017; Mobley et al., 2018).

1.2.1 Atmospheric Correction

Absorption and scattering by gaseous molecules and particulate matter modify light during transfer through the Earth's atmosphere. Radiances arriving at a remote sensor, therefore, contain information on both the Earth's surface and atmosphere. The process to subtract the atmospheric information from the combined signal is called atmospheric correction (AC).

AOPs measured by a remote sensor are defined by the AOPs of the atmosphere and the AOPs of an object at the bottom of atmosphere (BOA). Atmospheric AOPs can be described by the specific IOPs and concentration of gaseous molecules and particulate matter, thickness of the atmosphere between a sensor and the Earth's surface, illumination, and viewing geometry. Estimating aerosol concentrations requires knowledge about the distance between sensor and surface, the specific IOPs of atmospheric constituents, and the AOPs present at the BOA. As the latter are usually unknown, assumptions must be made. These assumptions rest on the existence of reference surfaces with known reflectance behavior (e.g. dense dark vegetation), which are frequent in most terrestrial environments but not on sea ice. Specific IOPs depend on the chemical and physical properties of the atmospheric constituents, which differ on spatial and temporal scales. Commonly used AC algorithms are developed for mid- and low-latitude environments, including typical concentrations of water vapor and aerosols, and their specific IOPs, but are not optimized for high-latitude Arctic atmospheric conditions (e.g., Lee et al., 2020). Further, the large sun zenith angle at high latitudes may be problematic because AC algorithms rely on plane-parallel atmospheric transfer calculations with sun zenith angles usually $< 70°$. For low sun zenith elevation, however, the curvature of the atmosphere must be taken into account (IOCCG, 2015). Other challenges may occur due to large adjacency effects, i.e., scattered light originating from neighboring pixels contributing to the measured signal, or contamination of ice in water pixels (Bélanger et al., 2007; IOCCG, 2015).

The different albedos of sea ice, melt ponds and open water in certain regions of the electromagnetic spectrum generally enable a robust classification of sea ice imagery, and most melt pond products derived from passive optical remote sensing data either base on TOA or at-sensor reflectance (e.g., Lee et al., 2020) or standard BOA reflectance products (e.g., Tschudi et al., 2008; Rösel et al., 2012) without questioning the suitability of the applied AC. Only Zege et al. (2015) have included AC in their MPF retrieval. Their algorithm enables manual parameterization based on observational data or assumes Arctic background aerosols (Tomasi et al., 2007, 2012).

Algorithms for quantitative estimation of bio-geophysical parameters from remote sensing data that base on field spectra rely on accurate correction of atmospheric influences.

This is particularly true for water bodies because of their comparably low albedo and correspondingly high relative atmospheric influence on radiances measured at-sensor (Mishra et al., 2017). Zege et al. (2015) show that AC strongly improves retrieval of albedo and MPF and Wright and Polashenski (2020) expect that errors in the MODIS surface reflectance product are in the order of 0.01–0.1. Despite the importance of AC, little effort was made to quantitatively assess the applicability of existing AC algorithms for the Arctic sea ice environment (IOCCG, 2015).

1.2.2 Bathymetry Mapping by Means of Passive Optical Remote Sensing

Mapping bathymetry by means of passive optical remote sensing requires a model describing the relationship between AOPs, e.g., water leaving reflectances, and depth of a water body at the sampled location. The premise for such a model is therefore that the bottom contributes to the AOPs arriving at the sensor, i.e., that the water body is optically shallow. Models that establish such a relationship can be roughly divided into empirical or analytical models (Gao, 2009; Dörnhöfer et al., 2016).

Empirical models are calibrated on the empirical relationship between a water body's AOPs acquired by a remote sensor, and the corresponding water depth at sampled locations. Optimal relationships between spectral bands and water depth are established exclusively via statistical techniques (e.g. ANNs, least squares regression, or step-wise regression) and do not consider any physical or optical principles. Semi-empirical models establish empirical relationships based on specific spectral features resulting from AOPs of the bottom. Empirical models may be very precise but require a database of water depths and corresponding spectra for calibration. Problems occur if measured AOPs are not represented in the database, e.g., in the presence of bottom types with different spectral characteristics, diverging illumination conditions or different water composition. Field measurements, however, are limited in space and time and, therefore, only represent a limited portion of the natural variability of AOPs. Consequently, empirical models are restricted to water bodies and/or situations matching the AOPs represented in the database and, thus, are vulnerable to changing environmental conditions (Ogashawara et al., 2017).

In contrast to empirical models, analytical models are based on the physical principles of radiative transfer. These models relate the AOPs of an optically shallow water body to the IOPs and depth of the water, and the AOPs of the bottom. Water depth can be determined by inversion of the radiative transfer equation. The IOPs of a water body are defined by the IOPs of the water itself and the concentrations of water constituents (e.g., phytoplankton, colored dissolved organic matter (CDOM), and non-algal particles). In optically shallow water, the AOPs of the bottom contribute to the bulk AOPs as described by its bidirectional reflectance distribution function (BRDF). Analytical models iteratively change the composition and height of the water column, and the composition of the bottom to fit a simulated to a measured spectrum and, thus, dynamically address different water depths, concentrations of water constituents, and bottom type mixtures. Yet, these models require knowledge about the specific IOPs of water constituents and the BRDFs of the bottom types present at site, which both may vary regionally as well as on spatio-temporal scales (Ogashawara et al., 2017) and depend strongly on the type of water body that is investigated.

One approach to tackle the limited variability of field measurements in empirical modeling is the application of analytical models to simulate a database that covers a wide range of AOPs (e.g., Hieronymi et al., 2017). This strategy, however, requires study area specific parameterization, e.g., regarding occurring bottom type BRDFs and water constituent IOPs.

1.3 Previous Work

Studies involving multi- and hyperspectral imaging sensors on aircraft and satellites for bathymetric mapping were conducted in different environments, e.g., in shallow coastal waters (e.g., Lyzenga, 1985; Jing and Datt, 2010; McIntyre et al., 2006; Ma et al., 2014), lagoons (e.g., Niroumand-Jadidi et al., 2020), reefs (e.g., Heege et al., 2007), lakes (e.g., Dörnhöfer et al., 2016), and rivers (e.g., Legleiter et al., 2009, 2016). To date, approaches to estimate the depth of melt ponds on Arctic sea ice from spectral data, however, are limited to field measurements and results suffered from large error.

The water bodies presumably most similar to melt ponds on sea ice, which have been subject to bathymetric mapping by means of remote sensing, are supraglacial lakes on the ice sheets of Greenland and Antarctica. Proposed methods include empirical models (e.g., Box and Ski, 2007; Legleiter et al., 2014) and analytical approaches based on the model of Philpot (1989) that connects the reflectance observed at a remote detector to bottom reflectance, depth and attenuation of the water, and reflectance of optically deep water. Deep water and bottom reflectance are obtained from dark ocean pixels and glacier ice pixels at the lake's edge, respectively. The water is considered to be pure natural fresh water, with known IOPs defined in literature. Knowing all parameters but depth enables inversion of the model (e.g., Sneed and Hamilton, 2007, 2011; Tedesco and Steiner, 2011; Georgiou et al., 2009). The different approaches were later compared (e.g., Moussavi et al., 2016; Pope et al., 2016) and refined, e.g., by considering different bottom type mixtures and water IOPs (Pope et al., 2016). Comparisons to *in situ* data or satellite-derived DEMs resulted in accuracies around 0.4 m (e.g., Georgiou et al., 2009; Legleiter et al., 2014; Moussavi et al., 2016) for depths up to several meters. However, in shallow water with depths less than 2 m RMSD was 0.9 m (Georgiou et al., 2009). Tedesco and Steiner (2011) found that the assumption of substrate homogeneity is problematic due to the presence of cryoconite holes and report a $\sim$ 10 % difference between mean bottom reflectance and mean reflectance values along the lake edge, which translates into an average error on lake depth retrieval up to –15.9 %, and maximum errors of –42.7 % in shallow water. Further, they found that the range of lake depth challenges the approach introduced by Sneed and Hamilton (2007) because of the wavelength dependent attenuation of water, which was later approved by Moussavi et al. (2016) and Pope et al. (2016). Results of Pope et al. (2016) further reveal that the empirical model of Legleiter et al. (2014) considerably overestimates lake depth, indicating that data from just one lake is not sufficiently representative. Most of the parameterizations of the physically based models also resulted in substantial overestimation of lake depth. Comparisons of absorption coefficients derived from imagery with the method proposed by Sneed and Hamilton (2007) and laboratory measurements revealed that lake depth estimation strongly depends on the the applied absorption coefficient. A sensitivity study based on simulated atmospheric path radiance further showed that differences in the red band by ±1.6 % propagate to errors of $10-30$ %. As the physically-based methods estimate deep water reflectance by means of ocean water pixels while melt water lakes may exist in high elevation areas far away from the coast, regional differences of atmospheric thickness and IOPs presumably have a large impact on the lake depth retrieval, pointing to the need for a rigorous atmospheric correction of satellite imagery (Pope et al., 2016).

Results of these studies may be sufficiently accurate for supraglacial melt water lakes with depths of several meters to tens of meters. Melt ponds on sea ice, however, are far more shallow. Reported accuracies in the range of tens of centimeters to meters are therefore not adequate. Another major difference between supraglacial melt water lakes and melt ponds on sea ice are the properties of the underlying ice. Sneed and Hamilton (2007, 2011), Pope et al. (2016) and Moussavi et al. (2020) used pixels at the edges of supraglacial lakes to describe lake bottom reflectance. While this assumption may be valid for glacial lakes, sea ice pixels are usually inappropriate to describe the bottom reflectance of melt ponds on sea ice. At the beginning of the melt season, the unponded sea ice surface forms a surface scattering layer of deteriorated ice in granular form, similar to coarse grained snow, with a typical thickness of 0.01–0.1 m and a scattering coefficient about 1–2 magnitudes larger than for ponded ice (Light et al., 2008). In contrast to bare ice, most of the downwelling irradiance is backscattered out of the ice, which explains the increased transmittance of light through ponded ice (Light et al., 2015; Taskjelle et al., 2017).

Another difference is the influence of ice thickness on the AOPs of melt ponds on sea ice. The AOPs of melt ponds on sea ice just above the water surface are defined by the ambient light field, the AOPs of the water surface, the AOPs of the pond water, defined by its IOPs and pond depth, and the AOPs of the pond bottom, which is defined by its IOPs and thickness. Yet, in contrast to supraglacial lakes the thickness of the underlying ice may be smaller than its optical thickness. In this case, the AOPs of the ocean beneath the pond bottom would also contribute to the AOPs of a melt pond. Modeling radiative transfer in sea ice has a long tradition (e.g., Grenfell and Maykut, 1977; Perovich and

Grenfell, 1982; Grenfell, 1991) but only recently some efforts were made to model radiative transfer in a combined melt pond-sea ice system to inversely estimate pond depth from field measurements.

Lu et al. (2016) developed a two-stream radiative transfer model to investigate the dependence of melt pond albedo and transmittance through ponded ice on pond depth and thickness of the underlying ice. Following the work of Taylor (2004) their model considers down- and upwelling irradiance in each layer under the assumption of diffuse incident radiation and isotropic scattering. They further made the following assumptions: (1) melt pond and ocean water are pure, without absorbing or scattering contaminants, (2) water is purely absorbing, (3) scattering in sea ice is spectrally flat, and (4) absorption in sea ice is described by the combined absorption coefficients of pure ice and sea water. Variations of pond depth (0–0.5 m) and ice thickness between (0.5–5.0 m) indicate that spectral albedo and transmittance both depend on pond depth only in the 600–900 nm range, while ice thickness is most influential in the 350–600 nm wavelength region. In a follow up paper, Lu et al. (2018) repeated the experiment but transformed the simulated spectra into RGB color space. Retrievals of pond depth from field data (Istomina et al., 2016) indicate that there is no clear relationship between pond depth and melt pond color in the VIS, confirming the findings of Lu et al. (2016).

Malinka et al. (2018) developed an analytical radiative transfer model based on the work of Makshtas and Podgorny (1996). The model relates melt pond spectral reflectance to pond depth and bottom albedo based upon the following assumptions: (1) melt water is pure and there is no scattering or absorption by contaminants, (2) the water is purely absorbing and scattering is negligible, and (3) the pond bottom reflection is isotropic. Pond bottom albedo is defined by the IOPs, i.e., transport scattering and absorption coefficients, and the thickness of the ice layer, whereby only the absorption coefficient of ice has a spectral behavior. Consequently, the spectral reflectance of the pond is determined only by pond depth, and the scattering coefficient and geometric thickness of the underlying ice. In contrast to Lu et al. (2016), Malinka et al. (2018) address the geometry of the incident light field and illustrate the influence of solar zenith angle on the spectral albedo. Inverse computations of measurements from three different field campaigns show that the model accurately reproduces melt pond albedo between 350 nm and 1300 nm. Retrieval of pond depth, however, is more uncertain as measured and simulated depths differ up to two times, with a corresponding RMSD of 65 %.

Results of Lu et al. (2016, 2018) and Malinka et al. (2018) indicate that the proposed methods are not suitable to derive the depth of melt ponds on sea ice from optical data.

1.4 Objectives and Outline

The previous chapters lead to the following conclusions:

- Areal information on melt pond depth and its temporal evolution should be mapped on large spatial scales with high temporal resolution. This information would help improving sea ice, climate and ecosystem models, to advance our understanding of the changing Arctic sea ice, and may assist navigation.
- Remote sensing enables regular, intercomparable long-term sea ice observations on large spatial scales but the majority of melt pond observations are limited to fractional coverage or two-dimensional morphology.
- Hyper- and multispectral imaging sensors on satellites and aircraft have successfully been used to derive water depth in different environments but existing approaches to derive the depth of melt ponds from optical data are either not appropriate for ponds on sea ice or do not provide the required accuracy.
- Atmospheric correction is an important step in the processing of passive optical remote sensing imagery that ensures intercomparability on regional and temporal scales, and is particularly important for the estimation of geophysical parameters, e.g., bathymetry. However, applicability of existent AC algorithms for the Arctic sea ice environment has not yet been investigated.

These findings point towards the primary goal of this dissertation, which is the development of a novel methodology to accurately estimate melt pond depth from passive optical measurements that is potentially scalable to air- and spaceborne systems. Reaching this goal requires achieving the following research objectives:

1. Development of a new method to accurately derive the depth of melt ponds on Arctic sea ice from optical data.
2. Scaling the new method to airborne imaging sensors to map melt pond bathymetry.
3. Assessing the suitability of existing atmospheric correction approaches for optical satellite imagery for deriving BOA reflectance of Arctic sea ice.

To achieve these objectives, a uniquely comprehensive dataset consisting of field measurements, hyperspectral airborne remote sensing data and spaceborne multispectral Sentinel-2 imagery was acquired during RV *Polarstern* cruise PS106 in summer 2017.

The thesis is based on the following publications:

- König, M. and Oppelt, N. (2020): A linear model to derive melt pond depth on Arctic sea ice from hyperspectral data
- König, M., Birnbaum, G., and Oppelt, N. (2020): Mapping the Bathymetry of Melt Ponds on Arctic Sea Ice Using Hyperspectral Imagery

- König, M., Hieronymi, M., and Oppelt, N. (2019): Application of Sentinel-2 MSI in Arctic Research: Evaluating the Performance of Atmospheric Correction Approaches Over Arctic Sea Ice

Excerpts will not be cited.

Chapter 2

A Linear Model to Derive Melt Pond Depth on Arctic Sea Ice From Hyperspectral Data

M. König and N. Oppelt

The Cryosphere (2020), doi:10.5194/tc-14-2567-2020
Received: 31 October 2019 - Discussion started: 9 December 2019
Revised: 28 May 2020 - Accepted: 1 July 2020 - Published: 12 August 2020

Abstract. Melt ponds are key elements in the energy balance of Arctic sea ice. Observing their temporal evolution is crucial for understanding melt processes and predicting sea ice evolution. Remote sensing is the only technique that enables large-scale observations of Arctic sea ice. However, monitoring melt pond deepening in this way is challenging because most of the optical signal reflected by a pond is defined by the scattering characteristics of the underlying ice. Without knowing the influence of meltwater on the reflected signal, the water depth cannot be determined. To solve the problem, we simulated the way meltwater changes the reflected spectra of bare ice. We developed a model based on the slope of the log-scaled remote sensing reflectance at 710 nm as a function of depth that is widely independent from the bottom albedo and accounts for the influence of varying solar zenith angles. We validated the model using 49 *in situ* melt pond spectra and corresponding depths from shallow ponds on dark and bright ice. Retrieved pond depths are accurate (root mean square error, RMSE = 2.81 cm; nRMSE = 16 %) and highly correlated with *in situ* measurements (r = 0.89; p = 4.34×10^{-17}). The model further explains a large portion of the variation in pond depth ($\mathrm{R}^2 = 0.74$). Our results indicate that our model enables the accurate retrieval of pond depth on Arctic sea ice from optical data under clear sky conditions without having to consider pond bottom albedo. This technique is potentially transferrable to hyperspectral remote sensors on unmanned aerial vehicles, aircraft and satellites.

2.1 Introduction

Melt ponds on sea ice are key elements for the Arctic energy budget. They are a main driver of the ice–albedo feedback mechanism (Curry et al., 1995) and affect the mass and heat balance of sea ice (e.g., Flocco et al., 2012; Perovich et al., 2009). Observations of pond evolution can be linked to observations of sea ice, ocean and atmosphere (e.g., Inoue et al., 2008b; Polashenski et al., 2012; Webster et al., 2015) for validation of ice and climate models (e.g., Flocco et al., 2012) and future sea ice prediction (e.g., Schröder et al., 2014). In the context of climate change, it is therefore important to increase our understanding of how melt ponds on sea ice change (Lee et al., 2012).

Recent efforts were made to observe the evolution of melt pond fraction with satellite data (e.g., Istomina et al., 2015b,a; Rösel et al., 2012; Tschudi et al., 2008; Zege et al., 2015), but few studies investigated melt pond depth despite its relevance for many applications. Melt pond depth is a parameter in the Los Alamos sea ice model CICE (Flocco et al., 2012; Hunke et al., 2013) and the ECHAM5 general circulation model (Pedersen et al., 2009). Lecomte et al. (2011) used pond depth to parameterize melt pond albedo in a snow scheme for the thermodynamic component of the Louvain-la-Neuve sea ice model. Holland et al. (2012) related pond water volume to surface meltwater fluxes in the community climate system model, version 4, and Palmer et al. (2014) used melt pond depths to model primary production below sea ice. Liu et al. (2015) point out that climate models and forecast systems that account for realistic melt pond evolution "seem to be a worthy area of expanded research and development" (Liu et al., 2015) and question the suitability of statistical forecasting methods in the context of the changing Arctic, which points towards the need for regular observations with large spatial coverage.

Synoptic observations of melt pond evolution are only possible with satellite remote sensing. Optical sensors with an adequate spatial resolution that operate in the visible (VIS) and near-infrared (NIR) wavelength regions enable the monitoring of pond water characteristics. The reflected optical signal from melt ponds without ice cover contains information on the pond water, the pond bottom, underlying ice and skylight reflected at the water surface.

Some studies investigated the potential to map the bathymetry of melt ponds with optical data in supraglacial lakes on the Greenland ice sheet. Tedesco and Steiner (2011) used the model of Philpot (1989) for optically shallow water and resampled hyperspectral reflectance measurements from below the water surface to Landsat and MODIS bands in order to explore its capability to derive the depth of a supraglacial lake. Due to the strong absorption of water in the near infrared, they limited the data range to 450–650 nm and excluded depth measurements < 1 m "because of the relatively small sensitivity of the reflectance data in the Landsat and MODIS blue and green bands to shallow waters" (Tedesco and Steiner, 2011). In comparison with shallow water sonar measurements, they underestimated depth by –23.7% and –42.7% for Landsat bands 1 and 2, respectively.

Legleiter et al. (2014) used hyperspectral remote sensing reflectance measurements above the water surface to map the bathymetry of supraglacial lakes and streams. They used an optimal band ratio analysis to find suitable band combinations for calibrating an empirical model based on field measurements on the Greenland ice sheet. A model based on two bands in the yellow–orange wavelength region resulted in an R^2 of 0.92 and a standard error of 0.47 m for depths ranging between 0.31 and 10.45 m. While this accuracy may be sufficient for glacial lakes, the maximum depth of ponds on sea ice is restricted by its thickness and therefore seldom exceeds 1 m (Morassutti and Ledrew, 1996; Perovich et al., 2009).

The color of melt ponds on sea ice ranges from bright blue to almost black and is primarily defined by the scattering and, to a lesser degree, by the absorption characteristics of the pond bottom (Lu et al., 2016, 2018). Different radiative transfer models for melt ponds on sea ice exist, but their capability to derive pond depth varies. Lu et al. (2016, 2018) developed a two-stream radiative transfer model to retrieve pond depth and the thickness of the underlying ice from RGB images but did not find a clear relationship between simulated and measured pond depth using the data from Istomina et al. (2016). To our knowledge, the most accurate model is the one presented in Malinka et al. (2018) resulting in an R^2 of 0.62 ($N = 26$) for *in situ* pond depths between 6 and 50 cm acquired under different illumination conditions. Their analytical two-stream radiative transfer model links the spectral albedo of ponds between 350 and 1300 nm at various sky conditions to pond depth and transport scattering coefficient and and thickness of the bottom ice. Fitting these parameters during inverse computation of *in situ* datasets from three field campaigns accurately reproduced *in situ* albedo spectra (relative root mean square difference, rRMSD < 1.5 %), but pond depth retrieval was more uncertain (rRMSD $= 65$ %).

We hypothesize that instead of using the entire spectrum, selecting bands in the near-infrared wavelength region improves the retrieval of pond depth on sea ice from optical data. The penetration depth of light into water is highest in the blue region of the electromagnetic spectrum and decreases with increasing wavelength; i.e., with increasing wavelength the influence of the water column's attenuation on the optical signal increases (Pope and Fry, 1997). Mapping the bathymetry of supraglacial lakes with a two-band model is challenging because the attenuation of water is wavelength dependent and the range of depths is wide. For shallow ponds on sea ice, Morassutti and Ledrew (1996) stated that the influence of water absorption on the pond albedo increases towards the NIR wavelength region. Lu et al. (2016) found that pond albedo significantly depends on pond depth in the wavelength region between 600 and 900 nm. In this paper, we therefore present a linear pond depth model for Arctic sea ice based on the absorption of near-infrared light in water from hyperspectral optical measurements under clear sky conditions.

2.2 Methods

We use spectral data of bare ice surfaces to simulate melt pond spectra for model development and validate the model with *in situ* melt pond measurements acquired during RV *Polarstern* cruise PS106 in summer 2017.

2.2.1 Observational Data

We used two instrument setups for the acquisition of optical data. For most measurements, we used a combination of two Ocean Optics STS-VIS spectrometers (Ocean Optics Inc., USA): one spectrometer pointing downwards and equipped with a 1° fore optic, the other pointing upwards and equipped with a cosine collector. Both instruments cover the wavelength region from $\sim$ 340 to $\sim$ 820 nm with a spectral resolution of 3.0 nm (Ocean Optics, 2019). We used a Labsphere Spectralon® 99% diffuse reflectance standard (Labsphere) as white reference and applied the data from the second spectrometer to correct the reflectance spectra for changes in downwelling irradiance. For each measurement, we computed the average of 30 individual spectra. Both instruments were mounted on the end of a 1 m long pole to avoid influences of the polar clothes on the measurements. We also attached a camera to the setup to take photographs of each measurement site (Figure 2.1).

Some of the data used in this study were acquired within the scope of an angle-resolving bidirectional reflectance distribution function (BRDF) experiment. For these measurements, we used an Ibsen Freedom VIS FSV-305 spectrometer (Ibsen Photonics A/S, Denmark) with a spectral resolution of 1.8 nm covering the wavelength range from $\sim$ 360 to $\sim$ 830 nm (Ibsen Photonics, 2019). The spectrometer was equipped with an optical fiber and a 1° fore optic that were attached to a field goniometer (Figure 2.2). We used the abovementioned Spectralon® panel as white reference after each azimuthal scan and computed an average reflectance from 20 spectra.

The quantity measured with both spectrometer setups is the remote sensing reflectance (R_{rs}; sr^{-1}) above the water surface:

$$R_{rs} = \frac{L_u}{E_d}, \tag{2.1}$$

where L_u is upwelling radiance - W(m^2 nm sr)$^{-1}$ - measured by the downward-pointing sensor and E_d is downwelling irradiance - W(m^2 nm)$^{-1}$ - which is derived from the Spectralon® measurement as

$$E_d = \frac{L_S \cdot \pi}{R_S} \tag{2.2}$$

where R_S is the isotropic reflectance of the Spectralon® panel and L_S is a radiance measurement – W(m^2 nm sr)$^{-1}$ – of the Spectralon® panel.

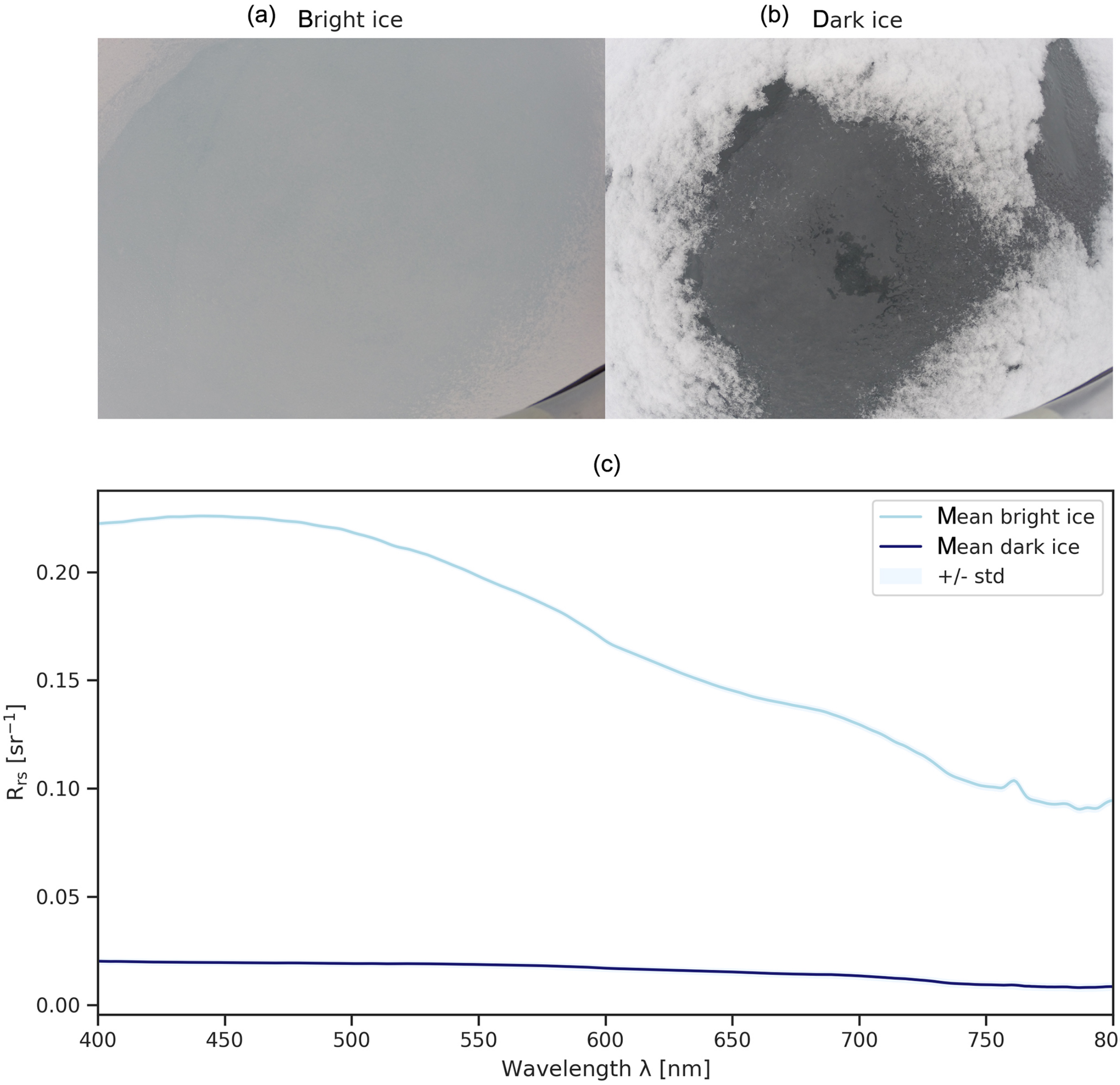

Figure 2.1: Photos of bright (a) and dark (b) bare ice surfaces and respective reflectance spectra (c). We took the photos from approximately 50 cm (a) and 30 cm (b) above the surface.

2.2.1.1 Ice Spectra

On 15 June 2017, we used the Ocean Optics setup to collect spectra from three bright and one dark bare ice surfaces (Gege et al., 2019) that were missing the typical surface scattering layer (Figure 2.1a,b). We therefore assume that their optical properties are comparable to pond bottoms. Illumination was diffuse and stable which was indicated by the negligible standard deviation of the 30 spectra contained in one measurement (Figure 2.1c).

On 2 July 2017 between 00:35 and 01:18 LST, we performed 12 nadir measurements of a bare ice surface, likewise missing a surface scattering layer (Figure 2.2a), under clear sky conditions and a mean solar zenith angle of 74.89° with the Ibsen setup (Gege and

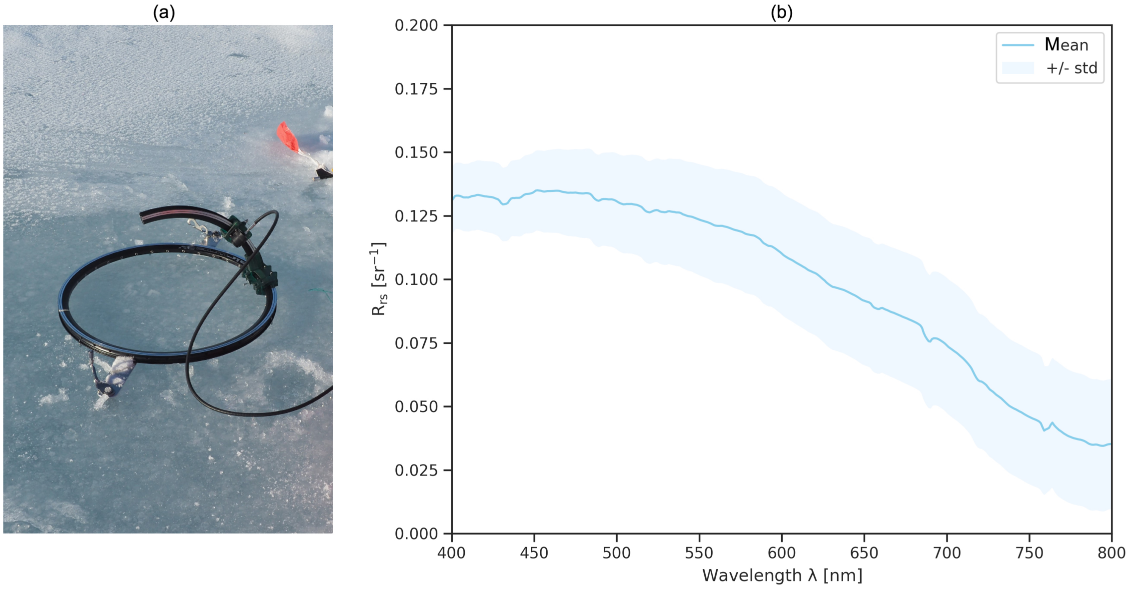

Figure 2.2: Ibsen bare ice measurement setup (a). Spectra used in this study (b) were taken at nadir.

König, 2019). Here we use the average spectrum. The large standard deviation may be attributed to surface metamorphism during the measurement (Figure 2.2b).

2.2.1.2 Pond Measurements

On 10 June 2017, we collected 49 melt pond spectra (Gege et al., 2019) and corresponding pond depths in three melt ponds. Two of the ponds had a bright blue color, while the third one was very dark, which is also apparent in Figure 2.3. The pond site was located in a ridged area, and ice thickness measurements from 14 June 2017 showed that ice thickness was ≥ 0.9 m below the bright ponds and ≤ 0.5 m below the dark pond, which indicates that the bright ice is older. We presume that the dark ice may have been a refrozen lead. However, no ice cores were analyzed to determine the respective ice types.

The bottoms of the bright ponds were mostly smooth and solid but also featured a few cracks and highly scattering areas that were very porous. The dark pond bottom was more heterogeneous and featured cracks and areas that were porous and riddled with holes (Figure 2.4).

At each pond, we referenced the Ocean Optics spectrometers using the Spectralon® panel before data acquisition. We performed spectral measurements from the edge of the pond or waded through the pond avoiding shading. We did not observe any wind-induced disturbances of the water surface and waited for the water surface to settle before performing measurements inside the ponds. All measurements were performed under clear sky conditions between 12:23 LST and 14:43 LST and corresponding solar zenith angles between 58.90 and 61.04°. Directly after each spectral measurement, we used a folding ruler

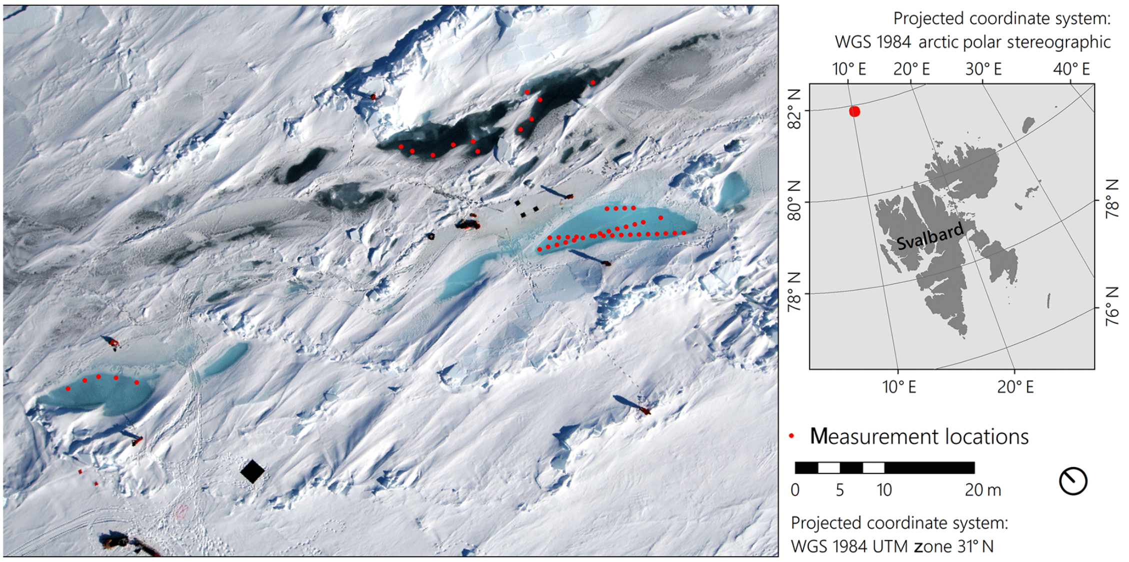

Figure 2.3: Overview of measurement sites in the three ponds. Aerial photo: Gerit Birnbaum.

to measure pond depth at the same location. Depths ranged between 6 and 25 cm with an average of 17.60 cm. Figure 2.5 illustrates the melt pond spectra and corresponding pond depths.

2.2.1.3 Data Smoothing

Even though the spectra appear smooth at first view, the hardly visible amount of noise in the data becomes relevant for calculating derivatives. To smooth the spectra, we therefore resampled all spectra to a 1 nm spectral sampling by linear interpolation and then applied a running average filter with a width of 5 nm.

2.2.2 Model Development

To develop an approach that does not require knowledge about on-site ice characteristics, our model must be independent from changes in the bottom albedo, i.e., scattering characteristics of the underlying ice. It shall further be applicable to a wide range of pond depths up to 1.0 m. Because the *in situ* melt pond dataset is limited to shallow depths and biased towards bright blueish ponds, we used the Water Color Simulator (WASI) to create a spectral library covering different bottom type mixtures and depths. WASI is a software tool for the analysis and simulation of deep and shallow water spectra that is based on well-established analytical models (Gege, 2004, 2014, 2015; Gege and Albert, 2006). We used the forward mode of the program WASI-2D (v4.1) to generate libraries of melt pond spectra. The procedures are described in the following.

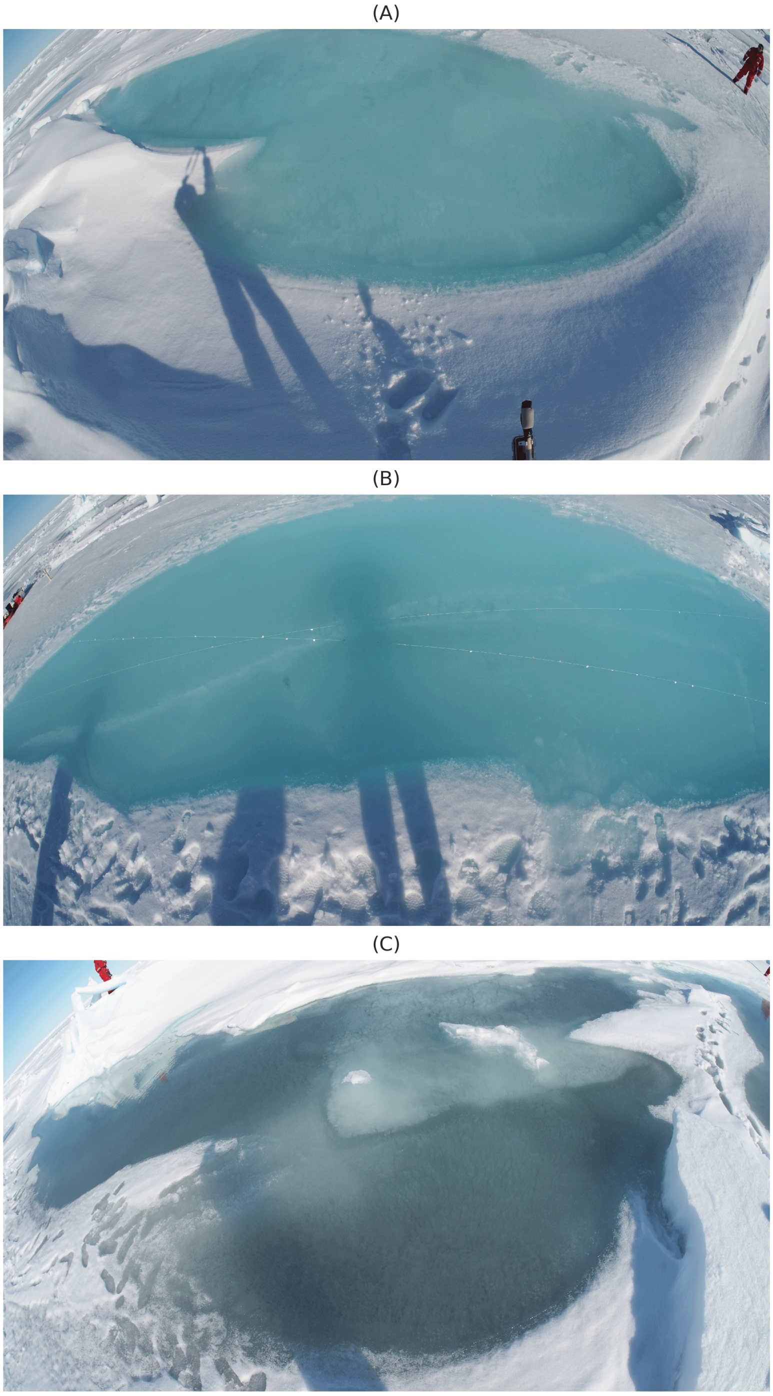

Figure 2.4: Photos of the small (a) and large (b) bright ponds and the dark pond (c). Photos: Peter Gege.

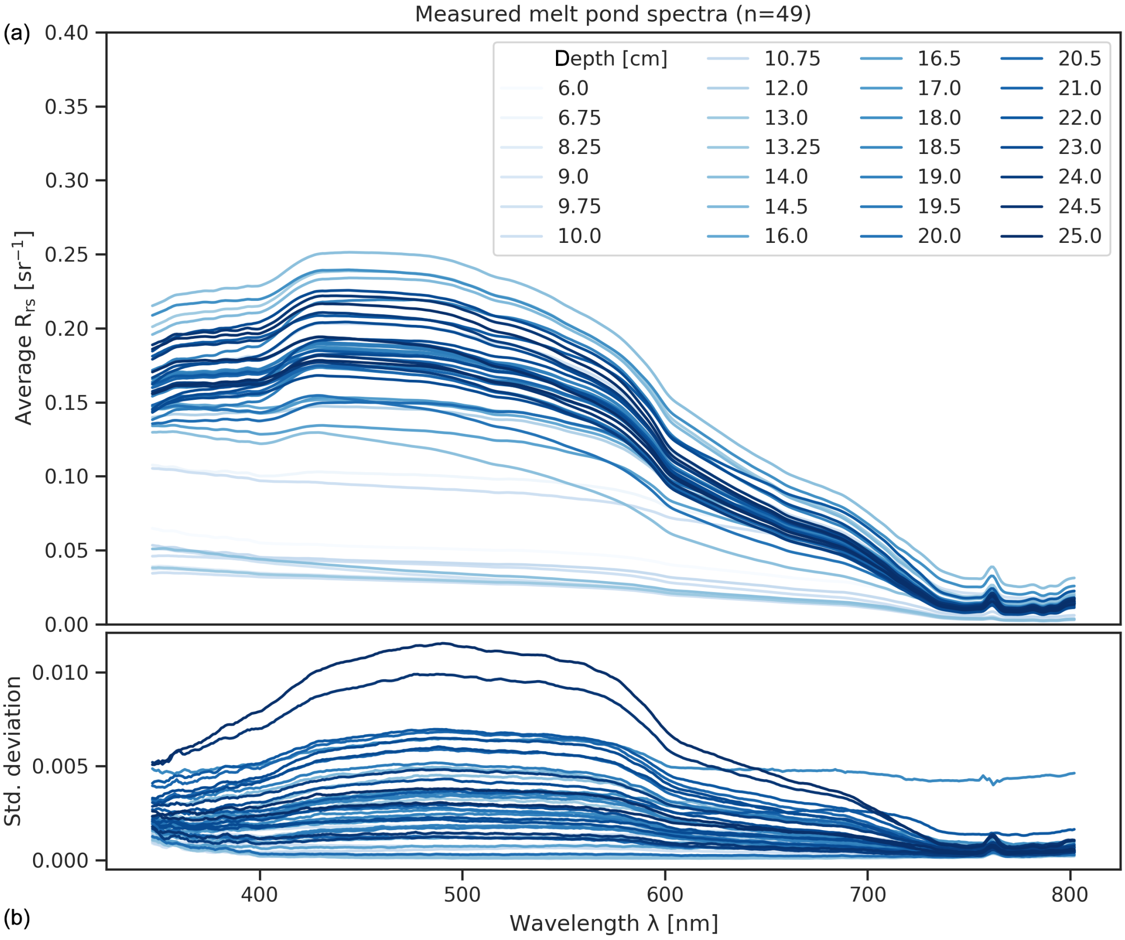

Figure 2.5: Average reflectance spectra (a), standard deviation of 30 measurements (b) and corresponding pond depths.

2.2.2.1 Simulated Data

We used the Ocean Optics bare ice spectra from overcast sky conditions (Section 2.2.1.1) as pond bottom reflectance

Analyses of optical properties of water samples showed only negligible amounts of chlorophyll a, colored dissolved organic matter and total suspended matter. Moreover, Podgorny and Grenfell (1996) report that the signal of scattering in meltwater is overwhelmed by the scattering in the bottom ice. We therefore defined a pure water column without additional absorbing or scattering water constituents and computed remote sensing reflectance in shallow water above the water surface according to Eq. (2.20b) in Gege (2015):

$$R_{rs}^{sh}(\lambda) = \frac{(1-\sigma)(1-\sigma_L^-)}{n_w^2} \cdot \frac{R_{rs}^{sh-}(\lambda)}{1-\rho_u \cdot Q \cdot R_{rs}^{sh-}(\lambda)} + R_{rs}^{surf}(\lambda) \tag{2.3}$$

where σ, σ_L^- and ρ_u are the reflection factors for E_d and upwelling radiance (L_u^-) and irradiance just below the water surface. σ and ρ_u are 0.03 and 0.54, respectively, while σ_L^- is calculated from the viewing angle (0° for a nadir-directed sensor). n_w is the refractive index of water (≈ 1.33), and Q is a measure of the anisotropy of the light field in water, approximated as 5 sr. R_{rs}^{sh-} is the remote sensing reflectance just below the water surface according to Albert and Mobley (2003):

$$\begin{aligned} R_{rs}^{sh-}(\lambda) = R_{rs}^{-}(\lambda) \cdot [1 - A_{rs,1} \cdot \exp\{-(K_d(\lambda) k_{uW}(\lambda)) \cdot z_B\}] \\ + A_{rs,2} \cdot R_{rs}^{b}(\lambda) \cdot \exp\{-(K_d(\lambda) + k_{uB}(\lambda)) \cdot z_B\}, \end{aligned} \tag{2.4}$$

where $A_{rs,1}$ and $A_{rs,2}$ are empirical constants and K_d, k_{uW}, and k_{uB} describe the attenuation of the water body with depth z_B defined by its absorption and backscattering and the viewing and illumination geometry. The first part of Equation 2.4 describes the contribution of the water body and the second part the contribution of the bottom. R_{rs}^- is the remote sensing reflectance of deep water just below the water surface defined by the absorption and backscattering of the water body and the viewing and illumination geometry. R_{rs}^b is the remote sensing reflectance of the bottom that is defined as the sum of the fractional radiances of all contributing bottom types defined by their albedos and under the assumption of isotropic reflection. R_{rs}^{surf} in Equation 2.3 is the ratio of radiance reflected by the water surface and E_d. We set R_{rs}^{surf} to zero; thus, the last part of Equation 2.3 can be ignored. We further used a solar zenith angle of 60°, similar to the *in situ* measurements, and a viewing angle of 0° (nadir). We computed linear mixtures of the two measured bottom albedos in 25 % steps (100 % dark, 0 % bright; 75 % dark, 25 % bright; ...; 0 % dark, 100 % bright). Using this setup, we generated a spectral look up table (LUT) by increasing pond depth from 0 to 100 cm in intervals of 1 cm, which is adequate for the great majority of melt ponds on Arctic sea ice. The final LUT contains 505 spectra (Figure 2.6).

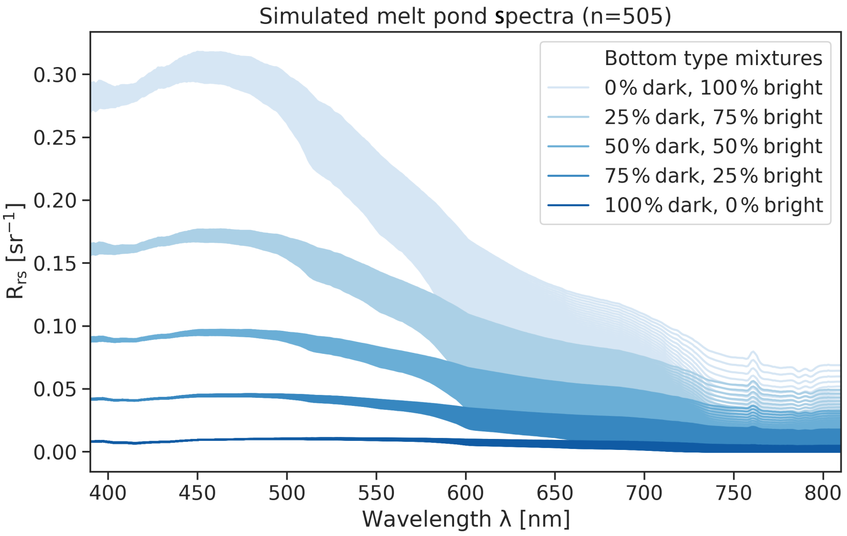

Figure 2.6: LUT generated with WASI-2D. Each of the five bottom type mixtures consists of 101 spectra (0 to 100 cm in 1 cm steps).

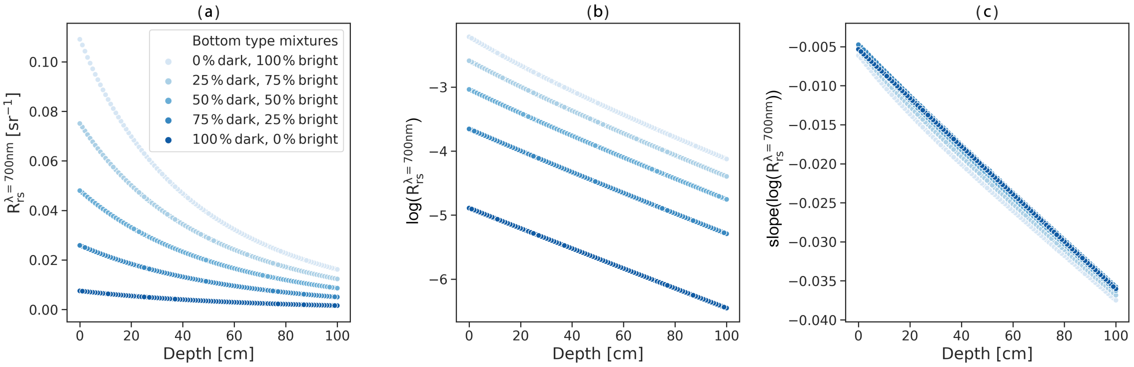

Figure 2.7: Processing of spectral data exemplified for λ=700 nm.

2.2.2.2 Data Processing

According to the Beer–Lambert law, the extinction of light at a certain wavelength in a medium is described by an exponential function. Here we assume that multiple scattering in meltwater and (multiple) reflections at the pond surface, bottom and sidewalls can be neglected to approximate the radiative transfer. Figure 2.7a illustrates the exponential decrease in R_{rs} with water depth at 700 nm for the five different bottom type mixtures. To linearize the effect, we computed the logarithm of the spectra (Figure 2.7b). Lastly, we computed the first derivative of the logarithmized spectra (Figure 2.7c) for each band by applying a Savitzky–Golay filter using a secondorder polynomial fit on a 9 nm window (The Scipy community, 2019b).

We then computed Pearson's correlation coefficient (r) as (The Scipy community, 2019c)

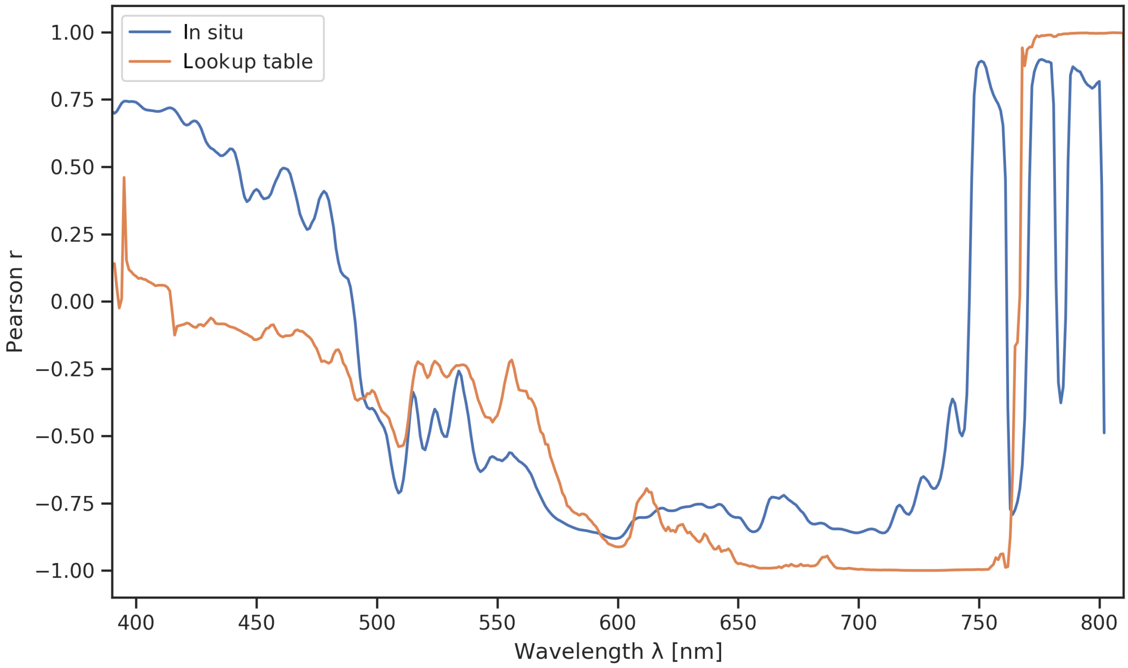

Figure 2.8: Wavelength-dependent correlation coefficients of pond depth with slope of log-scaled spectra for *in situ* measurements and simulated spectra.

$$r(x,y) = \frac{\sum_{i=0}^{n-1}(x_i - \acute{x})(y_i - \acute{y})}{\sqrt{\sum_{i=0}^{n-1}(x_i - \acute{x})^2 \sum_{i=0}^{n-1}(y_i - \acute{y})^2}} \tag{2.5}$$

where x_i and $\acute{x}$ are the depth of the ith sample and the average depth, y_i and $\acute{y}$ are the slope of the logarithmized reflectance at a certain wavelength of the ith sample and the average slope of the logarithmized reflectance at a certain wavelength, and n is the number of samples.

The orange curve in Figure 2.8 illustrates the wavelength-dependent correlation coefficients of the slope of the logarithmized spectra and pond depths in the LUT. We observe an almost perfect negative correlation in bands between 700 and 750 nm.We performed the same processing for the simulated spectra as for the *in situ* pond spectra. The blue curve in Figure 2.8 illustrates the wavelength-dependent correlation coefficients of measured pond depth and the slope of the logarithmized *in situ* spectra. We likewise observe strong negative correlations in the wavelength region around 700 nm.

To investigate the similarity of the dark and bright ice spectra, we normalized both bottom spectra at 710 nm and found a high spectral similarity between $\sim$ 590 and $\sim$ 800 nm (Figure 2.9). Consequently, the slope of the logarithmized spectra is widely independent from the chosen bottom albedo in this wavelength region. Assuming that this also applies to ice spectra recorded under clear sky conditions, we used the Ibsen bare ice measurement to develop a model for clear sky conditions accordingly.

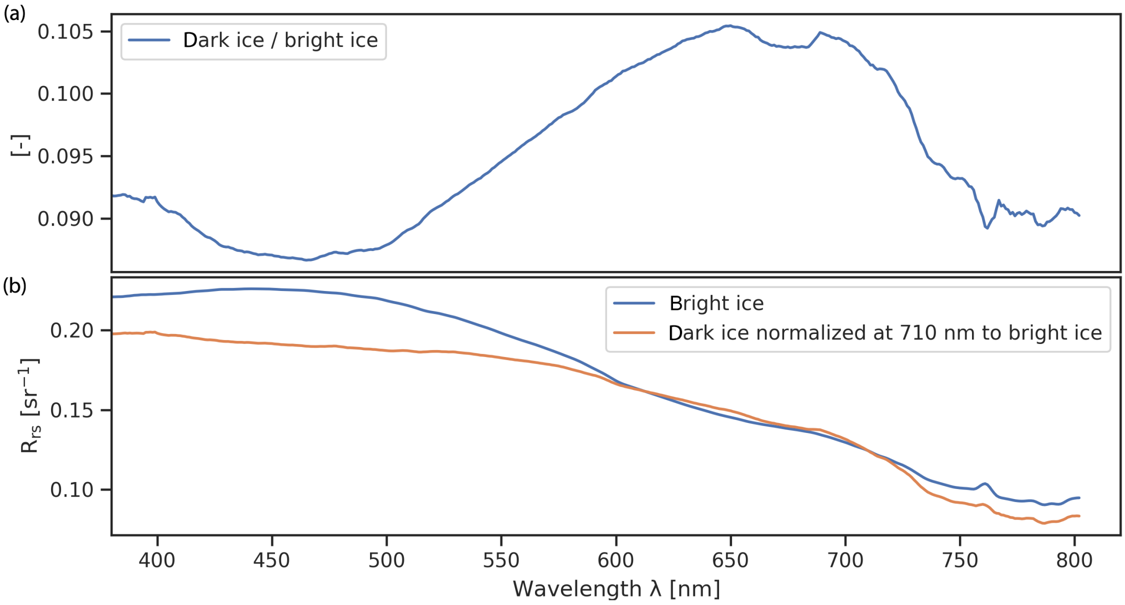

Figure 2.9: Quotient of bright and dark bare ice spectra (a) and R_{rs} of bright ice and dark ice normalized at 710nm (b).

2.2.2.3 Linear Model

Due to the strong negative correlation in the simulated as well as in the measured data, we chose the slope of the logarithmized spectrum at 710 nm (r = –1.0 and –0.86 for simulated and *in situ* data, respectively) to develop a simple linear model. We used scikit-learn's LinearRegression function (Pedregosa et al., 2011) to fit a linear model to the simulated data with the Ibsen bare ice spectrum as bottom albedo using the method of ordinary least squares.

We found that the solar zenith angle affects the slope and y intercept of the linear model. Because the model should be applicable to a wide range of solar zenith angles, we implemented a second model to derive the slope and y intercept of the linear model for various solar zenith angles. We used WASI to generate spectral libraries for different solar zenith angles (0, 15, 30, 45, 60, 75, 90°) and found that the resulting change in slope and y intercept can each be described by an s-shaped curve. We used SciPy's optimize.curve_fit function (The Scipy community, 2019a) to fit generalized logistic functions (Richards, 1959) into the data. Using these functions, the model's slope and y intercept can be computed for different solar zenith angles (Figure 2.10).

The model is

$$z = a(\theta_{\mathrm{sun}}) + b(\theta_{\mathrm{sun}}) \left[\frac{\partial \log R_{rs}(\lambda)}{\partial \lambda} \right]_{\lambda = 710\mathrm{nm}} \tag{2.6}$$

where z is the predicted pond depth and θ_{sun} is the solar zenith angle. a and b are offset and slope as follows:

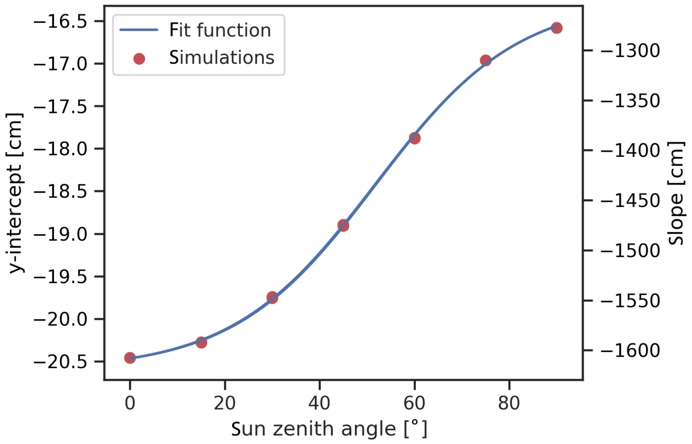

Figure 2.10: Change in model's y intercept and slope with solar zenith angle. Generalized logistic function fit into the simulated data.

$$a(\theta_{\text{sun}}) = -20.6 + \frac{0.79}{0.8 + 5.8\ \exp\ (-0.13 \cdot \theta_{\text{sun}})^{\frac{1}{2}}} (\text{cm}), \tag{2.7}$$

and

$$b(\theta_{\text{sun}}) = -1619.8 + \frac{94743.64}{255.3 + 7855\ \exp\ (-1.3 \cdot \theta_{\text{sun}})^{\frac{1}{19.9}}} (\text{cm}). \tag{2.8}$$

We further computed the coefficient of determination (R^2) as recommended by Kvålseth (1985) as

$$R^2(y, \hat{y}) = 1 - \frac{\sum_{i=0}^{n-1} (y_i - \hat{y}_i)^2}{\sum_{i=0}^{n-1} (y_i - \acute{y}_i)^2}, \tag{2.9}$$

where y_i and $\hat{y}_i$ are the true (simulated) and predicted values of the ith sample, n is the number of samples, and $\acute{y}_i = \frac{1}{n} \sum_{i=0}^{n-1} y_i$ (Pedregosa et al., 2011; scikit-learn developers, 2018b). In addition, we also computed the root mean square error (RMSE) as

$$RMSE(y, \hat{y}) = \sqrt{\frac{1}{n} \sum_{i=0}^{n-1} (y_i - \hat{y}_i)^2} \tag{2.10}$$

and the normalized RMSE (nRMSE) as

$$nRMSE(y, \hat{y}) = \frac{RMSE(y, \hat{y})}{\acute{y}} \cdot 100. \tag{2.11}$$

For the model described above, we obtained a perfect correlation (r = 1.0; probability value p = 8.9 $\times 10^{-172}$), an R^2 of 1.0 and an RMSE of 0.56 cm (nRMSE = 1 %) on the simulated training data.

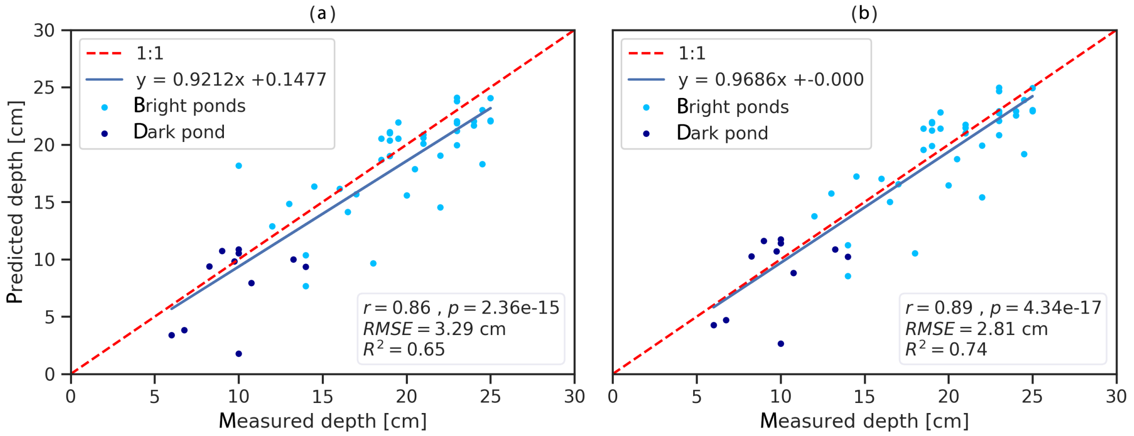

Figure 2.11: Measured versus predicted depth for the entire dataset (a) with outlier removed and offset correction (b).

2.3 Results

We validated the model with the *in situ* melt pond dataset from dark and bright ponds (Section 2.2.1.2) and observed a strong linear and statistically significant correlation (r = 0.86; $p = 2.36 \times 10^{-15}$; $R^2 = 0.65$; RMSE = 3.29 cm and nRMSE = 19 %). Most of the points scatter along the 1:1 line except for one point whose actual depth is 10 cm and predicted depth is 18 cm (Figure 2.11a). The externally studentized residual (t) (Kutner et al., 2004; Seabold and Perktold, 2010) classifies this point as an outlier ($t > 3$), and therefore we excluded this point from the dataset. The removal of the outlier improves all performance measures (r = 0.89; $p = 4.34 \times 10^{-17}$; $R^2 = 0.68$; RMSE = 3.11 cm; nRMSE = 18 %). The slope of the line of best fit increases to 0.9686, and the intercept indicates an offset of 0.878 cm. If we further correct for the offset, R^2 increases to 0.74 and RMSE improves to 2.81 cm (nRMSE = 16 %). The blue line is the line of best fit between actual and predicted pond depths. The linear equation of the line of best fit indicates that the model results in a small offset and a slope close to 1.0.

2.4 Discussion

Our results show that a simple model based on the derivative of the log-scaled R_{rs} at 710 nm allows water depth retrieval of dark and bright melt ponds on Arctic sea ice. The model training on simulated data and the independent testing using *in situ* measurements prove the applicability of our approach.

2.4.1 Observational Data

2.4.1.1 Spectral Measurements

Measurements of albedo have a long tradition in Arctic research (e.g., Grenfell and Perovich, 2004; Nicolaus et al., 2010; Perovich et al., 2002; Perovich and Polashenski, 2012) because albedo is an important quantity in climate models and can be measured with a single irradiance detector. In this study, we conducted measurements of R_{rs} because our model should be applicable to remote sensing data, and the quantity measured in optical remote sensing is radiance. It is only appropriate to derive an accurate radiance directly from the albedo of a Lambertian surface. This assumption, however, is not valid for specular water surfaces and may easily introduce errors. Morassutti and Ledrew (1996) identified changing E_d as the main error affecting reflectance data recording. To tackle this issue, we used a combination of two spectrometers described in Section 2.2.1.

Field spectroscopy is influenced by external factors and the measurement design itself. In contrast to ruler measurements, the spectrometer acquires information of an area. To ease comparison and limit the influence of spatial heterogeneities, we used a fore optic with a 1° field of view to minimize the footprint ($\sim$ 1 cm at a height of 60 cm). However, holding the instruments perfectly still for a period of several seconds is challenging, and even small changes in the position result in changes in the viewing angle, which increases the footprint of a measurement. For future campaigns, we therefore recommend using a gimbal to minimize the influence of roll and pitch of the handheld spectrometer setup. Another issue might have been reflections of the black spectrometer housings on the water surface possibly contributing to the offset between modeled and measured data.

Different refraction indices of wet and dry surfaces may cause part of the observed offset. Furthermore, using bottom albedos obtained from dry surfaces in WASI introduce a systematic offset. However, it remains unclear if the ice surface used to compute the spectral library was wet or dry.

Some of the scattering may be introduced by reflectances at the water surface, which we did not consider in the LUT computation because the necessary values for the parametrization are unknown. Another influence may be the different solar zenith angles between bare ice and pond measurements. The potential influence of the mentioned factors may be worth further examination to refine the model.

2.4.1.2 Pond Depth Measurements

Measuring the depth of a pond may appear trivial, but the bottom of a pond is frequently not flat and solid but can be slushy or riddled with holes. In addition, performing two measurements with a spectrometer and a folding ruler at the exact same location is difficult. We therefore recommend using a laser pointer at the end of the pole for orientation. These uncertainties explain some of the scattering in Figure 2.11. Interpretation of field photographs of the pond bottoms, however, did not indicate any systematic errors associated with pond bottom characteristics.

2.4.2 Model Validity

The majority of the field data used in this study are from bright blue ponds ($n = 38$), while fewer measurements were obtained in dark ponds ($n = 11$). We addressed this limited diversity of field data by computing a comprehensive LUT. The model generates accurate results (RMSE = 2.81 cm) on the entire *in situ* test dataset and explains a large portion of its variability ($R^2 = 0.74$). On the dataset from the dark pond, R^2 is less than 0 and nRMSE is 35 %. The reason is that measurements from the dark pond are very shallow (6–14 cm), and, thus, relative errors are larger compared to the deeper bright ponds. In addition, the number of data points is very small, and single outliers have a strong influence on performance metrics. The range of scattering around the 1:1 line (Figure 2.11), however, is similar for the data from dark (RMSE = 3.05 cm) and bright (RMSE = 2.49 cm) ponds, proving that the model's accuracy is similar for both subsets.

The data used in this study are the most comprehensive set of R_{rs} and depth measurements from melt ponds on Arctic sea ice acquired under clear sky conditions. The dataset, however, originates from only three ponds, covering a limited variability of bottom characteristics and pond depth. More validation data are desirable to explore the model capabilities to derive pond depth from deep dark and shallow bright ponds, for pond depth > 25 cm, and for a wider range of bottom types and solar zenith angles. In addition, more tests are necessary to explore how the model performs when the assumptions formulated in Section 2.2.2 are violated, e.g., when algae, suspended matter or yellow substances are abundant in the pond water or in the ice below the pond.

We successfully developed a model to accurately derive the depth of melt ponds on Arctic sea ice without having to consider the bottom ice characteristics of the pond; yet, we assume that we cannot entirely avoid any influence. When fitting a model to the Ocean Optics LUT (Figure 2.7c), we observe scattering around the 1:1 line resulting in an RMSE of 1.88 cm (nRMSE = 4 %). In the Ocean Optics LUT, however, the only variable parameter is bottom type mixture; we therefore conclude that the scattering results from the difference in bottom albedo. Consequently, bottom albedo may affect the model, which may explain some of the scattering in the test data.

Optical satellite data can only be obtained under clear sky conditions, but remote sensing images are likewise acquired from helicopters and unmanned aerial vehicles. These platforms also operate under diffuse illumination conditions, which are frequent in the Arctic. To check the validity of the model for overcast conditions, we applied the clear sky model to data from the same area acquired on 14 June 2017 during diffuse illumination conditions. The performance, however, is low (Figure 2.12) and shows a moderate correlation (r = 0.64; $p = 2.6 \times 10^{-4}$), an $R^2 < 0$ and an RMSE of 12.76 cm (nRMSE =

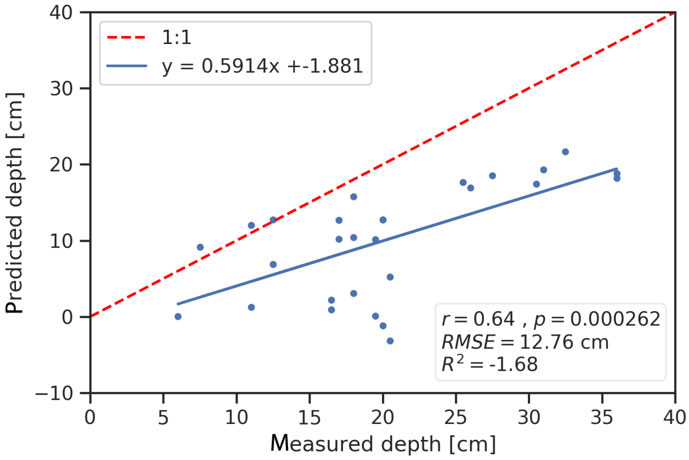

Figure 2.12: Measured versus predicted water depth for data acquired under overcast conditions on 14 June 2017.

63 %). We attribute the low performance to the different illumination conditions. Under diffuse conditions, a considerable part of the reflectance measured above the water surface is due to the reflection of clouds at the water surface. Further, the optical path length of the incoming light in water changes under overcast conditions.

We therefore conclude that the present model is only valid for clear sky conditions. The model accounts for the influence of varying solar zenith angles, but field data were limited to solar zenith angles between 58.9 and 61°. To enlarge its validity range, more field data covering different weather and illumination conditions are necessary.

2.5 Conclusion

We present a linear model slope-based approach in the spectral region around 710 nm to retrieve the depth of melt ponds on Arctic sea ice. However, the model is not restricted to Arctic sea ice and may be tested in shallow supraglacial ponds as well. The model calibration on simulated data and independent validation on *in situ* data prove the applicability and robustness of our approach. The final model is valid for hyperspectral data (R_{rs}) acquired under clear sky conditions and addresses varying solar zenith angles.

We used WASI to generate a LUT of pond spectra for five different bottom albedos and pond depths between 0 and 100 cm assuming clear pond water. We found that the slope of the log-scaled R_{rs} at 710 nm is widely independent from the bottom albedo and highly correlated with pond depth. Thus, we applied a linear model to retrieve pond depth from R_{rs} in this wavelength region. The slope and y intercept of the linear equation, however, change with the solar zenith angle for which other models do not account for (e.g., Legleiter et al., 2014; Tedesco and Steiner, 2011). To overcome this limitation, we trained linear models for seven solar zenith angles in between and found that a general logistic function is able to describe the change in slope and y intercept for each solar zenith angle. The inputs for our model, therefore, are the slope of the log-scaled $R_{rs}^{\lambda=710}$ and sun zenith angle. We successfully validated the model on *in situ* measurements (r = 0.89; R^2 = 0.74; RMSE = 2.81 cm; *n*RMSE = 16 %) with solar zenith angles between 58.9 and 61° and observed similar accuracies for bright and dark ponds.

The next step is the transfer to hyperspectral airborne and satellite systems, e.g., EnMAP (Guanter et al., 2016), to enable a synoptic view on the evolution of melt ponds on Arctic sea ice. One constraint may be the size of melt ponds, which requires a high spatial resolution. We further assume that the additive signals of the atmosphere and reflections of skylight at the water surface may complicate the retrieval of pond depth with remote sensors. In addition, the sensitivities and band settings of remote sensors also affect the transferability of our approach. Here, further testing and comprehensive ground truth data are necessary. In these regards, we expect the Multidisciplinary drifting Observatory for the Study of Arctic Climate (MOSAiC) expedition to result in further improvements.

Acknowledgements

We thank Peter Gege for his encouragement and the provision of WASI. We highly appreciate the support of the German Aerospace Center (DLR) Oberpfaffenhofen and especially thank Thomas Schwarzmaier, Stefan Plattner and Peter Gege for the development and provision of the instruments used in this study. We further acknowledge the support of captain Thomas Wunderlich, the crew, and the chief scientists, Andreas Macke and Hauke Flores, of RV *Polarstern* cruise AWI_PS106_00, as well as the assistance provided by the colleagues supporting our fieldwork on PS106 especially Peter Gege, Gerit Birnbaum, Niels Fuchs, Martin Hieronymi and Thomas Ruhtz. We would also like to thank Justin Mullins at Write About Science for his valuable comments and Marcel Nicolaus for his estimation of the pond site's ice type situation. Finally, we thank two anonymous referees for their constructive critique, which helped us to improve the paper, and Stef Lhermitte for his editorial efforts.

Chapter 3

Mapping the Bathymetry of Melt Ponds on Arctic Sea Ice Using Hyperspectral Imagery

M. König, G. Birnbaum and N. Oppelt

Remote Sensing (2020), doi:10.3390/rs12162623
Received: 2 July 2020 - Revised: 7 August 2020 - Accepted: 11 August 2020 - Published: 14 August 2020

Abstract. Hyperspectral remote sensing instruments on unmanned aerial vehicles (UAVs), aircraft and satellites offer new opportunities for sea ice observations. We present the first study using airborne hyperspectral imagery of Arctic sea ice and evaluate two atmospheric correction approaches (ATCOR-4 (Atmospheric and Topographic Correction version 4; v7.0.0) and empirical line calibration). We apply an existing, field data-based model to derive the depth of melt ponds, to airborne hyperspectral AisaEAGLE imagery and validate results with *in situ* measurements. ATCOR-4 results roughly match the shape of field spectra but overestimate reflectance resulting in high root-mean-square error (RMSE) (between 0.08 and 0.16). Noisy reflectance spectra may be attributed to the low flight altitude of 200 ft and Arctic atmospheric conditions. Empirical line calibration resulted in smooth, accurate spectra (RMSE < 0.05) that enabled the assessment of melt pond bathymetry. Measured and modeled pond bathymetry are highly correlated ($r = 0.86$) and accurate (RMSE $= 4.04$ cm), and the model explains a large portion of the variability ($R^2 = 0.74$). We conclude that an accurate assessment of melt pond bathymetry using airborne hyperspectral data is possible subject to accurate atmospheric correction. Furthermore, we see the necessity to improve existing approaches with Arctic-specific atmospheric profiles and aerosol models and/or by using multiple reference targets on the ground.

3.1 Introduction

From May to September, evolution and refreezing of melt ponds at the sea ice surface dramatically changes the energy and momentum exchange between atmosphere and ocean in the Arctic. Melt ponds have a substantially lower albedo than bare ice or snow and significantly affect the heat and mass balance of sea ice (e.g. Taylor, 2004); therefore, they are considered the main driver of the ice-albedo feedback mechanism (Curry et al., 1995). Moreover, the amount of radiative energy stored in ponds and open water governs the onset of freezing in autumn (Kwok and Untersteiner, 2011). Likewise, melt ponds increase the amount of photosynthetically active radiation transmitted through the ice into the upper ocean up to a factor of about four (Arrigo et al., 2012; Light et al., 2015; Nicolaus et al., 2012; Ehn et al., 2011) fostering primary production (Arrigo et al., 2012; Horvat et al., 2017), warming of the upper ocean layer (Inoue et al., 2008b), and bottom ice melt (Perovich and Polashenski, 2012).

The temporal evolution of melt ponds is characterized by a strong seasonality and generally follows the surface metamorphism and change of phases from dry to melting snow, pond formation, pond drainage, pond evolution, and fall freeze-up (Perovich and Polashenski, 2012; Nicolaus et al., 2010).

Melt pond coverage, i.e., areal fraction of melt ponds on sea ice, depends significantly on sea ice surface topography which is in turn strongly influenced by deformation and aging processes, snow cover and ice permeability (Eicken et al., 2004). Undeformed first-year ice is characterized by a homogeneous snow cover enabling lateral spreading of shallow ponds (Perovich et al., 2002; Webster et al., 2015), with pond depth mostly < 50 cm (Morassutti and Ledrew, 1996; Yackel et al., 2000), and cover up to 80 % of the ice surface (Nicolaus et al., 2012; Fetterer and Untersteiner, 1998). Multi-year ice shows a preexistent hummocky topography that controls snow depth distribution and lateral pond spreading (Eicken et al., 2004; Morassutti and Ledrew, 1996), and a low permeability that retains meltwater at the ice surface (Webster et al., 2015). Melt ponds on multi-year ice are generally smaller (Yackel et al., 2000; Fetterer and Untersteiner, 1998) and deeper than those on first-year ice, reaching depths of ~ 70 cm (Morassutti and Ledrew, 1996; Yackel et al., 2000), and pond coverage is usually smaller than 40 % (Nicolaus et al., 2012). In contrast to drifting ice, land-fast ice is influenced by coastal processes, e.g., tides, that result in a rugged, sharply edged surface topography facilitating accumulation of drifting snow and formation of small and deep ponds (Webster et al., 2015; Morassutti and Ledrew, 1996). Terrestrial influences such as warm air and dust input further influence the temporal and spatial evolution of melt ponds (Webster et al., 2015). The recent decline of the Arctic sea ice cover in size (Serreze et al., 2007) and thickness (Comiso, 2012) accompanies the loss of old multi-year ice and the trend towards a more seasonal ice cover (Nicolaus et al., 2012; Kwok et al., 2009; Maslanik et al., 2011) associated with increased pond coverage (Scharien et al., 2014; Roeckner et al., 2012).

Remote sensing is the primary tool for observations of Arctic sea ice because *in situ* campaigns are cost- and labor-intensive and spatially limited. Remote sensing offers the possibility to obtain synoptic information on a more or less regular basis. At large spatial scales, melt pond coverage is routinely observed with medium resolution optical sensors such as MODIS or Sentinel-3/OLCI (e.g., Istomina et al., 2015b; Rösel et al., 2012; Tschudi et al., 2008). Detailed observations of melt pond geometries are possible with higher resolution optical data (Webster et al., 2015; Fetterer and Untersteiner, 1998; Markus et al., 2003, 2002; König et al., 2019; Wright and Polashenski, 2018) or synthetic aperture radar (Kim et al., 2013). Besides satellite observations, airborne campaigns with planes (Yackel et al., 2000; Markus et al., 2003; Wright and Polashenski, 2018; Hanson, 1961; Holt and Digby, 1985; Tschudi et al., 2001; Birnbaum et al., 2009) and helicopters (Perovich et al., 2002; Langleben, 1971; Tschudi et al., 1997; El Naggar et al., 1998; Tucker et al., 1999; Hanesiak et al., 2001; Perovich and Tucker, 1997; Skyllingstad et al., 2009; Lu et al., 2010; Huang et al., 2016; Divine et al., 2015; Miao et al., 2015; Istomina et al., 2016) provide observations of melt pond coverage on a sub-meter scale. Others installed cameras on towers (Langleben, 1969), tethered balloons (Derksen et al., 1997) or research vessels (Sankelo et al., 2010). Tschudi et al. (2008), Maslanik et al. (2002), Inoue et al. (2008a) and Mingfeng et al. (2018) used unmanned aerial vehicles (UAVs) to observe of melt pond coverage, whereby the recent technical development in this field may facilitate the future of aerial melt pond observations (Gaffey and Bhardwaj, 2020; Watts et al., 2012).

The studies mentioned above focused primarily on melt pond coverage; a comprehensive understanding of melt pond evolution, however, requires information about the two-dimensional areal development and pond depth. The latter governs the transmittance of shortwave solar radiation into the ice and upper ocean layer (Inoue et al., 2008b; Ebert et al., 1995) and determines the albedo of melt pond covered sea ice (Morassutti and Ledrew, 1996; Ebert and Curry, 1993). Therefore, pond depth is an important parameter in the treatment of radiative transfer in sea ice models (Hunke et al., 2013; Flocco and Feltham, 2007; Scott and Feltham, 2010) and global climate models (Flocco et al., 2010; Holland et al., 2012; Pedersen et al., 2009) used, for example, for the prediction of sea ice extent and thickness.

Pond depth is often recorded in field studies (e.g. Morassutti and Ledrew, 1996; Eicken, 1994) but these data sets are limited to few observations per pond and logistically challenging; however, remote sensing based approaches to map the two-dimensional bathymetry of melt ponds are scarce. The authors are only aware of Divine et al. (2016) who used UAV red, green and blue (RGB) stereovision to map the bathymetry of melt ponds north of Svalbard.

Another technology that enables bathymetry mapping is hyperspectral imaging. An approach was successfully developed by Legleiter et al. (2014) and Moussavi et al. (2016) to derive the depth of supraglacial lakes on the Greenland ice sheet based on hyperspectral field data. Their approach showed a standard error of 47 cm for lake depth between 0.31

m and 10.45 m. Supraglacial lakes and ponds on sea ice, however, differ significantly regarding depth range and bottom ice properties. While supraglacial lakes may be several meters deep (e.g., Legleiter et al., 2014; Tedesco and Steiner, 2011), melt ponds on sea ice reach maximum depths of ~ 1 m (Untersteiner, 1961). Considering this range of depths, a standard error of 0.47 m would be insufficient for a remote sensing based retrieval of melt pond depth. Moreover, in optically shallow waters, the optical properties of the bottom influence the water leaving radiance. While the subjacent ice in supraglacial lakes may be hundreds of meters thick, the bottom of ponds on sea ice may be optically thin, i.e., the signal may be influenced by ice thickness.

The shallowness of melt ponds on Arctic sea ice is a challenge for classic depth retrieval, because pond albedo in the visible wavelength region of the electromagnetic spectrum (VIS) is primarily defined by pond bottom characteristics (Lu et al., 2016). RGB images are, therefore, unsuitable to map melt pond bathymetry (Lu et al., 2018). To overcome this issue, König and Oppelt (2020) used bands around 710 nm where pond depth is the main factor influencing pond albedo (Lu et al., 2016). Their model is calibrated on simulated data to avoid any bias due to the limited comprehensiveness of field data. It is designed to be widely independent of the pond bottom albedo and sun zenith angles, and has been validated on hyperspectral field data.

Although airborne hyperspectral imagery has been used to map the bathymetry of coastal environments (e.g. McIntyre et al., 2006), rivers (e.g. Legleiter et al., 2016, 2009) and lakes (e.g. Giardino et al., 2015), similar applications for melt ponds on sea ice are still missing. In this paper, we present the first application of airborne hyperspectral imagery in Arctic sea ice and investigate whether the model presented in König and Oppelt (2020) can be applied to these data. We describe the processing steps needed to derive maps of melt pond depth, i.e., melt pond bathymetry, and further discuss how the data processing, especially atmospheric correction, affects results and how field sampling influences calibration and validation of remote sensing products in Arctic sea ice.

3.2 Materials and Methods

We applied the model by König and Oppelt (2020) to atmospherically corrected, airborne hyperspectral imagery acquired with an AisaEAGLE sensor covering the wavelength region between 400 nm and 970 nm (see Section 3.2.2 for details), and validated results using *in situ* pond depth measurements. We compare two atmospheric correction approaches and evaluate their performances using field data. In order to evaluate the performance of the pond depth model, we validate calculated pond depths using field measurements and inspect bathymetry maps for plausibility.

3.2.1 Field Data

For this study, we gathered the data during RV *Polarstern* cruise PS106 as part of an 11-days ice station north of Svalbard (Macke and Flores, 2018, see also Figure 3.1). Melting had just begun and most of the floe was still snow-covered but some ponds had already formed in ridged terrain. We sampled four ponds on 10 June 2017. Figure 3.1 also illustrates that the ponds differed in color: Ponds 2 and 3 were bright blueish, Pond 4 was dark grey-blue, while Pond 1 was split into a dark and a bright half. The ice floe consisted mostly of first-year and, to a lesser degree, of second-year ice. Occasional ice thickness measurements from 14 June 2017 show that the bottom of the bright ponds was thicker (≥ 0.9 m) than the dark pond's bottom (≤ 0.4 m), indicating that ponds 2 and 3 may have been located on older ice while the ice below Pond 4 may have been younger. However, no ice cores were sampled at the pond site, prohibiting a reliable statement about ice type.

3.2.1.1 Pond Measurements

We performed measurements of pond depth ($n = 60$) either from the edge of a pond (Ponds 1, 2 and 4) or while wading through (Pond 3) using a folding ruler. Measured depth ranged between 1.3 cm and 25.0 cm. As described in König and Oppelt (2020), the measurement of pond depth is not trivial as the bottom of a pond may be highly variable, e.g., solid, slushy or riddled with holes and cracks, and may change on centimeter scales. At every point, we also measured remote sensing reflectance over the water surface (König and Oppelt, 2019). The measurement setup consisted of two Ocean Optics STS-VIS spectrometers (Ocean Optics Inc., Douglas Avenue Dunedin, FL, USA). One downwards pointing spectrometer equipped with a 1° fore optic that we referenced with a Labsphere Spectralon 99 % diffuse reflectance standard (Labsphere Inc., North Sutton, NH, USA) to acquire remote sensing reflectance; and a second, upwards pointing spectrometer equipped with a cosine collector to track changes in downwelling irradiance. We used the latter to correct the data acquired with the first spectrometer. Both spectrometers cover the wavelength region from ~ 340 nm to ~ 820 nm with a sampling interval < 1 nm and a spectral resolution of 3 nm (Ocean Optics, 2019). We sampled ponds 2–4 under clear sky conditions between 11:45 UTC and 14:05 UTC and pond 1 under variable illumination conditions between 17:10 UTC and 17:30 UTC.

3.2.1.2 Measurement Localization

On a drifting ice floe, the accurate localization of measurements taken at different times inside a high-spatial resolution remote sensing image is a major challenge and small errors in localization may result in large errors when comparing derived and measured water depth. We used handheld Global Positioning System (GPS) devices to track our position on the floe and intended to correct the ice drift by using a triangulation technique with three stationary GPS devices as described in König et al. (2019). Spatial accuracy of

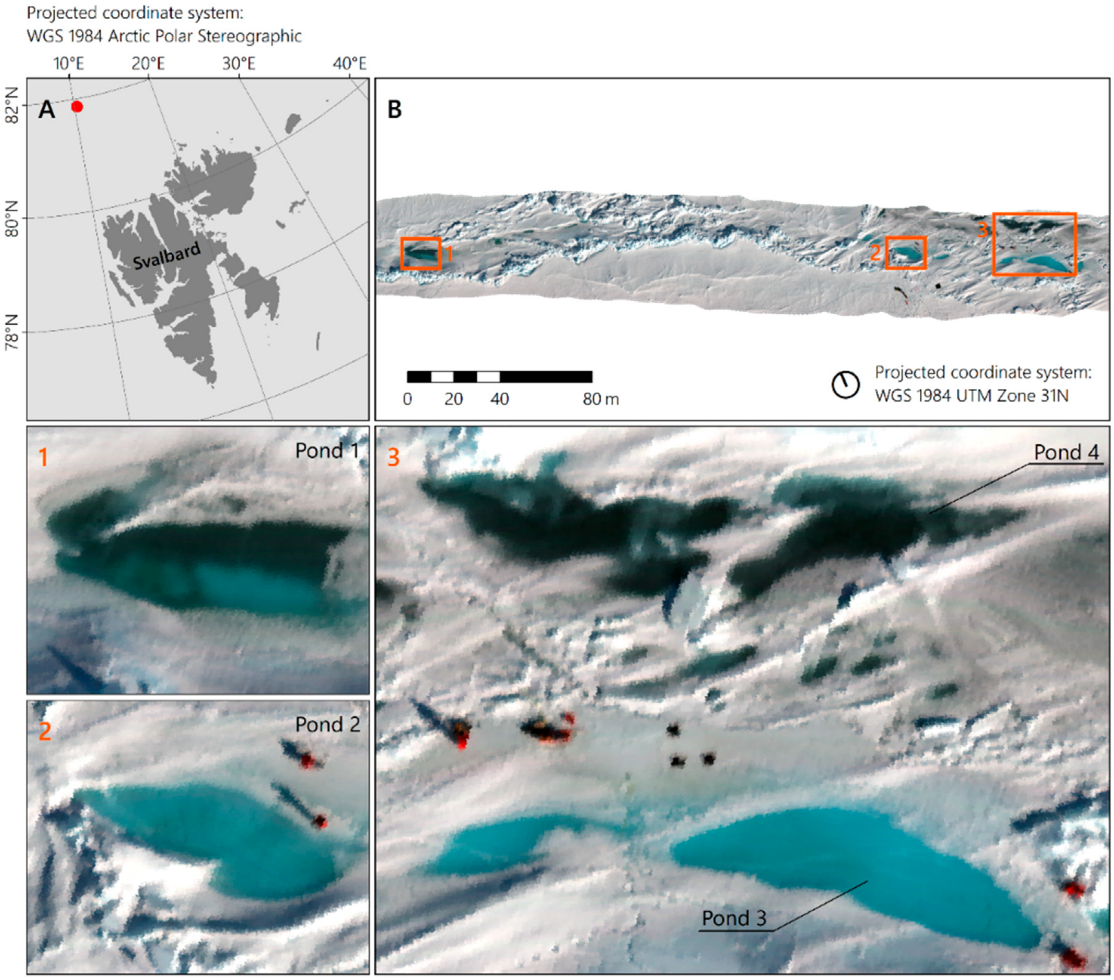

Figure 3.1: Study area. (A) Location in the Arctic Ocean. The red dot indicates the location of (B). (B) Subset of AisaEAGLE flight stripe containing the surveyed ponds. (1) Subset of Pond 1. (2) Subset of Pond 2. (3) Subset of Ponds 3 and 4. Background: AisaEAGLE flight stripe (spatial resolution: 8.5 cm, red, blue and green (RGB): 661.16 nm, 550.25 nm, and 482.57 nm).

the corrected locations, however, was insufficient. Therefore, we localized measurement positions in the AisaEAGLE images manually by thoroughly interpreting measurement logs and field photographs.

In Pond 3, we installed a cord system that facilitated reconstruction of measurement locations. We measured pond depth at equal distances of 100 cm along the cords that were tied to wooden sticks, which could be identified in an airborne image. We registered the image to the georeferenced hyperspectral data manually using prominent image features as control points. Knowing the distance of each measurement location to the ends of the respective cord, we were able to locate measurements in the hyperspectral image accurately.

We used a flagging system to provide information about the spatial localization uncertainty. Localization is very certain for measurements along the cord system, quite certain for measurements close to prominent sea ice features that are apparent on field photographs and in remote sensing imagery, and less certain otherwise. To address the uncertainty, we buffered each measurement position with a radius of 20 cm for the very certain, 30 cm for the quite certain, and 40 cm for the less certain measurements. For each spatial buffer we computed the mean and standard deviation of all pixels whose center is located within. Figure 3.2 presents buffered measurement locations and measured pond depths. Pond color and measured depth in Ponds 3 and 4 further show that visual pond color is primarily influenced by the optical properties of the pond bottom and not by pond depth.

3.2.1.3 Spectral Reference Measurements

To assess the quality of the atmospheric correction, we placed a 2 × 2 m^2 reference target made of black awning fabric on the ice. The target's reflectance has been determined in the laboratory with an ASD LabSpec5000 spectrometer (Analytical Spectral Devices Inc., Boulder, CO, USA) covering the wavelength region from 350 nm to 2500 nm with a 1 nm spectral sampling rate and equipped with contact probe.

At 14:35 UTC, we measured the nadir reflectance of an ice surface covered by the AisaEAGLE data using the same spectrometer and a bare fiber with a 23° field of view (FOV) mounted to a pistol grip. For both measurements we used a 95 % diffuse Labsphere Spectralon reflectance standard (Labsphere Inc., United States) as white reference. We resampled both spectra to AisaEAGLE bands using the sensor's spectral response functions and central wavelengths. Figure 3.3 illustrates the location of both spectral targets and the corresponding field reflectance spectra. The polygons of the black and white target contain 362 and 73 pixels, respectively.

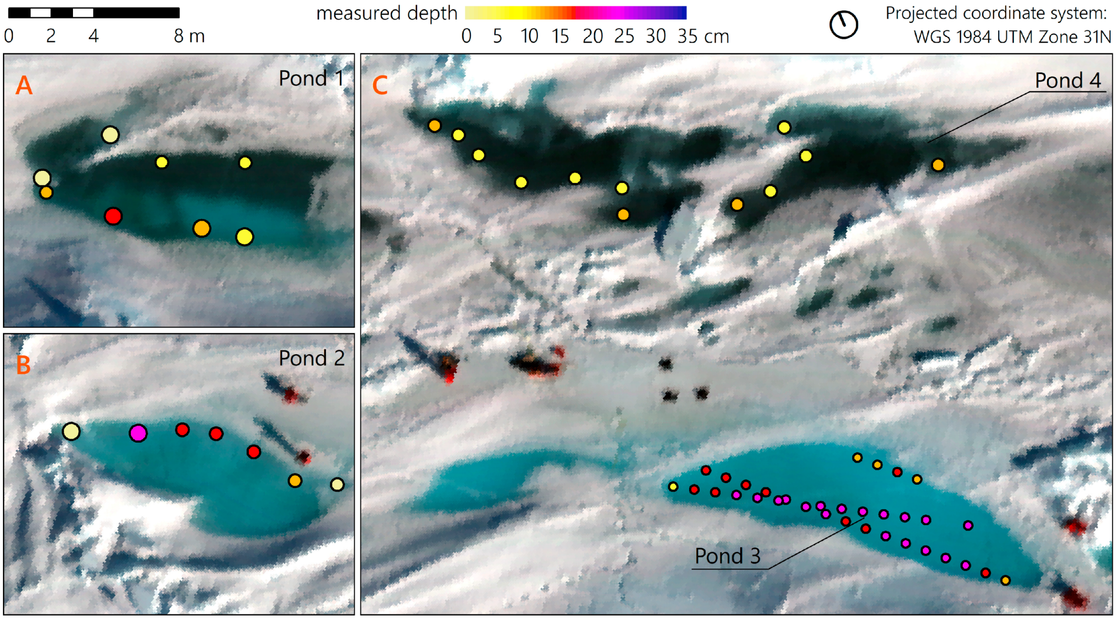

Figure 3.2: *In situ* depth measurement locations. Circle sizes correspond to estimated spatial uncertainties (radii are 20 cm, 30 cm and 40 cm). (A) Pond 1. (B) Pond 2. (C) Ponds 3 and 4. Background: AisaEAGLE flight stripe (spatial resolution: 8.5 cm, RGB: 661.16 nm, 550.25 nm, and 482.57 nm).

3.2.1.4 Measurements of Atmospheric Parameters

Between 14:42 and 15:21 UTC, sun photometer measurements were conducted on board of RV *Polarstern* some 800 m away. Measurements are published in the Maritime Aerosol Network (AERONET-MAN, Holben et al., 1998) and provide aerosol optical thickness at five wavelengths (440 nm, 500 nm, 675 nm, 870 nm and 1020 nm), Angstrom Exponent between 440 nm and 870 nm as well was water vapor column height. From the sun photometer measurements, we computed the aerosol optical thickness (AOT) at 550 nm (β) as (Equation 3.1):

$$\beta = \frac{AOT_{\lambda}}{(\frac{\lambda}{500})^{-\alpha}} \tag{3.1}$$

where AOT_{λ} is the mean AOT at λ (500 nm) and α is the mean Angstrom exponent between 440 nm and 870 nm. Table 3.1 summarizes the atmospheric parameters.

3.2.2 Remote Sensing Data

To our knowledge, this is the first study presenting airborne hyperspectral imagery from Arctic sea ice. We used hyperspectral data acquired with an AisaEAGLE sensor (Specim, Spectral Imaging Ltd., Oulu, Finland) owned by Alfred Wegener Institute, Helmholtz Center for Marine and Polar Research. The sensor was mounted on a platform especially

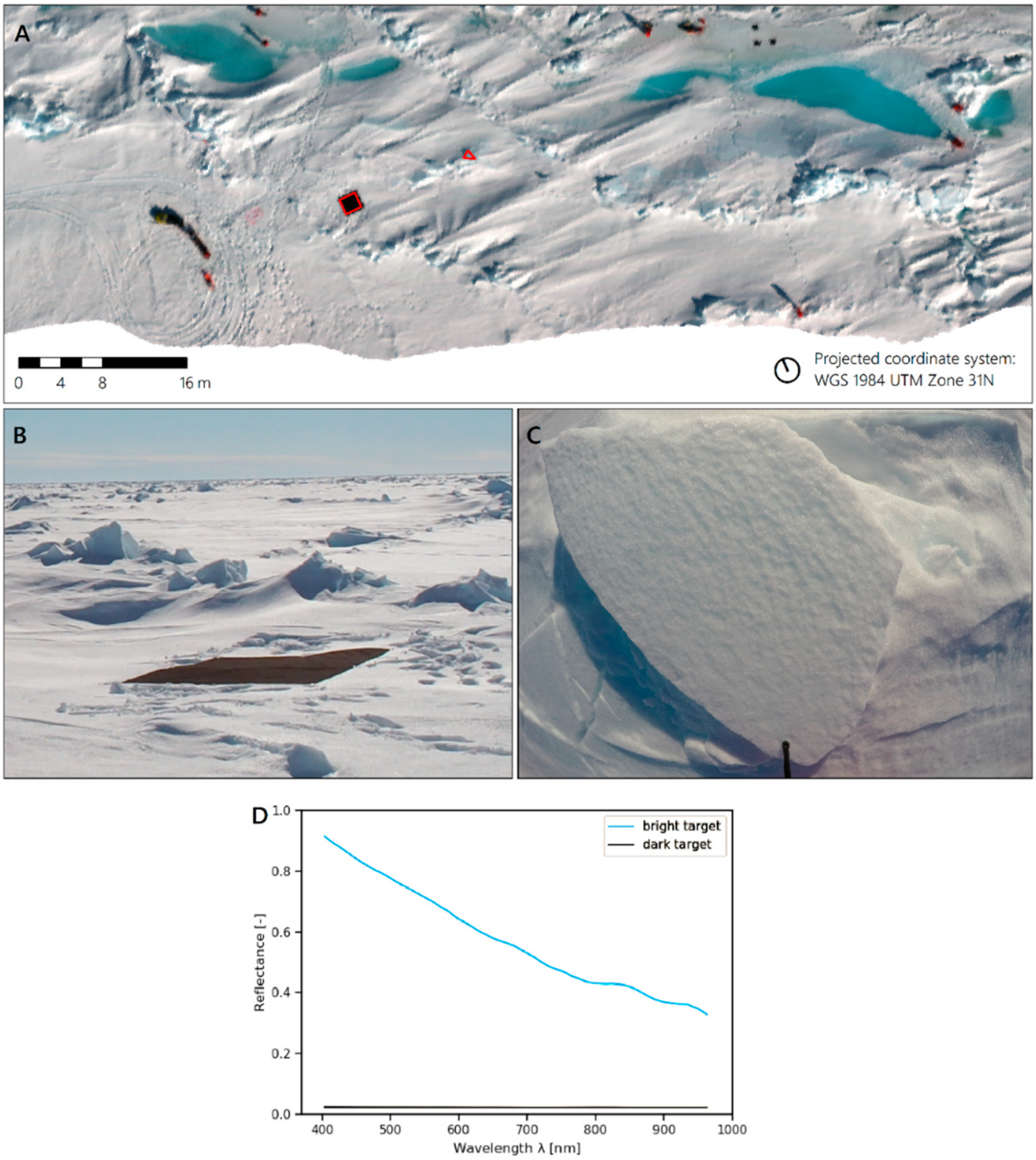

Figure 3.3: Location of reference measurements. (A) illustrates the location of the black target and the ice surface (red polygons) within the flight stripe; Background: AisaEAGLE flight stripe (spatial resolution: 8.5 cm, RGB: 661.16, 550.25, and 482.57 nm). (B) is a photo of the black target (Photo: Peter Gege). (C) is a photo of the reference ice surface. (D) illustrates the resampled spectral signatures of the black target and the bright reference site, respectively.

Table 3.1: Atmospheric parameters from Maritime Aerosol Network (AERONET) Microtops Level 2.0 data.

Parameter	**Unit**	**Minimum**	**Mean (± Standard Deviation)**	**Maximum**
Aerosol optical thickness at 550 nm	[-]	0.0217	0.0231 (± 0.0029)	0.0317
Angstrom Exponent (440 nm - 810 nm)	[-]	0.2168	1.0656 (± 0.4086)	1.6412
Water vapor	cm	1.1066	1.1415 (± 0.0226)	1.1881

designed for BK117-C1 helicopters, which are operated on RV *Polarstern* by HeliService International GmbH.

The sensor is a progressive scanner based on a charge-coupled device (CCD) array with 1024 spatial pixels and covers the spectral region from 400 nm to 970 nm with a FOV of 37.42° (Specim Spectral Imaging Ltd.). A fourfold spectral binning resulted in 130 spectral bands with an average full width half-maximum (FWHM) of 4.6 nm. On 10 June 2017, a helicopter flight covering the pond area was performed under clear-sky conditions. Hyperspectral data was recorded between 11:39 UTC and 11:53 UTC at a flight height of 200 ft and at a ground speed of 10 kn, the corresponding sun zenith angle was 58.9°. A twofold spatial binning resulted in a ground sampling distance of 8.5 cm.

The Aisa system was equipped with an RT3100 inertial and GPS measurement system (Oxford Technical Solution Ltd., Bicester, UK). It is a combination of a Global Navigation Satellite System (GNSS) to provide GPS position and altitude while a 3-axial inertial measurement unit (IMU) is used to provide the orientation in 3-D space with a roll/pitch accuracy of 0.05° and a heading accuracy of 0.1°.

Radiometric and Geometric Preprocessing

12-bit raw data [-] were converted to at-sensor spectral radiances [W/(m^2 nm sr)] by applying the sensor's radiometric calibration coefficients. Since the data showed noticeable striping, we applied a vertical stripe removal from the Spectral Processing Exploitation and Analysis Resource (SPEAR) toolbox in ENVI (Exelis Visual Information Solutions Inc., United States; v5.4.1).

Usually, the AisaEAGLE is equipped with a Fiber Optic Downwelling Irradiance Sensor (FODIS) to track changes in downwelling irradiance [W/(m^2 nm)] and to compute at-sensor remote sensing reflectance [sr^{-1}] (R_{rs}). Measurements of downwelling irradiance, however, were influenced by rotor blade interference and partial coverage of the sensor's hemisphere by the helicopter, which prevented the use of the FODIS data.

A geographic lookup table (GLT) containing the pixel's location in the WGS84 UTM zone 31N projected coordinate system was created with CaliGeo (4.9.5) software (Specim, Spectral Imaging Ltd., Finland) using the IMU and GPS measurements.

3.2.3 Atmospheric Correction

The accurate removal of effects due to atmospheric absorption and scattering is required to produce measures of surface reflectance. In general, complex radiative transfer models are used to simulate the incoming solar irradiance, subsequent atmospheric effects and the final at-sensor radiance; atmospheric effects can then be eliminated and surface reflectance spectra derived. Atmospheric correction is a common preprocessing step and use of an appropriate, thorough correction is of great significance for interpretation of hyperspectral imagery and any subsequent processing (Mahiny and Turner, 2007).

On 10 June 2017, high pressure areas over Barents Sea and Svalbard caused the predominant subsidence temperature inversion reaching the ground. Prevailing low stratus clouds vanished and temperatures reached +2 °C (Macke and Flores, 2018). The operator considered the atmospheric conditions during the flight as clear and calm, with blue sky conditions. Sun photometer measurements confirmed a low aerosol particle concentration as common over the inner Arctic sea ice in summer (Kupiszewski et al., 2013) where absolute humidity is usually low (Andreas, 2002). The low flight altitude of 200 ft reduces the influence of atmospheric absorption and scattering. However, adjacency effects may be strong in the contrast-rich sea ice environment (Bélanger et al., 2007). To provide remote sensing data in units of surface R_{rs}, we applied two different atmospheric correction techniques, i.e., an approach based on a radiative transfer model and an empirical line based method.

3.2.3.1 Atmospheric and Topographic Correction Version 4 (ATCOR-4)

We used ATCOR-4 (Atmospheric and Topographic Correction version 4; v7.0.0), which is an established standard for atmospheric correction of wide FOV optical and thermal airborne remote sensing imagery (Markelin et al., 2012). Atmospheric correction is performed by inversion of a look up table (LUT) pre-compiled with the Moderate Resolution Atmospheric Radiance and Transmittance Model–version 5 (MODTRAN 5) (Berk et al., 2008) radiative transfer model. ATCOR-4 enables the correction of adjacency effects and has the advantage that aerosol type and maps of aerosol optical thickness and water vapor may be derived from the imagery if a sensor offers appropriate spectral bands and the image contains the required surface types (Richter and Schläpfer, 2015).

In the absence of a digital ice surface model, we used ATCOR-4 for flat terrain to perform atmospheric correction on the radiometrically corrected image. We resampled the LUT to the AisaEAGLE bands using the sensor's spectral response functions and turned off the band interpolation in the wavelength 725/825 nm water vapor region. We increased the thresholds to compute the cloud mask in the blue-green wavelength region and the water mask in the near infrared to the respective maximum values of 80 % and 12 % and used the land-average water vapor (WV) for water pixels. Because an image-based retrieval of aerosol type is not possible for flight altitudes below 1 km, we manually defined a maritime aerosol type. We selected an atmospheric file with a flight altitude of 0 km above sea level that was later interpolated to a flight altitude of 0.1 km. Based on flight altitude we defined an adjacency range of 0.006 km according to (Richter and Schläpfer, 2015). The small amount of dark pixels in the image prohibited the computation of a variable visibility map. The image based visibility estimation resulted in a visibility of 100 km. We used the 820 nm region with band regression to compute a WV map before performing image processing. Eventually, we used the GLT to georeference the atmospherically corrected image. The output image is in units of surface reflectance [% · 100] per band [µm]. For the follow-up processing, we converted the data into surface reflectance [-] per band [nm].

3.2.3.2 Empirical Line Calibration

In general, empirical line calibration produces very accurate results if ground-truth information is available. We first used the GLT to georeference the radiometrically corrected image and then used the empirical line calibration in the Tactical Hyperspectral Operations Resource (THOR) Atmospheric Correction Workflow in ENVI that requires one bright and one dark target with known reflectance located in the image. Here, we used the laboratory measurement of the black target, the field measurement of the ice surface and the reflectance measurements of the regions of interest displayed in Figure 3.3. The output image is in units of surface reflectance [-] per band.

3.2.4 Retrieval of Melt Pond Depth

To develop a model that is widely independent of the bottom albedo and robust against bias induced through the sample characteristics, König and Oppelt (2020) computed a library of melt pond spectra for five different bottom albedos and pond depths between 0 and 100 cm using the Water Color Simulator (WASI) (v4.1) (Gege, 2004, 2014, 2015). They log scaled the spectra to account for the exponential absorption of light in water and computed the slope at each band by applying a Savitzky–Golay filter. The final model uses the 710 nm band and accounts for changing slope and y-intercept of the linear equation resulting from changing sun zenith angles. They validated the model using *in situ* R_{rs} data generating a high accuracy (root mean squared error (RMSE) = 2.81 cm). Simulated and measured pond depths were highly correlated (r = 0.89), and the model explained a large amount of the depth variations ($R^2 = 0.74$) (König and Oppelt, 2020).

To convert the remote sensing data from surface reflectance into R_{rs}, we divided the data by π. Then we linearly interpolated bands in 1 nm steps and applied a rolling mean filter with a window size of 5 nm, log-scaled each spectrum and computed the slope at each band by applying a Savitzky–Golay filter using a second order polynomial fit with a window length of 27 nm. We then applied the model of König and Oppelt (2020) to the data (Equation (3.2)):

$$z = a(\theta_{\text{sun}}) + b(\theta_{\text{sun}}) \left[\frac{\partial \text{log} R_{rs}(\lambda)}{\partial \lambda}\right]_{\lambda=710\text{nm}} - 0.878, \tag{3.2}$$

with z being the predicted pond depth and θ_{sun} being the sun zenith angle. Offset (a) and slope (b) are computed as (Equations 6.3 and 6.4):

$$a(\theta_{\text{sun}}) = -20.6 + \frac{0.79}{0.8 + 5.8 \text{ exp } (-0.13 \cdot \theta_{\text{sun}})^{\frac{1}{2}}} \text{ [cm]}, \tag{3.3}$$

and

$$b(\theta_{\text{sun}}) = -1619.8 + \frac{94743.64}{255.3 + 7855 \text{ exp } (-1.3 \cdot \theta_{\text{sun}})^{\frac{1}{19.9}}} \text{ [cm]}. \tag{3.4}$$

3.2.5 Evaluation

3.2.5.1 Evaluation of Atmospheric Correction

To evaluate the atmospheric correction techniques, we compared results with field spectra. We compared the field spectra of the black target and the ice surface with the average surface reflectance within the respective region of interests (ROIs) illustrated in Figure 3.3. Since we used the same information for the empirical line calibration, we further compared the average reflectance spectra from four melt pond buffers with the respective *in situ* spectra.

To find suitable melt pond buffers for comparison, we used the radiance data and computed the mean and standard deviation for each spectral band within each buffer. For each buffer we then normalized the average standard deviation with the average mean reflectance assuming that a small normalized average standard deviation refers to a small heterogeneity within the buffer, i.e., the buffer mean reflectance is a good candidate for comparison. Eventually, we chose the four buffers with the smallest normalized average standard deviations.

We resampled the field data to AisaEAGLE bands using the sensor's spectral response functions and extracted the mean surface reflectance from the corresponding ROIs to compute the RMSE according to (Pedregosa et al., 2011; scikit-learn developers, 2018a) as:

$$RMSE(y, \hat{y}) = \sqrt{\frac{1}{n}\sum_{i=0}^{n-1}(y_i - \hat{y}_i)^2} \tag{3.5}$$

where y_i is the *in situ* reflectance and $\hat{y}_i$ is the buffer mean reflectance at the i-th band and n is the number of bands. We computed the RMSE for all bands in the wavelength region where the respective sensors overlap and, due to the relevance for the depth retrieval, separately for the wavelength region between 670 nm and 750 nm.

3.2.5.2 Evaluation of Bathymetry Retrieval

To quantify the quality of the depth retrieval we computed Pearson's correlation coefficient (r) according to (The Scipy community, 2019c) as (Equation (3.6)):

$$r(x,y) = \frac{\sum_{i=0}^{n-1}(x_i - \acute{x})(y_i - \acute{y})}{\sqrt{\sum_{i=0}^{n-1}(x_i - \acute{x})^2 \sum_{i=0}^{n-1}(y_i - \acute{y})^2}} \tag{3.6}$$

where x_i is measured depth at the i-th sample and y_i is the mean simulated depths inside the i-th buffer area; $\acute{x}$ is the average measured depth and $\acute{y}$ is the average buffer mean and n is the number of samples.

We further computed the RMSE according to Equation (3.4) with y_i being the measured depth and $\hat{y}_i$ being the mean predicted value of the buffer of the i-th sample and n being the number of samples. As a third measure we computed the coefficient of determination (R^2) according to (Kvålseth, 1985) (Equation (3.7)):

$$R^2(y,\hat{y}) = 1 - \frac{\sum_{i=0}^{n-1}(y_i - \hat{y}_i)^2}{\sum_{i=0}^{n-1}(y_i - \acute{y}_i)^2}, \tag{3.7}$$

where (Equation (3.8))

$$\acute{y} = \frac{1}{n}\sum_{i=0}^{n-1} y_i \tag{3.8}$$

Note that according to this definition R^2 may possibly be negative indicating a complete lack of fit.

3.3 Results

3.3.1 ATCOR-4

Figure 3.4 illustrates that ATCOR-4 generally overestimates reflectance but retrieved spectra roughly match the shape of the ground truth measurements. RMSEs are 0.12 and 0.1 for the bright and dark targets and corresponding wavelength region from 400 nm to 973 nm, and between 0.08 and 0.11 for the pond spectra and corresponding wavelength region ranging between 400 nm and 823 nm. Melt pond spectra are spiky in the blue-green wavelength region and the bright ice surface spectrum shows spikes and peaks over the entire spectrum. Melt pond and ice spectra are characterized by a strong increase in reflectance

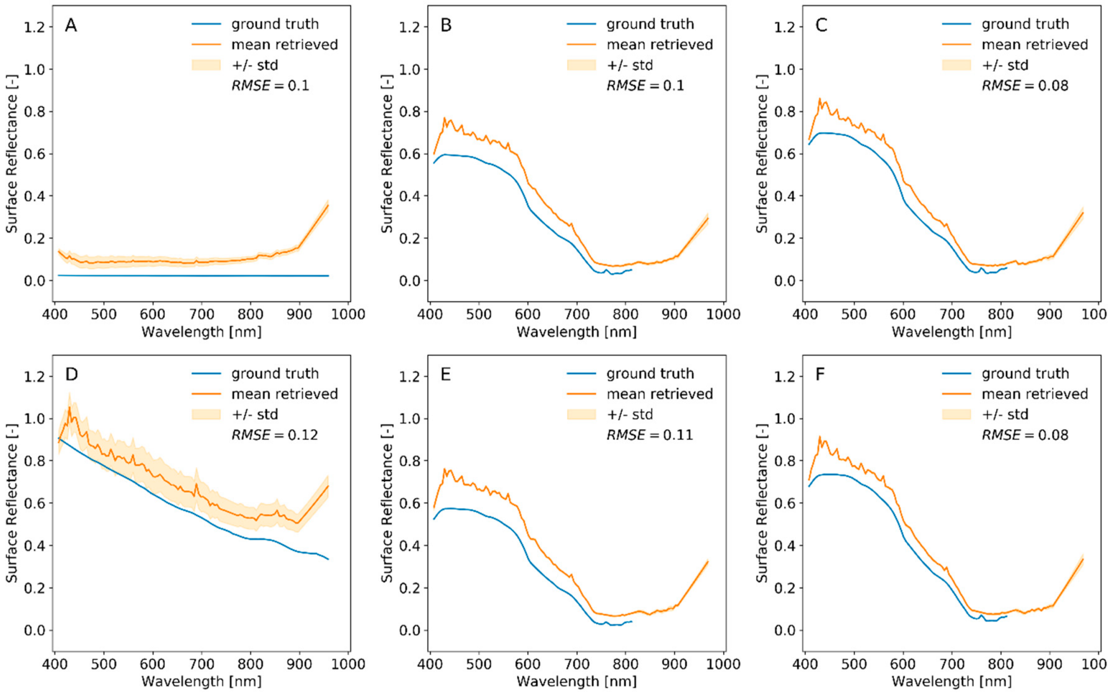

Figure 3.4: Comparison between Atmospheric and Topographic Correction (ATCOR) and field spectra for the dark (A) and bright (D) targets and four melt pond buffers (B,C,E,F). Root mean squared error (RMSE) is computed for the overlapping wavelength regions.

between 400 nm and 430 nm, while the dark target spectrum is characterized by decreasing reflectance between 400 nm and 450 nm. All spectra show a distinct increase in the wavelength region above ∼ 900 nm (note that the linear behavior results from interpolation in the 940 nm water vapor region). The large standard deviation of the dark and bright target indicates that both targets are characterized by a relatively high spectral variability, while the pond spectra inside the buffer areas are less variable.

In the wavelength region between 670 nm and 750 nm, RMSE for the dark and bright spectra are 0.07 and 0.1, respectively. The RMSE for the pond spectra is between 0.05 and 0.07. Figure 3.5 illustrates that a peak at ∼ 689 nm characterizes all spectra.

Measured and modeled depth values are highly correlated (r = 0.85) but modeled depths remain underestimated (Figure 3.6). This finds expression in the line of best fit's negative offset (–8.25) and results in a negative R^2 (–2.24) and high RMSE (11.57 cm). The slope of 0.83 indicates an increasing underestimation towards larger depths.

3.3.2 Empirical Line Calibration

Figure 3.7 illustrates that the empirical line calibration increases the accuracy of the retrieved spectra. Figure 3.7A and D show that the mean radiance spectra perfectly fit with the field spectra (RMSE = 0.0). In comparison to the field spectra, retrieved pond spectra overestimate reflectances in the wavelength region between 400 nm and ∼ 700 nm,

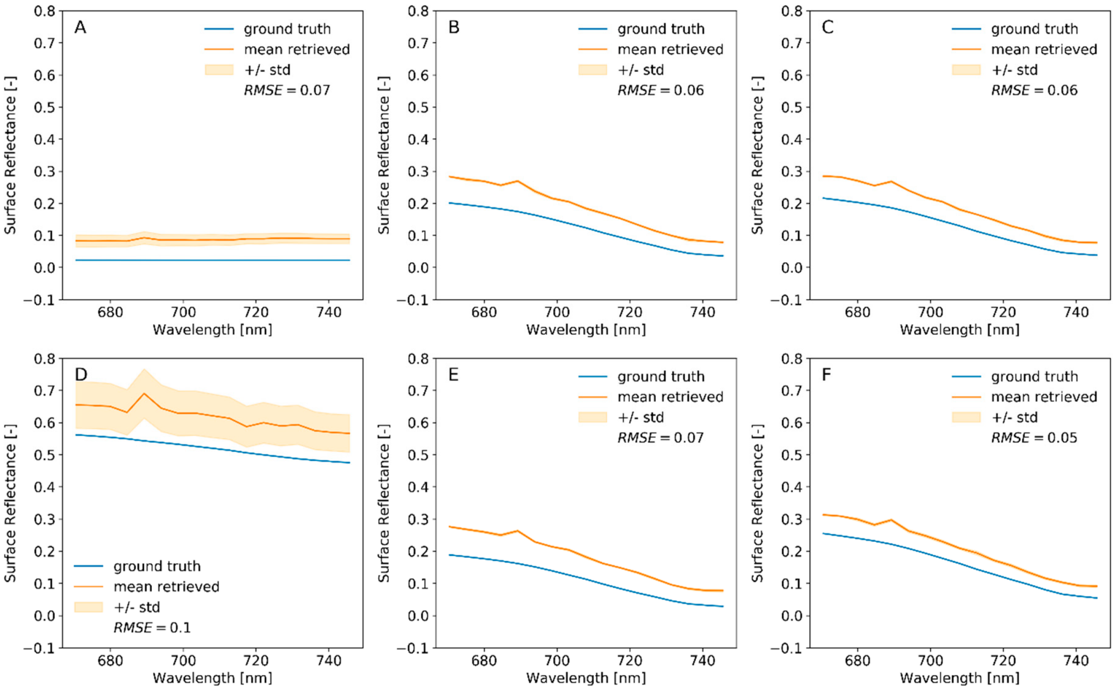

Figure 3.5: Comparison between ATCOR and field spectra for the dark (A) and bright (D) targets and the four melt pond buffers (B,C,E,F). RMSE is computed for bands between 670 and 750 nm.

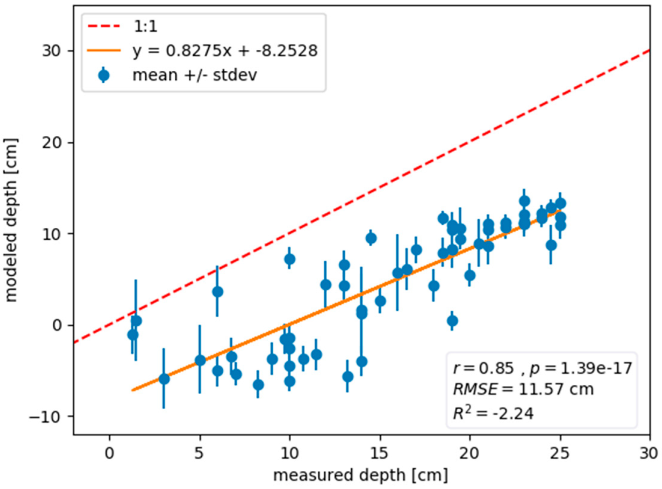

Figure 3.6: Scatter plot of measured vs. modeled pond depth ($n = 60$).

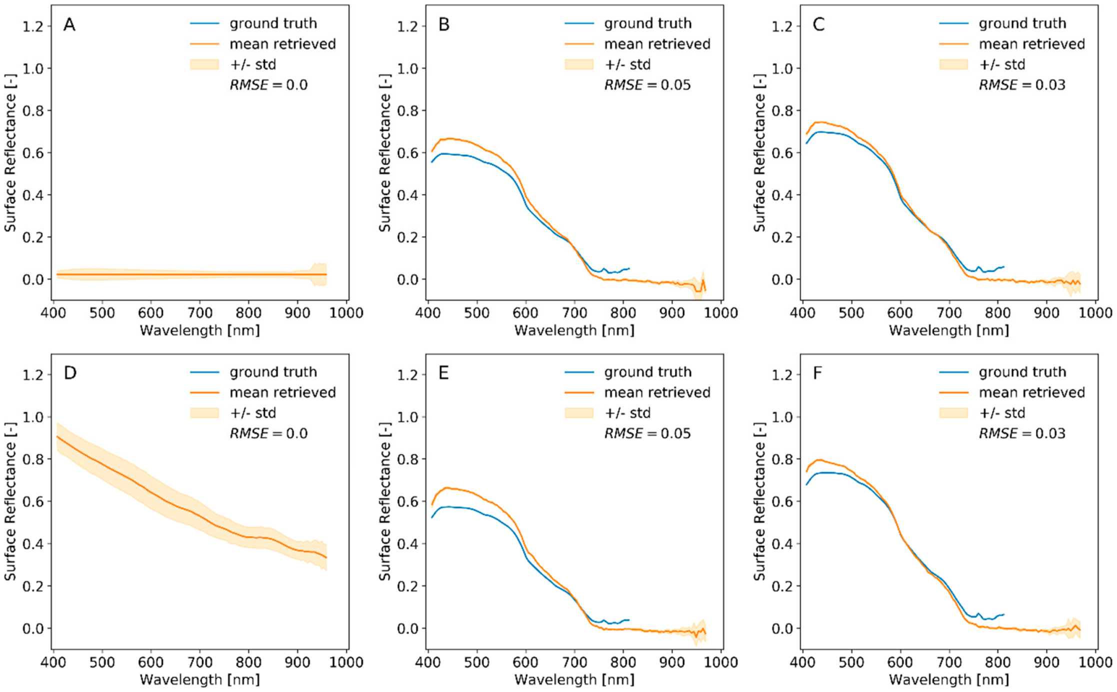

Figure 3.7: Comparison between empirical line calibration and field spectra for the dark (A) and bright (D) targets and four melt pond buffers (B,C,E,F). RMSE is computed for the overlapping wavelength regions, respectively.

whereby overestimation decreases towards longer wavelengths. At wavelengths beyond 700 nm, the empirical line method results in an underestimation, with values dropping below zero reflectance and an increasing standard deviation beyond 950 nm.

Figure 3.8 illustrates that the empirical line calibration results in a perfect fit of the retrieved spectra with field spectra of both targets (RMSE = 0.0). RMSE for the pond spectra is small (0.01–0.02) indicating a good fit. The slope of the curves, however, slightly differs. Generally, the slope of the retrieved curve is slightly steeper than the slope of the field measurements.

Due to the good performance of the empirical line calibration, the pond depth retrieval shows higher accuracies compared to the ATCOR-4 results. We excluded pixels with depths ≤ 0 from the analysis to avoid an influence of adjacent ice pixels incorporated in the buffered areas on the statistics. Measured and modeled depths are highly correlated ($r = 0.86$) with an RMSE of 5.96 cm. The model explains about half of the variability in pond depth ($R^2 = 0.49$). The slope of the line of best fit is close to 1 but the offset of 2.77 indicates a general overestimation of retrieved pond depths (Figure 3.9).

Correcting the offset (Figure 3.10) improves RMSE (4.05 cm) and R^2 (0.74). Pond 1 in Figure 3.11 demonstrates that the model is insensitive to pond bottom color since the bright and dark areas do not correspond to the derived bathymetry.

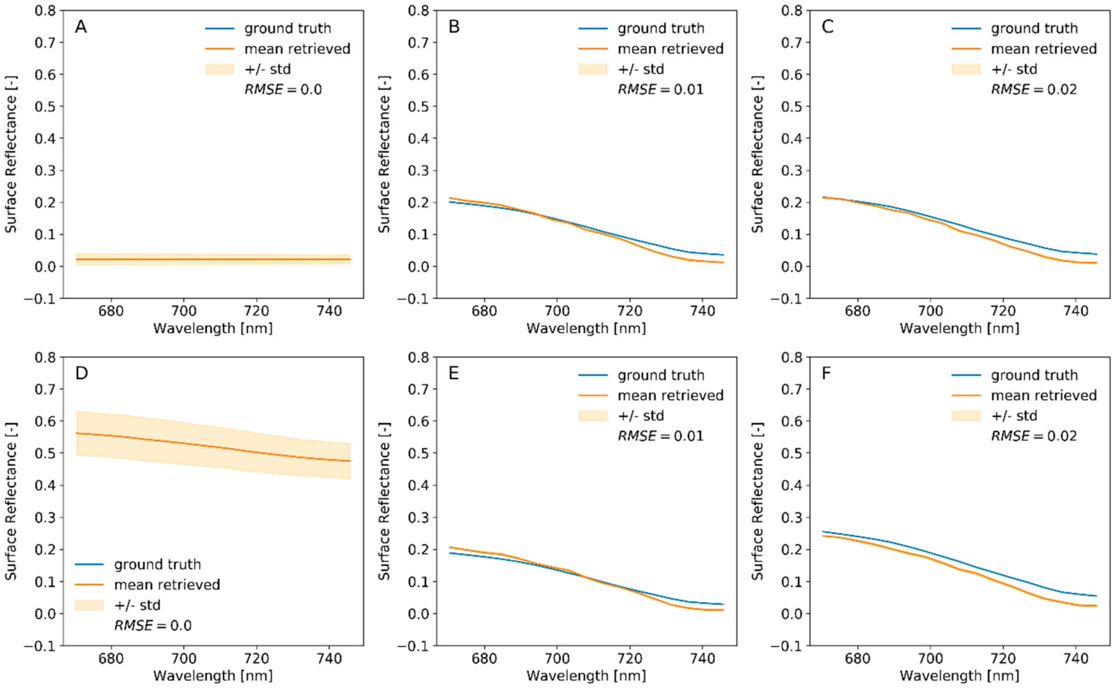

Figure 3.8: Comparison between empirical line calibration and field spectra for the dark (A) and bright (D) targets and four melt pond buffers (B,C,E,F). RMSE is computed for bands between 670 nm and 750 nm.

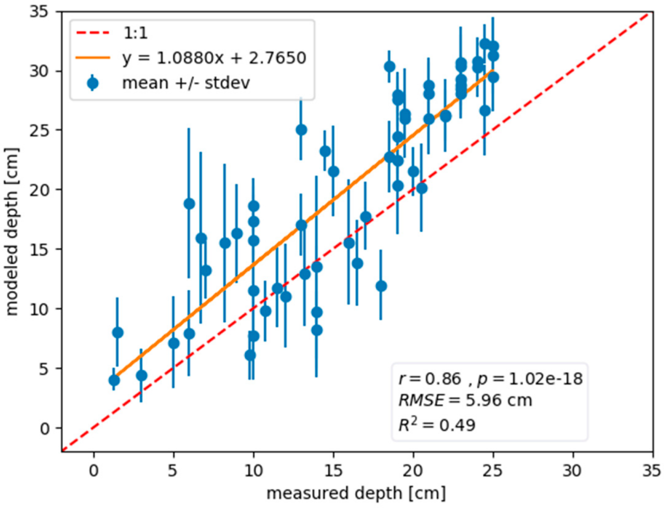

Figure 3.9: Scatter plot of measured vs. modeled pond depth ($n = 60$).

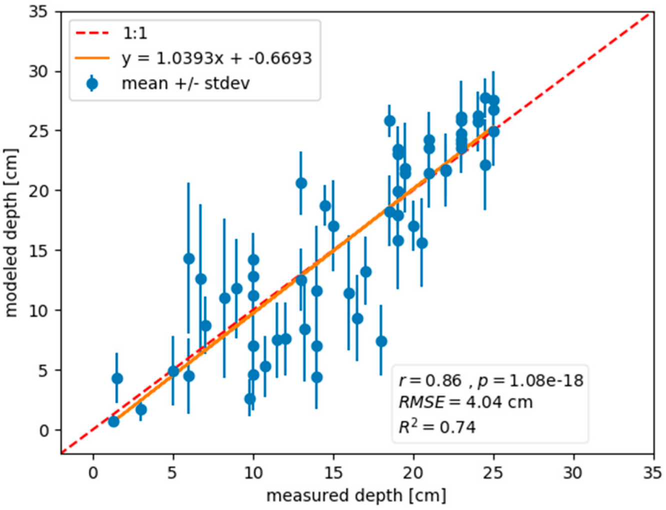

Figure 3.10: Scatter plot of measured vs. modeled pond depth ($n = 60$) after offset correction.

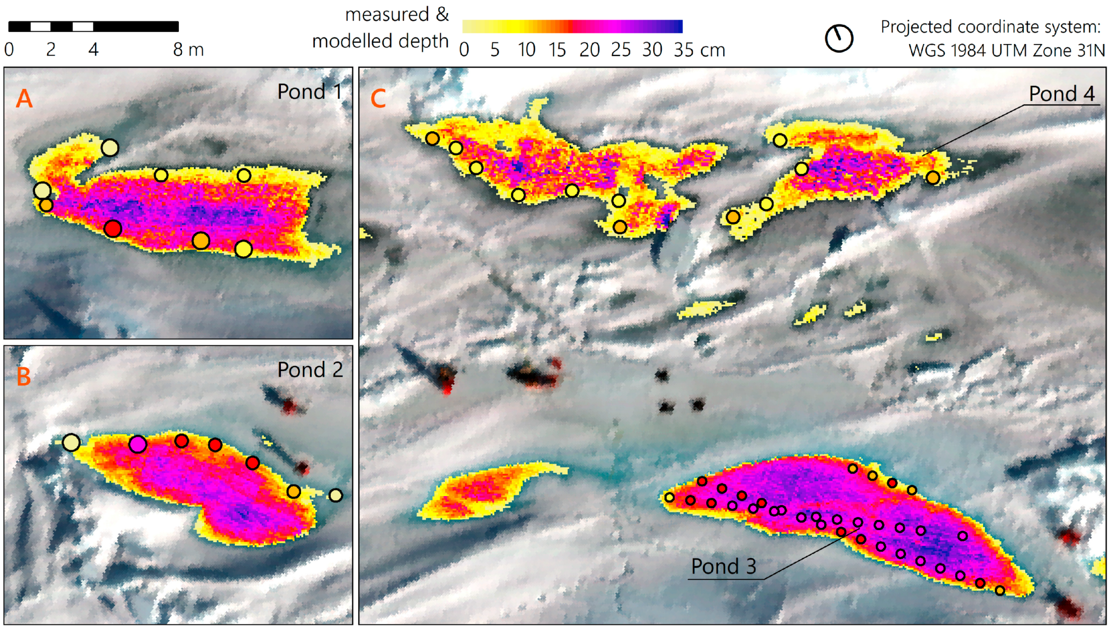

Figure 3.11: Results of pond depth model applied to empirical line correction results. Modeled and measured depth share the same color code. Circle sizes correspond to estimated spatial uncertainties (radii are 20 cm, 30 cm and 40 cm). (A) Pond 1. (B) Pond 2. (C) Ponds 3 and 4. Background: AisaEAGLE flight stripe (spatial resolution: 8.5 cm, RGB: 661.16 nm, 550.25 nm, and 482.57 nm).

3.4 Discussion

To the best of our knowledge, this study presents a first analysis of airborne hyperspectral image processing and analysis of Arctic sea ice. The setup consisting of spectral targets, field and atmospheric measurements is typical for airborne hyperspectral campaigns.

3.4.1 ATCOR-4

Most studies lacking atmospheric measurements use standard atmospheric profiles and aerosol models based on a qualitative assessment of environmental conditions. The MODTRAN 5 LUTs integrated in ATCOR-4 cover a wide range of environmental conditions but have not yet been tested in the Arctic sea ice environment.

ATCOR-4 performs a basic scene classification to compute a haze/cloud/water map with 19 classes and applies thresholds to certain bands to compute water and cloud masks (Richter and Schläpfer, 2015). Even though we raised the thresholds for clouds and water to their respective maxima, they were inappropriate for the sea ice environment, e.g., the reflectance of snow, ice and even melt ponds can reach values beyond 80 % in the Blue/Green. Consequently, the resulting image classification is inappropriate; 52.3 % were misclassified as clouds, 34.2 % were misclassified as land and only 13.5 % were classified as water while snow was overlooked, most probably due to the absence of a 1.6 µm channel. An inspection of the WV map shows that retrieved values range between 1.2 and 1.5 cm over water pixels and between 0.75 and 0.9 for the rest. Both values, however, do not correspond well with the sun photometer measurements (1.1415 (± 0.0226) cm).

The low flight altitude impeded the image-based retrieval of an aerosol type. Due to the location of the study area in the Arctic Ocean, however, we chose a maritime aerosol model. The variable visibility option was unavailable because the image did not contain a sufficient number of dark pixels. ATCOR-4 uses the dense dark vegetation approach to find the most suitable visibility for an image. Given the absence of vegetation in the Arctic sea ice, this method proved unsuitable. Nevertheless, retrieval of the visibility was possible resulting in a value of 100 km. The corresponding AOT ($\sim$ 0.2), however, is ten times overestimated compared to the sun photometer measurements ($\sim$ 0.02). Yet, even the maximum visibility of 120 km would result in an enormous overestimation of AOT, indicating that the chosen LUTs do not perform well in the Arctic. At the same time, flight altitude and corresponding atmospheric thickness is overestimated due to the limitation to 0.1 km minimum altitude. These issues may account for the spikes and peaks in the ATCOR-4 results (Figure 3.4).

Sensor calibration may also influence the results. The sensor was calibrated with the helicopter's acrylic window installed. Temperature differences between calibration, storage and operation may have caused slight defects or staining of the window, which may explain some of the noise visible in Figure 3.11. Another cause may be spectral smile effects or uncertainty in the applied solar irradiance spectrum, especially in the 380–600 nm spectral region as described by Thompson et al. (2015).

ATCOR reflectance spectra show a strong increase in the wavelength region > 900 nm. This increase is also visible in the radiance data and may result from second order light contribution from the blue end of the spectrum as observed for the CASI sensor in Antarctica by Black et al. (2014).

3.4.2 Empirical Line Calibration

As expected, results of the empirical line calibration accurately match field spectra indicated by the small RMSEs (< 0.05). Compared to the spectra retrieved with ATCOR-4, the spectra with the empirical line calibration are smoother, indicating that atmospheric conditions were stable during acquisition.

Although flight altitude was $\sim$ 200 ft on average, it varied between 157 ft and 263 ft over the course of the flight. The corresponding change in atmospheric thickness has likely influenced the empirical line calibration. Over the ROIs and pond measurements used for the quality assessment, altitude varied only between 229 ft and 243 ft. The small RMSEs indicate only marginal influence but in other parts of the flight stripe where flight altitude differed considerably, influence may be larger.

The overestimation in the blue-green wavelength region (Figure 3.7) may result from skyglint at the water surface or from the temporal difference between field and airborne measurements. We used spectral targets for the empirical line calibration. However, illumination conditions and viewing angle between ground truth spectroscopy and remote sensing data acquisition differed and we did not consider the targets' bidirectional reflectance distribution function (BRDF). For future studies, particular attention is, therefore, required for measurements simultaneously to the image acquisition and/or to the use of targets with known BRDF. In addition, the utilization of additional white and grey targets as proposed in Black et al. (2014) may improve atmospheric correction of airborne sensors in the future. The size of the targets depends on the sensor's FOV, flight altitude, and desired spatial resolution of the imagery and should be increased accordingly.

The empirical line calibration requires field information and, therefore, is logistically more challenging than LUT-based approaches. The identification of pseudo-invariant features in the Antarctic to facilitate empirical line calibration is recommended by Black et al. (2014). However, in the constantly changing central Arctic Ocean, such surfaces generally do not exist.

3.4.3 Pond Depth Retrieval

Results illustrate that the accurate retrieval of pond depth from airborne hyperspectral imagery depends on the quality of the atmospheric correction and the accurate retrieval of surface reflectance. Even though ATCOR-4 overestimated surface reflectance and partially resulted in spikes and peaks, the quality obtained may be sufficient for robust applications such as the computation of spectral indices. For applications that rely on precise spectral information, however, the results are inadequate.

The empirical line calibration reduced the differences in reflectance in the wavelength region around 710 nm, but the difference in slope resulted in an overestimation of pond depths. Correcting for the offset of ~ 4.5 cm improved RMSE and R^2 and performance is similar to the values presented in König and Oppelt (2020) ($r = 0.89$; R^2=0.74; RMSE= 2.81 cm).

Figure 3.12 exemplifies that the model produces accurate results. The pond mask accurately extracts the two small ice islands and the L-shaped draw around the bright, elevated ice is also described by the model. Figure 3.12 further indicates that the model is possibly sensitive to shadows. Pond depth appears to be overestimated in the shadow of the ice block on the right side of Figure 3.12B.

Results for Pond 1 (Figure 3.11A) illustrate that spectral information in the VIS is unsuitable for the derivation of pond depths. Bathymetry patterns in Figure 3.11 do not correspond to bottom color in Figure 3.1 suggesting the applicability of the model in dark and bright ponds.

Frequent cloud cover in the Arctic Ocean hampers observations with optical satellite sensors but UAVs and helicopters may operate below clouds. In its current state, the model presented in König and Oppelt (2020), however, is only valid for clear sky conditions. More research and development is necessary to enable pond depth retrieval using airborne hyperspectral data acquired under overcast conditions.

As discussed previously in König and Oppelt (2020), more *in situ* data covering a greater variety of pond characteristics is necessary to further test the model's applicability. The results presented in this study extend the model's testing and indicate its applicability in shallow ponds but tests in deep ponds on multi-year ice are still pending. However, field data of increased spatial resolution is desirable in order to investigate the spatial variability of pond depths. This may be achieved by means of remotely operated sonar equipped boats (e.g., Legleiter et al., 2014; Tedesco and Steiner, 2011). Yet, the shallowness of melt ponds on sea ice, especially at melt onset, might be an issue for most sonars.

3.4.4 Spatial Uncertainties

Given the high spatial resolution of 8.5 cm and considering the highly variable pond bottom bathymetry, the precise localization of field measurements is important for the validation process. At this scale, however, GPS measurements were insufficiently accurate to localize measurements within the ponds. For our study, we benefit from the large amount of field photographs and detailed protocols that permitted us to reconstruct measurement locations accurately. However, precision of the localization remains indefinable and its influence on the evaluation remains uncertain.

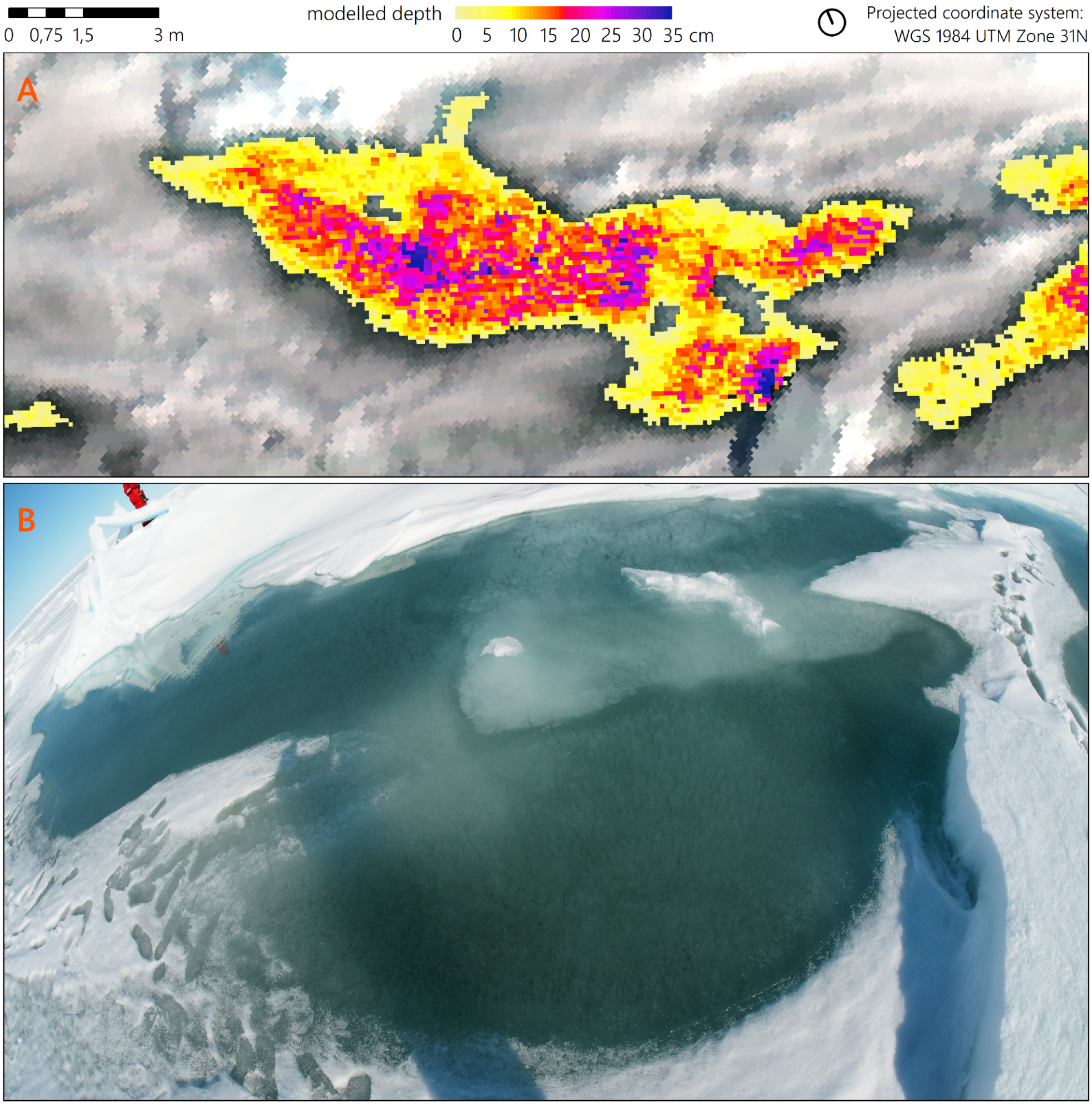

Figure 3.12: Comparison of bathymetry and field photograph. (A) Results of pond depth model applied to Empirical Line Correction results. Background: AisaEAGLE flight stripe (spatial resolution: 8.5 cm, RGB: 661.16 nm, 550.25 nm, and 482.57 nm). (B) Photo: Peter Gege.

We addressed the vague measurement localization by buffering the points with three different radii according to the estimated spatial uncertainty and, therefore, computed the mean of all pixels whose center is located within the buffer area. However, each mean is influenced by the frequency and range of values within a buffer, which is in turn influenced by the buffer's center location and radius, and the respective heterogeneity of the pond bottom included in the buffer. The standard deviation plotted in Figure 3.10 illustrates that the variability in pond depth within a buffer may be large, reaching a maximum range of 19.31 cm. Choosing the buffers' mean values for the computation of the performance metrics influences the results, e.g., choosing the pixel value from each buffer that fits the *in situ* measurements best would result in very high performance (r = 0.99; p = 0.00; RMSE = 0.96 cm; $R^2 = 0.98$).

In order to reduce the influence of spatial uncertainties on the interpretation, an improved localization of field measurements is therefore desirable for future studies. One option may be the establishment of a local reference system based on other techniques such as ultra-wideband positioning (Pozyx NV, 2020; Ammari, 2019).

We used the IMU/GPS data recorded during image acquisition for the geometric preprocessing of the AisaEAGLE imagery. While the progressive scanner is moving, the ice is drifting independently at the same time. We did not correct for these effects in the geometric preprocessing but comparisons with photographs taken at nadir from helicopter indicate that geometric effects due to ice drift are negligible in this case. Nevertheless, the influence of sea ice drift on progressive scanner image geometries may be worth investigating in future studies but requires accurate information about sea ice kinematics.

3.5 Conclusion

In this paper, we presented a novel study dealing with the acquisition, processing and atmospheric correction of airborne hyperspectral imagery in Arctic sea ice. We tested two atmospheric correction approaches (ATCOR-4 and empirical line calibration) on hyperspectral AisaEAGLE imagery acquired during RV *Polarstern* cruise PS106 in summer 2017 and validated results with field measurements. Based on this data, we tested if an existing model for pond depth assessment based on hyperspectral data described in König and Oppelt (2020) can be applied to airborne AisaEAGLE imagery.

We found that ATCOR-4 generally overestimates measured reflectances but retrieved spectra roughly match the shape of field measurements enabling robust applications such as computation of spectral indices. Retrieved spectra, however, are noisy and resulted in strongly underestimated pond depths. Given a maximum pond depth of about 100 cm, resulting accuracies were too low for pond depth assessment ($R^2 = -2.24$, RMSE = 11.57 cm). Therefore, we advise not using ATCOR-4 for pond depth retrieval at very low flight altitudes (< 100 m). Empirical line calibration was more accurate and resulted in smooth spectra and reduced differences between retrieved and *in situ* reflectance, especially in the wavelength region around 710 nm, which is relevant for the pond depth retrieval. Final results were highly correlated (r = 0.86), accurate (RMSE = 4.04 cm) and the model explained a large portion of the variability in pond depth (R^2= 0.74).

Although the ponds studied here cover a wide range of bottom type characteristics, more data from different sea ice regimes are desirable to further investigate the model's applicability. Maximum pond depth in this study was $\sim$ 35 cm. While the model is valid for pond depths up to 100 cm, tests in deep ponds as found on multi-year ice are still pending. We are confident that the Multidisciplinary drifting Observatory for the Study of Arctic Climate (MOSAiC) (Knust et al., 2019) will increase the amount and variability of ground truth data collected in conjunction with hyperspectral remote sensing data.

Our results are in good agreement with the findings of König and Oppelt (2020) and show the potential of melt pond bathymetry assessment by means of airborne hyperspectral remote sensing. Results, however, likewise indicate that the model is sensitive to differences in spectral slope. An application of the model for observations of the temporal evolution of melt pond depth, therefore, requires accurate radiometric and spectral calibration of the sensor as well as a precise atmospheric correction.

For future campaigns in Arctic sea ice, we recommend that the instrument should be calibrated under comparable environmental conditions. We further recommend upgrading the setup with a FODIS to track changes in downwelling irradiance and deploying of spectral reference targets for calibration and validation.

The technical development in the field of hyperspectral imaging sensors resulted in small-sized lightweight sensors that may be operated on UAVs (Adão et al., 2017); and hyperspectral satellite missions such as EnMAP (Guanter et al., 2016) may enable pond depth retrieval on new spatial and temporal scales. Operationalization of the method and scaling to satellite measurements, however, requires an atmospheric correction, where field information is not available. Therefore, we underline the need for improved atmospheric correction processors that consider environmental and atmospheric conditions in the Arctic Ocean. Furthermore, we hypothesize that the implementation of LUTs specifically designed for the Arctic sea ice environment may improve existing algorithms for atmospheric correction.

Besides an appropriate atmospheric correction, applicability of the pond depth retrieval in satellite remote sensing is limited to ponds of certain area and geometry depending on a sensor's spatial resolution. The model is only valid for clear melt pond pixels and spectral mixing with adjacent sea ice surfaces may result in erroneous bathymetry. Further research is necessary to investigate how these issues may be addressed, e.g., by identification and exclusion of mixed pixels or spectral unmixing.

Acknowledgements

We acknowledge the support of captain Wunderlich, the crew and the chief scientists Andreas Macke and Hauke Flores of RV *Polarstern* cruise AWI_PS106_00. We thank all colleagues from PS106 who assisted with fieldwork and in particular Niels Fuchs, Peter Gege, Martin Hieronymi and Thomas Ruhtz for their valuable contributions to the *in situ* measurements, and the pilots Lars Vaupel and Jan Kenzia for the helicopter operation. We further thank Peter Gege for his advice and Marcel Nicolaus for his opinion on the pond site's ice type situation. We would also like to thank Birgit Heim for access to ATCOR-4, and Sebastian Rößler and Rolf Richter for their helpful answers related to AisaEAGLE processing and ATCOR. We acknowledge the efforts of the AERONET-MAN and the colleagues from TROPOS for the sun photometer measurements. Finally, we would like to thank three anonymous reviewers for their valuable comments.

Chapter 4

Application of Sentinel-2 MSI in Arctic Research: Evaluating the Performance of Atmospheric Correction Approaches Over Arctic Sea Ice

M. König, M. Hieronymi and N. Oppelt

frontiers in Earth Science (2019), doi:10.3389/feart.2019.00022
Received: 27 July 2018 - Accepted: 04 February 2019 - Published: 22 February 2019

Abstract. Multispectral remote sensing may be a powerful tool for areal retrieval of biogeophysical parameters in the Arctic sea ice. The MultiSpectral Instrument on board the Sentinel-2 (S-2) satellites of the European Space Agency offers new possibilities for Arctic research; S-2A and S-2B provide 13 spectral bands between 443 and 2,202 nm and spatial resolutions between 10 and 60 m, which may enable the monitoring of large areas of Arctic sea ice. For an accurate retrieval of parameters such as surface albedo, the elimination of atmospheric influences in the data is essential. We therefore provide an evaluation of five currently available atmospheric correction processors for S-2 (ACOLITE, ATCOR, iCOR, Polymer, and Sen2Cor). We evaluate the results of the different processors using *in situ* spectral measurements of ice and snow and open water gathered north of Svalbard during RV *Polarstern* cruise PS106.1 in summer 2017. We used spectral shapes to assess performance for ice and snow surfaces. For open water, we additionally evaluated intensities. ACOLITE, ATCOR, and iCOR performed well over sea ice and Polymer generated the best results over open water. ATCOR, iCOR and Sen2Cor failed in the image-based retrieval of atmospheric parameters (aerosol optical thickness, water vapor). ACOLITE estimated AOT within the uncertainty range of AERONET measurements. Parameterization based on external data, therefore, was necessary to obtain reliable results. To illustrate consequences of processor selection on secondary products we computed average surface reflectance of six bands and normalized difference melt index (NDMI) on an image

subset. Medians of average reflectance and NDMI range from 0.80–0.97 to 0.12–0.18 while medians for TOA are 0.75 and 0.06, respectively..

4.1 Introduction

The limited accessibility of Arctic sea ice makes satellite remote sensing an important tool for synoptic observations in this region. The retrieval of parameters, such as the spectral albedo of sea ice or snow and properties of melt ponds and leads, relies on spectral information; the retrieval of optical properties of target surfaces and waterbodies therefore is necessary. Optical sensors such as the Advanced Visible High Resolution Radiometer (AVHRR; e.g., Huck et al., 2007) and the Moderate Resolution Imaging Spectroradiometer (MODIS; e.g., Rösel et al., 2012; Tschudi et al., 2008) have long been used in Arctic research (Pope et al., 2014; Nasonova et al., 2017) providing observations of different parameters such as sea ice extent, sea ice thickness and albedo. The Sentinel-3 satellites (S-3) from the European Space Agency's (ESA) Copernicus program, carrying the Ocean and Land Colour Instrument (OLCI), continue this tradition (Donlon et al., 2012; Malenovský et al., 2012). Recently, Istomina and Heygster (2017) published a retrieval algorithm for sea ice albedo and melt pond fraction from S-3/OLCI observations. Despite a high temporal and spatial coverage of the abovementioned sensors (swath widths: AVHRR = 2,900 km, MODIS = 2,330 km, S-3/OLCI = 1,270 km), their coarse spatial resolution (AVHRR: 1.1–4 km, MODIS: 250–1,000 m, S-3/OLCI: 300 m) impedes detailed observations of sea ice features such as melt ponds and ridges, which exist at spatial scales of meters to tens of meters (Figure 4.1). Studies based on optical sensors with a higher spatial resolution ($\leq$ 30 m), however, are rare. Markus et al. (2002) demonstrated the potential of Landsat 7 ETM+ (L7; 30 m) for the classification of summertime sea ice surface conditions and retrieved the spatial distribution of ponded/unponded ice and open water (Markus et al., 2003), while Landy et al. (2014) used this sensor to observe sea ice development. Rösel (2013) underlined that high resolution satellite data enable determining melting features on Arctic sea ice and provide a basis for the comparison with coarse resolution satellite data. The ETM+ 8-bit sensor, however, showed saturation problems in the contrast-rich Arctic environment (Bindschadler et al., 2008; Rösel, 2013).

ESA's Sentinel-2 mission (S-2) offers new opportunities for optical sensors in the Landsat-like spatial domain. S-2 consists of the twin satellites S-2A and S-2B, launched in 2015 and 2017, respectively. Both satellites are equipped with the MultiSpectral Instrument (MSI), which provides 13 spectral bands with a 12-bit radiometric resolution in the wavelength region from 443 to 2,202 nm. Depending on the band, spatial resolution varies between 10, 20, and 60 m (European Space Agency, 2015, 2018a). Figure 4.2 illustrates the spatial and spectral settings of S-2A. Compared to L7, S-2 has a larger swath width (290 km) and geographical coverage reaches up to 83° north. The two S-2 satellites are shifted by 180° on the same orbit, which results in a return period of 5 days. In higher

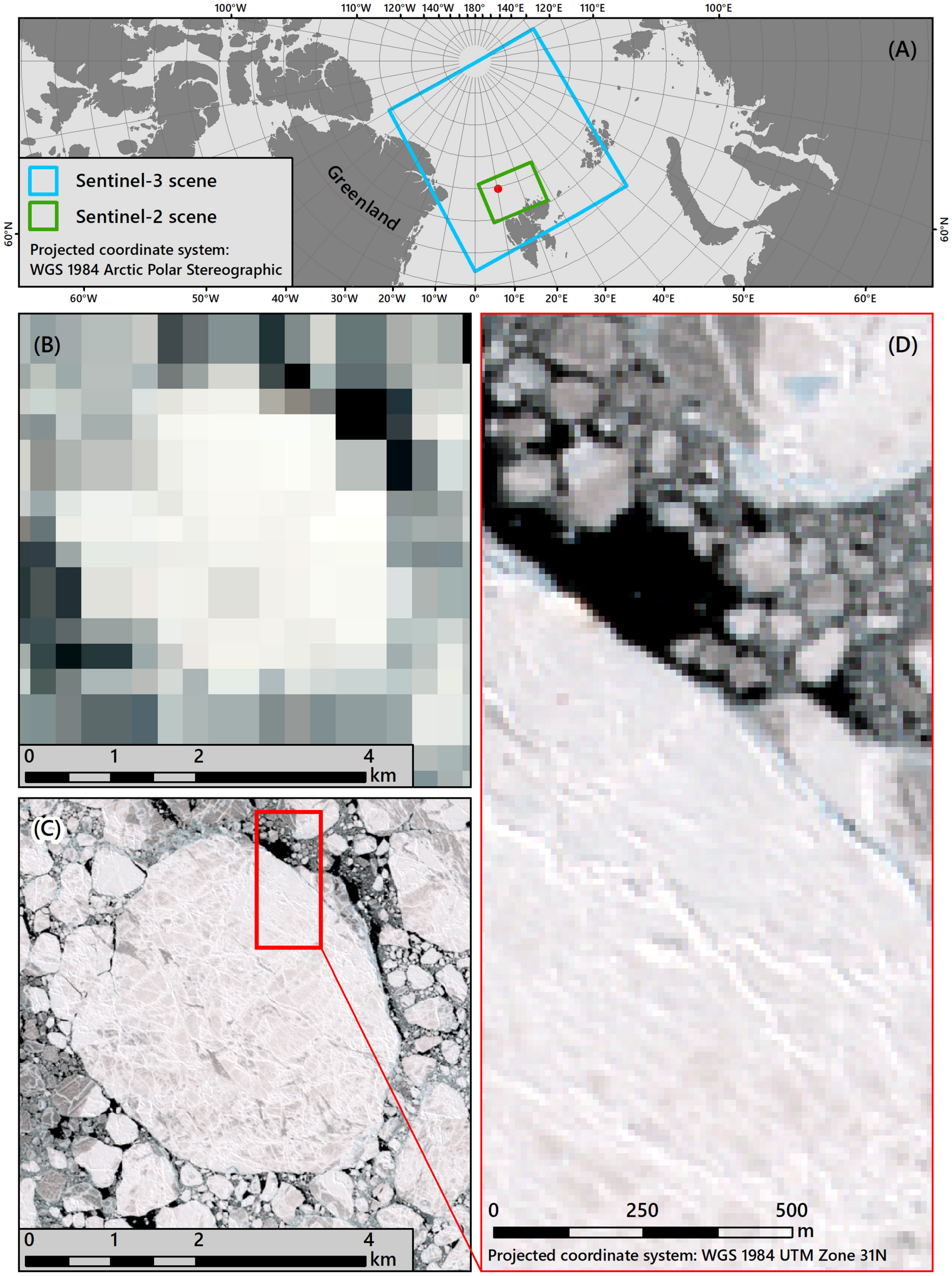

Figure 4.1: Comparison of Sentinel-2A (S-2A) and 3A (S-3A) spatial coverage and resolution [contains modified Copernicus Sentinel data (2017) processed by ESA/EOM]. (A) Coverage of S-3A/OLCI and S-2A/MSI scenes, the red dot indicates the location of (B). (B) Ice floe acquired with S-3A/OLCI (300 m, RGB: 665, 560, and 490 nm) at 2017-06-10 14:00:15 UTC. (C) The same floe acquired with S-2A (10 m, RGB: 665, 560, and 490 nm) at 2017-06-10 14:58:01 UTC. (D) S-2A details.

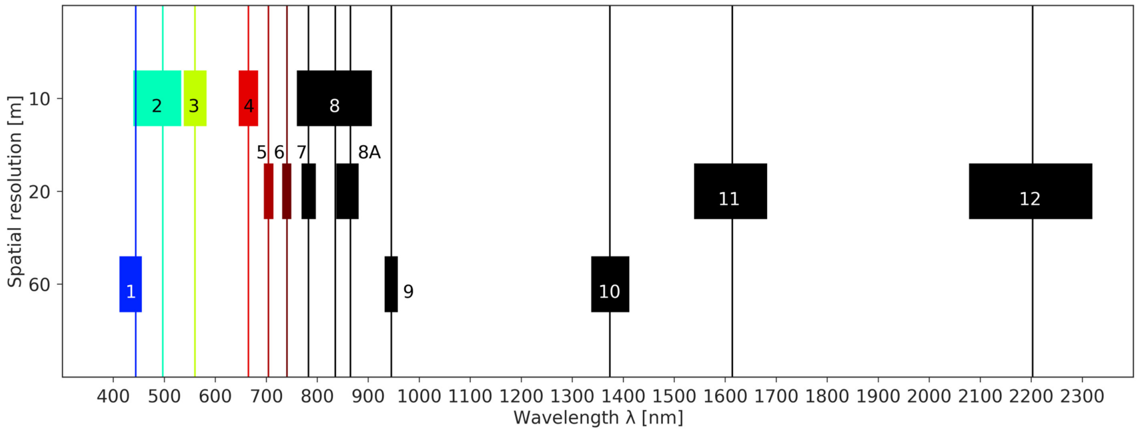

Figure 4.2: S-2A MSI band widths, central wavelengths and spatial resolutions.

latitudes, overlapping swaths further increase the return period to up to one image per day (European Space Agency, 2015, 2018b, Copernicus EO Support, personal communication). Due to the terrestrial focus of the S-2 mission, geographical coverage in the Arctic Ocean is currently limited to areas around islands but areas of interest may be added to the Mission baseline “if sufficient resources are identified” (European Space Agency, 2015). Malenovský et al. (2012) mentioned the potential of S-2 for albedo retrieval, derivation of snow properties and mapping of polynyas and leads; nevertheless, they also highlighted the demand for “precise corrections for atmospheric propagation, topography and directional reflectance behavior” (Malenovský et al., 2012), pointing to the importance of atmospheric correction (AC) of optical remote sensing data. Zege et al. (2015) also emphasized the importance of AC for the retrieval of melt pond fraction and surface albedo.

Radiative transfer through the atmosphere is strongly influenced by Rayleigh and Mie scattering as well as aerosol and gas absorption. This combination is particularly challenging over water areas, where the atmospheric path radiance is typically > 85 % of the total signal in oceanic waters, > 60 % in sediment-rich waters, and > 94 % in very dark waters (IOCCG, 2010). Low sun zenith angles ($> 70°$) and correspondingly long atmospheric paths further aggravate the processing of data at the beginning and the end of summer in high latitudes (IOCCG, 2015). An adequate AC is therefore essential for the derivation of physical surface properties and follow-up multi-temporal analyses. Another challenge resulting from atmospheric transfer and the scattering of radiation is the neighboring or adjacency effect, i.e., the scattering of light from neighboring surfaces into the sensors field of view resulting in information overlay (Sterckx et al., 2015b). Adjacency effects depend on the brightness contrast between a target pixel and its neighborhood (Richter et al., 2006). The Arctic sea ice is a mix of snow, ice, melt ponds and ocean water, with typical broadband albedos in the visible wavelength region (VIS) ranging from > 0.90 for fresh snow to < 0.05–0.1 for ocean water (Perovich et al., 1998). Moreover, while being negligible for wavelength regions > 1.5 µm, the adjacency effect increases with shorter wavelengths (Richter and Schläpfer, 2017), i.e., the wavelength region used for water remote sensing is heavily affected. Due to the characteristic spatial mixture and high contrasts of deep, clear ocean waters, melt ponds, bright ice and snow surfaces in the sea ice, we expect the adjacency effect to have a large impact on S-2 imagery of Arctic sea ice.

Several AC processors are available for S-2, and some papers already compared processors for lakes (e.g., Dörnhöfer and Oppelt, 2016; Martins et al., 2017). Only recently, Doxani et al. (2018) performed an inter-comparison of AC processors for different surface types in temperate and tropical zones. Yet, to our knowledge, no study exists for Arctic sea ice; therefore, the objective of this paper is to evaluate the performance of AC processors for S-2 over different surface types in the Arctic sea ice. For this, we processed S-2A data applying five AC processors (ACOLITE, ATCOR, iCOR, Polymer, and Sen2Cor) and evaluated the results using *in situ* data from open water and ice floe surface measurements acquired during an RV *Polarstern* cruise in June 2017. We further investigate the influence of different AC processors on the retrieval of apparent optical properties, i.e., surface reflectance and remote sensing reflectance, which are used to retrieve parameters such as the spectral albedo or NDMI.

4.2 Methods

4.2.1 Study Area

4.2.1.1 Cruise Overview

During cruise PS106.1 RV *Polarstern* was moored to an ice floe north of Svalbard between June 3 and 16, 2017 (Figure 4.3). At the beginning of the measurement period, snow and white ice covered most of the floe. Some few ponds had already formed at pressure ridges but we did not observe any pond formation on the flat parts of the floe; bare ice was exposed only very occasionally. Neither ponds nor bare ice were present near the measurement sites. Melting, however, started during the measurement period. The specific surface area of snow samples from the top 1–2 cm has been analyzed with an IceCube (A2 Photonic Sensors, France) at different locations in the area of interest. Snow melt results in a decrease of the snow's specific surface area. Figure 4.4 illustrates that melt occurred between June 4 and 10.

4.2.1.2 Atmospheric Parameters

To provide input data for the different AC processors, we used sun photometer measurements conducted on board of RV *Polarstern* and published in the Maritime Aerosol Network (AERONET-MAN, Holben et al., 1998). For later analysis, we computed the aerosol optical thickness (AOT) at 550 nm from the sun photometer measurements as:

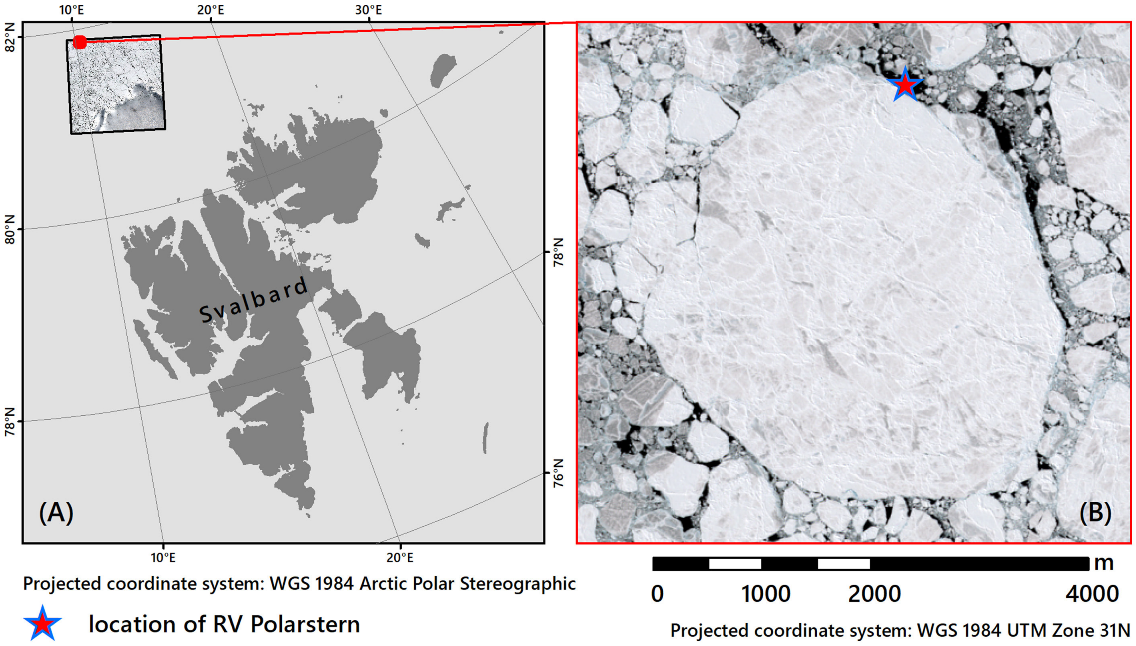

Figure 4.3: Location of S-2 granule (A) and ice floe (B) in the Arctic Ocean on June 10, 2017.

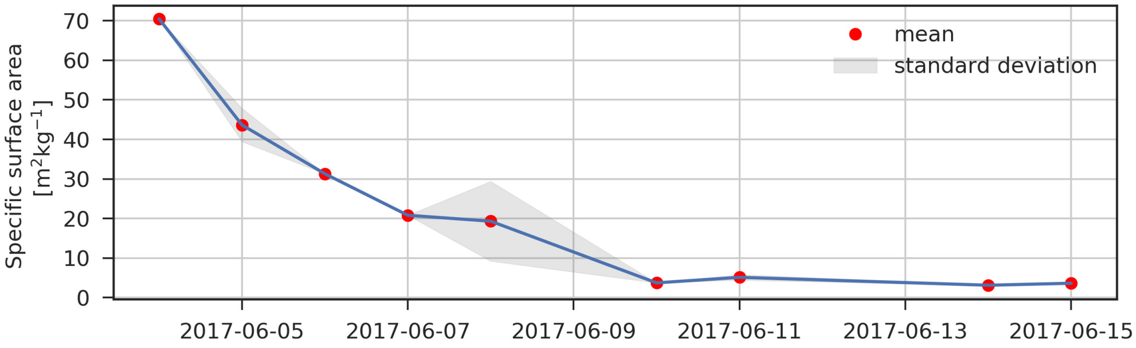

Figure 4.4: Specific surface area of snow at different locations between 2017-06-04 and 2017-06-15.

$$\beta = \frac{AOT_\lambda}{(\lambda/550)^{-\alpha}} \tag{4.1}$$

with β being turbidity, i.e., AOT at 550 nm, AOT_λ being the mean AOT at λ (500 nm) and α being the mean Angstrom exponent between 440 and 870 nm. We further used data from the weather station on board RV *Polarstern* (Schmithüsen, 2018). Table 4.1 summarizes minimum, maximum, mean and standard deviation of the atmospheric parameters used to atmospherically correct the S-2 data acquired on June 10, 2017 (details on S-2 data are provided in Section 7.2.3).

Table 4.1: Atmospheric parameters.

Parameter	**Unit**	**Minimum**	**Mean (± Standard Deviation)**	**Maximum**	**Data source**
Aerosol optical thickness at 550 nm	[-]	0.0217	0.0231 (± 0.0029)	0.0317	AERONET Microtops Level 2.0 data
Water vapor	cm	1.1066	1.1415 (± 0.0226)	1.1881	AERONET Microtops Level 2.0 data
Visibility	km	∼ 60	65.00 (± 2.2)	∼ 70	Weather station on board RV *Polarstern*

4.2.2 *In Situ* Data

To validate the results of the AC processors, we performed radiometric measurements of snow and ice covered areas (Section 7.2.2.1.1) as well as open water (Section 7.2.2.1.2). Simultaneously to the radiometric open water measurements, we took water samples for water constituent analysis (Section 7.2.2.2). All measurements have been localized with Global Positioning System (GPS) measurements (Section 7.2.2.3).

4.2.2.1 Radiometric Measurements

4.2.2.1.1 Snow and Ice Measurements on the Floe

For spectral measurements on the floe, we used an ASD LabSpec5000 spectrometer (Analytical Spectral Devices Inc., United States), covering the wavelength region from 350 to 2,500 nm with a 1 nm spectral sampling rate. The ASD was equipped with an optical fiber with a 23° field of view (FOV) mounted to a pistol grip attached to a pole to avoid influences of the polar suits during the measurements (Figure 4.5A). We used a Labsphere Spectralon reflectance standard with 95 % diffuse reflectance (Labsphere Inc., United States) as white reference. In addition, we used a set of Ocean Optics STS-VIS

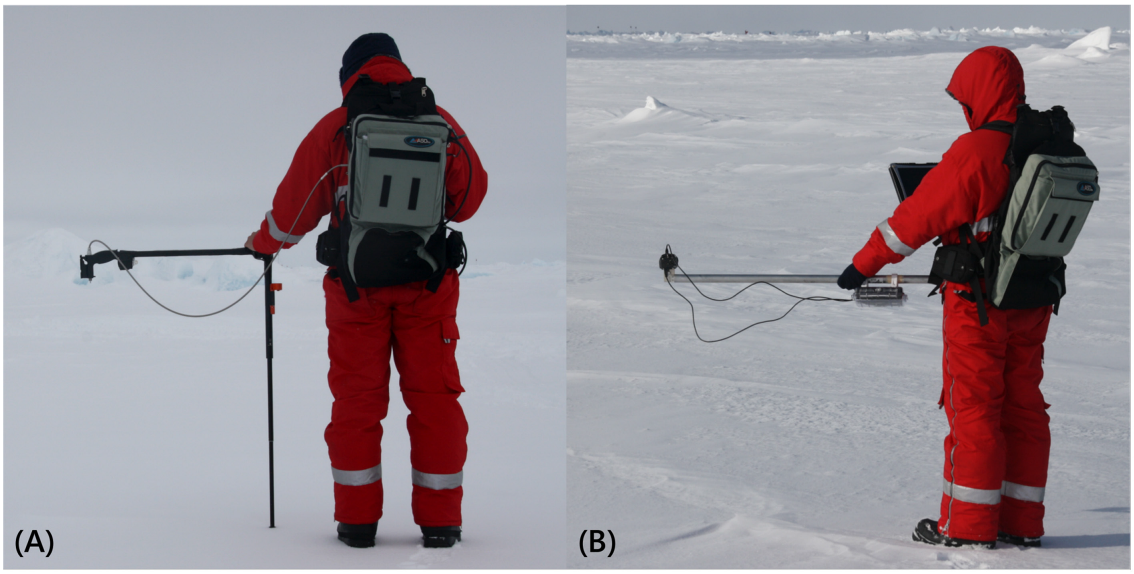

Figure 4.5: Measurement setups for ASD (A) and Ocean Optics (B) spectrometers. Photos: Natascha Oppelt.

spectrometers (Ocean Optics Inc., United States). The setup consists of two synchronized spectrometers; one pointing downwards with a 1° FOV and the other, equipped with a diffusor, pointing upwards to track planar incoming radiation. Both instruments cover a wavelength region from 340 to 820 nm with a spectral sampling rate < 1 nm. The spectrometers have also been attached to the end of a pole to avoid influences of the polar suits on the measurements (Figure 4.5B). For the Ocean Optics Instruments, we used a Labsphere Spectralon 99 % diffuse reflectance standard (Labsphere Inc., United States) as white reference. For both instrument setups, we took reference measurements at intervals < 10 min and when illumination conditions changed. Before conducting a white reference measurement with the ASD, we measured the Spectralon panel to control whether illumination has changed since the last reference measurement. If we detected changes, we performed a visual quality check on all measurements since the previous white reference and deleted spectra with unusual shapes. We corrected the Ocean Optics measurements for irradiance changes using the upwards pointing sensor. To account for the spatial heterogeneity within one S-2 pixel, we either walked around during the measurement process or performed measurements at different sites that we chose randomly. Table 4.2 summarizes measurement dates, instruments and illumination conditions.

4.2.2.1.2 Open-Water Measurements

In open-sea water of a polynya, we conducted radiometric measurements from the deck of the vessel using three hyperspectral (380–950 nm) RAMSES sensors (TriOS GmbH, Germany). The sensors were arranged to measure downwelling irradiance (E_d), upwelling radiance just above the water surface (L_u; sensor viewing angle of 40° with 90° azimuth

Table 4.2: Illumination conditions and instruments used.

Date	**Instrument(s) used**	**Illumination conditions**
2017-06-05	ASD	Diffuse, solar disk invisible
2017-06-07	ASD, OO	Variable
2017-06-09	OO	Diffuse, solar disk invisible
2017-06-10	RAMSES	Clear sky
2017-06-15	ASD, OO	Diffuse, solar disk visible

ASD, Analytical Spectral Devices spectrometer; OO, Ocean Optics spectrometer.

angle to the sun), and corresponding sky radiance (L_{sky}). We calculated remote sensing reflectance, R_{rs}, according to the following equation:

$$R_{rs}(40°, 90°) = \frac{L_u(40°, 90°) - \rho L_{sky}(40°, 90°)}{E_d} \tag{4.2}$$

The sea surface reflectance factor, ρ, depends on the sun-viewing geometry and wind-dependent roughness of the surface. Wind was light to moderate, but the limited fetch reduced roughness (mean square slope of the waves) compared to open sea. We applied the usually recommended surface reflactance factor of Mobley (1999) to determine the mean reflectance, in this case $\rho = 0.0272$. Moreover, we applied four different surface reflectance factors between 0.0176 and 0.03 (Mobley, 2015; Hieronymi, 2016) to account for potential effects of reduced roughness and polarization. This methodical variability together with temporal changes of the single measurements were taken into account to determine the standard deviation of the *in situ* measurements.

We resampled all field spectra to S-2A bands using the spectral response functions and central wavelengths (European Space Agency, 2018a,c).

4.2.2.2 Water Sampling

We took water samples from the polynya simultaneously to the radiometric measurements. Water samples were filtrated and optically analyzed in the ship's laboratory. We determined the spectral absorption properties using a PSICAM (Röttgers and Doerffer, 2007), a QFT-ICAM (Röttgers et al., 2016), and a Liquid Waveguide Capillary Cell (World Precision Instruments, United States). During the S-2A acquisition on June 10, the –1.7 °C cold seawater had a salinity of $\sim$ 34 PSU. The particle concentration was very low, yielding a total particulate absorption coefficient at 440 nm, $a_p(440)$ of approximately 0.013 m^{-1}. The colored dissolved organic matter (CDOM) absorption at 440 nm, $a_{cdom}(440)$, was 0.038 m^{-1}. The spectral shape of the particulate absorption indicates only to the presence of organic phytoplankton particles and no sediments; there is no significant particulate and CDOM absorption in the near infrared (> 700 nm). The chlorophyll-a concentration (Chl-a) from the photometric measurements was 0.19 ($\pm$ 0.1) mg m^{-3}; additional measurements with an AlgaeTorch (bbe Moldaenke GmbH, Germany) yielded Chl between 0.2 and 0.3 mg m^{-3}. These results confirm that the sampled water was very clear during the measurement period.

4.2.2.3 Positioning of Sampling Points

During the measurement period (Table 4.2) the ice floe drifted several tens of kilometers. To relocate all field measurements in a satellite image, we performed a drift-correction. Three stationary GPS devices constantly tracked floe movement in a 10-s interval. Additionally, we determined the locations of all sampling points with GPS measurements (F5521gw, Ericsson, Sweden; Galaxy S7, Samsung, South Korea; eTrex 10, Garmin, United States) in the World Geodetic System 1984 reference system. To locate all measurements from different dates and times in a single satellite image, we first applied a Savitzky-Golay filter to smooth the positioning data of each of the stationary GPS devices; then we used a second order polynomial to interpolate points in a 1-s interval. In this way, we could allocate every field measurement to three stationary GPS positions. Using this data, we computed the distances from every field measurement position to each of the three stationary GPS devices at the respective time of data acquisition ($t_{in\ situ}$). To find the measurement locations on the floe at the time of satellite overpass ($t_{satellite}$) we fit the distances to the three stationary GPS devices at $t_{satellite}$ to the distances computed at $t_{in\ situ}$ using the method of least squares. Finally, we performed a visual quality control.

4.2.3 Sentinel-2 Data

On June 10, 2017, clear sky conditions allowed acquisition of S-2A data of the floe at 14:58:01 UTC. For this study, we used the S-2 L1C top of atmosphere (TOA) reflectance product (processing baseline: 02.05 European Space Agency, 2015). For AC evaluation, we used S-2 bands which are in the spectral range of the field instruments, i.e., S-2A bands 2–7 (490–783 nm) for sea ice surfaces and bands 2–7 plus band 8A (490–865 nm) for the open water surface. All processors provide a 10 m output, except ATCOR. Which only offers a 20 m output. To provide spatially comparable results, we therefore downsampled 10 m output data to a spatial resolution of 20 m by 2 × 2 pixel block averaging.

4.2.3.1 Regions of Interest

In general, a point-by-pixel comparison is necessary for an accurate validation of remote sensing data via *in situ* measurements. With a steadily drifting floe, however, we are unable to assess precise accuracies of GPS measurements and trilateration; we therefore dismissed a point-based validation. Instead, we defined a region of interest (ROI) for each measurement section by computing a circular buffer with a 20 m radius around all

Table 4.3: Number of pixels, number of *in situ* spectra and measurement device.

ROI	**Date**	**No. of spectra**	**No. of pixels**	**Device**
05A	2017-06-05	411	12	ASD
05B	2017-06-05	686	15	ASD
05C	2017-06-05	346	16	ASD
07A	2017-06-07	177	18	ASD
07B	2017-06-07	400	32	OO
07C	2017-06-07	100	24	OO
09A	2017-06-09	150	20	OO
10A	2017-06-10	> 1,000	15	RAMSES
15A	2017-06-15	330	20	ASD
15B	2017-06-15	60	9	ASD
15C	2017-06-15	60	17	ASD
15D	2017-06-15	180	27	OO

OO, Ocean Optics; ASD, Analytical Spectral Devices spectrometer for each ROI (Figure 3 shows the locations of ROIs).

GPS points belonging to one measurement section. We defined all pixels intersecting the respective buffer area to be one ROI. Table 4.3 lists the respective number of pixels and field spectra as well as the measurement device used for each ROI.

Regarding the RAMSES measurements, we manually defined one ROI in the open water area next to RV *Polarstern* and excluded pixels with unusual shape presumably influenced by floating ice. Figure 4.6 illustrates locations of the respective ROIs.

4.2.3.2 Atmospheric Correction Processors

For our study, we selected common, publicly available AC algorithms. The level of user-controlled parametrization depends on the respective processor and is described in the following. Table 4.4 summarizes the most relevant parameters.

ACOLITE is developed at the Royal Belgian Institute of Natural Sciences and includes AC processors specifically designed for aquatic applications, e.g., it addresses diffuse sky reflectance at the water surface. We used the most recent version that applies a new dark spectrum fitting AC by default (Vanhellemont, 2019). The algorithm consists of five steps (Vanhellemont and Ruddick, 2018): (1) Correction of atmospheric gas transmittance and sky reflectance in the TOA signal; (2) Construction of a dark spectrum using the darkest pixels in each band; (3) Estimation of AOT at 550 nm for different aerosol models (continental, maritime) by linearly interpolating path reflectance from look up

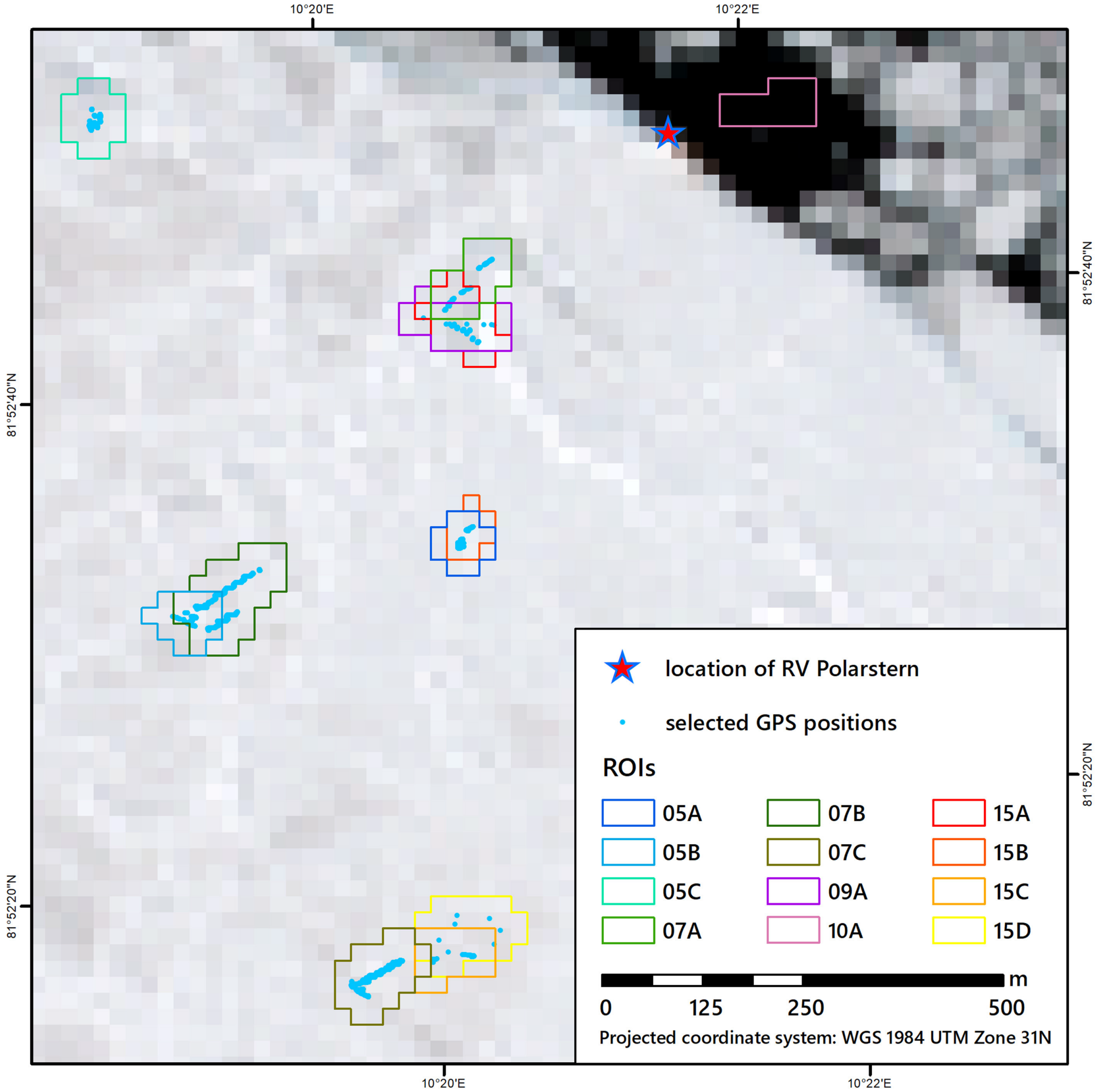

Figure 4.6: ROI locations on the investigated floe. Background: S-2A stretched pseudo-true color RGB image (RGB: 665, 560, and 490 nm, spatial resolution: 20 m) acquired at 2017-06-10 14:58:01 UTC.

tables (LUTs) generated with the Second Simulation of a Satellite Signal in the Second Simulation of a Satellite Signal in the Solar Spectrum-Vector (6SV) radiative transfer model (Vermote et al., 1997); (4) Retaining the band resulting in the lowest AOT for each aerosol model; (5) AC with band and model combination resulting in overall lowest AOT. This approach is presumably more appropriate for ice surfaces than the black short-wave infrared approach of previous versions (Vanhellemont and Ruddick, 2015). Information on precipitable water, atmospheric pressure and ozone concentration are obtained from ancillary data. Adjacency effects are to some extent addressed in the aerosol correction procedure, but are not entirely extinguished (Vanhellemont and Ruddick, 2018). We used the default parameterization but changed the WV default value to 1.14 cm according to the AERONET data. The output of ACOLITE may be images of different reflectances such as surface reflectance or R_{rs} with a 10 m spatial resolution, which was downsampled afterwards.

ATCOR (Atmospheric / Topographic Correction for Satellite Imagery; Richter and Schläpfer, 2017) uses pre-calculated LUTs computed with the Moderate-Resolution Atmospheric Radiance and Transmittance Model–version 5 (MODTRAN 5) (Berk et al., 2008) and image-based retrievals of atmospheric properties. The LUTs cover four aerosol models (rural, urban, maritime, and desert) and six water vapor column contents (0.4–5.0 cm). Varying ozone concentrations are addressed via an extra ozone database. The dense dark vegetation method is used to derive AOT and the aerosol type can be estimated by comparison of derived path radiance with MODTRAN standard aerosol types. WV is estimated using the Atmospheric Pre-corrected Differential Absorption algorithm. The resulting unit is "bottom of atmosphere" (BOA) reflectance (Richter and Schläpfer, 2017). The interface of ATCOR guides the user through the parametrization of the processor, which enables to address emerging problems. The small number of dark pixels in the image hampered an image-based retrieval of aerosol type and AOT. A WV map could be generated, but values near the vessel were high ($\sim$ 1.8 cm) compared to the AERONET data. To parametrize the processor in accordance to the AERONET data, we therefore selected the pre-defined maritime aerosol type and a stable WV of 1.0 cm, which is the closest selectable default value, compared to the AERONET data. Visibility as a measure for AOT was set to 65 km. ATCOR considers adjacency effects as averaged reflectance of the neighborhood of a pixel (Richter and Schläpfer, 2017); its impact therefore depends on the difference in reflectance of a pixel and its neighborhood and decreases exponentially with increasing distance. Thus, for recurrent spatial patterns, adjacency effects remain similar at different spatial scales; consequently, the absolute range of the adjacency correction is uncritical. Therefore, we selected a typical range of 1 km (Richter and Schläpfer, 2017). The number of adjacency zones remained unchanged (1). We further applied a cirrus correction and selected the 20 m spatial resolution output.

Table 4.4: Parametrization of AC processors used in this study.

Processor	**Version**	**References**	**LUT radiative transfer model**	**Applied aerosol model**	**AOT retrieval**	**WV retrieval**	**Adjacency correction**
ACOLITE	20180419	Vanhellemont (2018), Vanhellemont and Ruddick (2018)	6SV	Image based; continental	Dark spectrum fitting	Ancillary data	No
ATCOR-2	9.1.2	Richter and Schläpfer (2017)	MODTRAN 5	User-defined; maritime	User defined visibility; 65 km	User defined: 1.0 cm	Yes
iCOR	0.1	Sterckx et al. (2015a), VITO (2017), De Keukelaere et al. (2018)	MODTRAN 5	Fixed: rural	Image-based	Fixed: 2.0 cm	Yes
Polymer	4.0	Steinmetz et al. (2011)	Successive Order of Scattering	None (polynomial model for atmospheric path reflectance)	Iterative coupled ocean-atmosphere optimization scheme	No	Yes, through AC
Sen2Cor	2.4.0.	Müller-Wilm (2016)	libRadtran	User-defined: maritime	Image-based	Image-based	Yes

In this study, we also used iCOR version 0.1 in ESA's Sentinel Application Platform (SNAP; v5.0). iCOR, previously known as OPERA (Sterckx et al., 2015a), is an AC processor for land and water as it accounts for the non-Lambertian reflectance of water surfaces. The iCOR workflow comprises four steps (De Keukelaere et al., 2018): (1) Classification of land/water pixels; (2) AOT retrieval over land following the approach in Guanter (2006), and extension to adjacent water pixels assuming a spatially homogeneous atmosphere; (3) adjacency correction; (4) AC using pre-calculated MODTRAN 5 LUTs based on a rural aerosol model (De Keukelaere et al., 2018). In the current iCOR SNAP version, WV is fixed to 2.0 cm. Over water the adjacency effect is corrected using the SIMilarity Environment Correction (SIMEC) approach (Sterckx et al., 2015b) while over land the user defines a fixed range (Sterckx et al., 2015a; VITO, 2017). We applied the adjacency correction and increased the default adjacency window for land surfaces to three pixels (tests with larger values introduced a reflectance peak at 705 nm). Further, we adjusted the default AOT value to 0.02 according to the AERONET data. Besides that, we used the default parameter setting. iCOR returns BOA reflectances in the native resolution of the respective band.

The polynomial-based atmospheric correction algorithm Polymer (Hygeos France Steinmetz et al., 2011) is an AC processor for water bodies applicable to multiple sensors, including MSI and OLCI. Polymer is a spectral matching algorithm, which decouples the reflectance signal of the water body from atmospheric and water surface reflectance. It makes use of the observation that the sum of atmospheric path reflectance and adjacency effects can be approximated by a polynomial consisting of three terms that address (1) non-spectral scattering or reflection, (2) fine aerosol scattering and (3) molecular scattering and adjacency effects, and does not require an aerosol model (IOCCG, 2015). One of the strengths of Polymer is the possibility to retrieve R_{rs} in presence of sun glint, which leads to a higher yield of evaluable pixels compared to other algorithms. Recently, the Polymer algorithm has been modified to improve results in high latitudes (Steinmetz and Ramon, 2018). In the processing chain, non-water surfaces are masked, i.e., Polymer has only been applied to ROI 10A. For this study, the Polymer 10 m outputs were projected and resampled to the Sentinel-2 grid using the Nearest Neighbor approach, and spatially downsampled to 20 m resolution by 2 × 2 pixel block averaging.

Sen2Cor is the Sentinel-2 Level-2A Prototype processor for land surfaces. For this paper, we used the stand-alone version of Sen2Cor 2.4.0, which also allows for an image-based retrieval of atmospheric parameters. Water vapor is derived with the Atmospheric Pre-corrected Differential Absorption algorithm applied to S-2 bands 8A and 9. Sen2Cor estimates AOT by means of the dense dark vegetation method using the relation of the reflectance in bands 4, 2, and 12. The image-derived atmospheric parameters are then associated with pre-computed LUTs generated by a libRadtran based radiative transfer model. The LUTs include two atmospheric models (mid-latitude summer and winter), two aerosol types (maritime, rural), six or four different WV column values and six ozone concentrations (Müller-Wilm, 2016). We chose the maritime aerosol type and selected the mid-latitude winter model atmosphere as suggested in Harris Geospatial Solutions Inc. (2018). We activated the variable visibility option and changed the default value to 65 km.

4.2.4 Perfomance Measures

We performed the spectral measurements on the floe within 5 days before and after the satellite acquisition. Illumination conditions therefore differed for field measurements and the satellite observation (see Section 7.2.2.1) which may affect measurement results (Malinka et al., 2016). Moreover, due to the different spectrometer setups described in Section 7.2.2.1.1, ASD and Ocean Optics show varying sensitivities to changing illumination conditions. The different FOVs result in varying sensitivities to changing sensor-surface geometries. An inter-comparison of ASD and Ocean Optics under field conditions revealed mean differences in surface reflectance of about 0.1; a comparison of *in situ* spectra and BOA reflectances by means of classic performance metrics such as bias or root mean squared error therefore is unreasonable.

To identify systematic differences between the respective processors, i.e., the average tendency of the BOA reflectance to be larger or smaller than TOA reflectance, we computed the percentage bias (PBIAS) as

$$PBIAS = 100 \cdot \frac{\sum_{i=1}^{n}(R^{AC}(\lambda_i) - R^{TOA}(\lambda_i))}{\sum_{i=1}^{n}(R^{TOA}(\lambda_i))} \tag{4.3}$$

with R^{AC} and R^{TOA} being the bottom and top of atmosphere reflectance at band λ_i, respectively; n is the number of bands.

Compared to the absolute values, spectral shapes are more stable, especially at the beginning of the melt season and for the visible wavelength regions (Perovich and Richter-Menge, 1994). We therefore evaluated the spectral shapes of ice and snow measurements on the floe, computing the slope between two adjacent bands and then calculate the slopes' Mean Absolute Error (slope MAE):

$$slope\ MAE = \frac{1}{n}\sum_{i=1}^{n}|S^{AC}(\lambda_i, \lambda_{i+1}) - S^{in\ situ}(\lambda_i, \lambda_{i+1})| \tag{4.4}$$

with $S^{AC}(\lambda_i, \lambda_{i+1})$ being the slope of the BOA reflectance outputs of the respective AC processor and $S^{in\ situ}(\lambda_i, \lambda_{i+1})$ being the slope of the resampled *in situ* reflectance between band λ_i and band λ_{i+1}, respectively; n is the number of band pairs. We further calculated the coefficient of determination (r^2) as the square of Pearson's correlation coefficient to evaluate linear correlations between the respective AC BOA output and the *in situ* measurement:

$$r^2 = \left(\frac{\sum_{i=1}^{n} (R^{in\ situ}(\lambda_i) - \overline{R^{in\ situ}}) \cdot (R^{AC}(\lambda_i) - \overline{R^{AC}})}{\sqrt{\sum_{i=1}^{n} (R^{in\ situ}(\lambda_i) - \overline{R^{in\ situ}})^2} \cdot \sqrt{\sum_{i=1}^{n} (R^{AC}(\lambda_i) - \overline{R^{AC}})^2}} \right)^2 \tag{4.5}$$

with R^{AC} being the output of the respective AC processor and $R^{in\ situ}$ situ being the reflectance of the resampled *in situ* spectrum at band λ_i (band 2–7); n is the number of bands.

For deep polynya water, we performed measurements of R_{rs} from the deck of the vessel parallel to the satellite overpass under clear-sky conditions. No white referencing was necessary due to the measurement setup, which already integrates changes in illumination conditions. We therefore compared resulting reflectance intensities. ACOLITE calculates R_{rs}, while ATCOR, iCOR, SEN2COR and Polymer yield surface reflectances. The surface reflectances were transformed into R_{rs} following Mobley et al. (2018):

$$R_{rs} = \frac{R^{AC}}{\pi} \tag{4.6}$$

with R^{AC} being the surface reflectance output of the respective AC processor. We then computed MAE to account for differences in reflectance intensity according to:

$$MAE = \frac{1}{n} \sum_{i=1}^{n} |R_{rs}^{AC}(\lambda_i) - R_{rs}^{insitu}(\lambda_i)| \tag{4.7}$$

with R_{rs}^{AC} being R_{rs} of the respective AC processor and R_{rs}^{insitu} being R_{rs} of the resampled *in situ* spectrum at band λ_i (band 2–8A); n is the number of bands. To evaluate correspondence in spectral shapes, we computed slope MAE and r^2, replacing surface reflectance with R_{rs} and expanding S-2A band selection by band 8A.

4.3 Results

Due to the different measurement designs described above, we discuss the results for open water as well as snow and ice surfaces separately.

4.3.1 Snow and Ice Surfaces

Figure 4.7A,C,E illustrates the mean shape and intensity of S-2A TOA reflectances, BOA reflectances of the respective AC processors and resampled *in situ* spectra from snow and ice surfaces. Due to the low variance, we computed the mean spectra of all ROIs on the floe. *in situ* spectra show the typical shapes of snow and ice with maximum reflectances in the blue-green wavelength region and a decrease toward longer wavelengths. Maximum mean *in situ* reflectances at band 2 (490 nm) range from approximately 0.8–1.1 with high standard deviations presumably resulting from a high spatial variability on sub-pixel scale. Values are in line with field measurements from other studies (e.g. Perovich, 1998;

Goyens et al., 2018). In comparison to the TOA spectrum, BOA spectra for all AC processors show increased reflectances over the entire spectrum. For each ROI, Sen2Cor produces the highest BOA reflectances, also indicated by high PBIAS values (Table 4.5). On average, Sen2Cor BOA reflectances are about 30 % higher than TOA reflectances. BOA reflectances of iCOR (mean PBIAS: 10.8 %) and ATCOR (mean PBIAS: 11.7 %) are generally lower than Sen2Cor values and resemble each other in intensity and shape. Yet, in comparison to iCOR, ATCOR BOA reflectances decrease slightly with shorter wavelengths. ACOLITE BOA reflectances are lowest for all ROIs and only 6.6 % higher than TOA reflectances, on average. Figure 4.7E illustrates the slopes of the respective spectra showing largest differences for Sen2Cor (mean slope MAE: 1.17E–03); high slope MAE values in Table 4.5 confirm this observation. For iCOR (mean slope MAE: 2.64E-04) and ATCOR (mean slope MAE: 2.29E–04), Figure 4.7E highlights differences in bands 2–4 and similarities in bands 5–7. Overall, ACOLITE fits the shape of the resampled *in situ* spectrum best, also indicated by low slope MAE values in Table 4.5 (mean slope MAE: 1.92E–04). Coefficients of determination in Table 4.5 confirm this trend and are highest for ACOLITE (mean r^2: 0.9758), followed by ATCOR (mean r^2: 0.9728) and iCOR (mean r^2: 0.9702), while Sen2Cor shows the weakest linear relationship (mean r^2: 0.9137), on average.

4.3.2 Open Water

Figure 4.7B,D,F illustrates the results for the open water measurements. It is obvious that ACOLITE and Sen2Cor intensities are one order of magnitude higher than the *in situ* values, also demonstrated by high MAE values inTable 4.6. High coefficients of determination ($r^2 \sim 0.96$), however, indicate a strong linear correlation between resampled *in situ* and R_{rs} spectra, although the spectral slope is different (slope MAE in Table 4.6 and Figure 4.7). iCOR average R_{rs} is almost 10 times higher than average *in situ* data (MAE $\sim$ 0.01), but spectral shape is more similar compared to ACOLITE and Sen2Cor indicated by a small slope MAE (2.17E–05) and high r^2 ($\sim$ 0.97). Polymer retrieved R_{rs} are in the same order of magnitude as measured R_{rs}, illustrated by a small MAE of 0.0015, while ACOLITE, iCOR and Sen2Cor overestimate R_{rs}. The lowest slope MAE (1.54E–05) indicates that Polymer resembles the shape of the *in situ* spectrum most accurately. The comparably weak correlation ($r^2 \sim 0.85$) results from a drop of the spectrum in bands 5–8A (Figure 4.7B). The ATCOR output is also in the correct order of magnitude over the full spectrum and has the smallest MAE and a comparable low slope MAE. It has to be noted, however, that the spectral shape in the visible range differs, also indicated by a weak linear correlation ($r^2 \sim 0.18$). The slope MAE is higher than for Polymer, highlighting the difference in shape in visible bands 2 (490 nm) to 4 (665 nm).

Table 4.5: Performance measures of resampled mean *in situ* and BOA spectra for different ROIs on the ice floe.

ROI	**AC Processor**	**PBIAS**	**r^2**	**Slope MAE**
05A	ACOLITE	6.6	0.994026	1.41E-04
	ATCOR	12.2	0.988867	2.07E-04
	iCOR	11.0	0.981445	2.90E-04
	Sen2Cor	30.0	0.919942	1.20E-03
05B	ACOLITE	6.6	0.980658	1.90E-04
	ATCOR	11.5	0.986336	1.71E-04
	iCOR	9.3	0.987513	2.29E-04
	Sen2Cor	29.8	0.923357	1.17E-03
05C	ACOLITE	6.6	0.970177	1.61E-04
	ATCOR	12.2	0.977065	2.27E-04
	iCOR	12.5	0.982563	2.46E-04
	Sen2Cor	29.5	0.923	1.16E-03
07A	ACOLITE	6.6	0.981395	2.09E-04
	ATCOR	12.2	0.975791	2.74E-04
	iCOR	11.7	0.948195	3.71E-04
	Sen2Cor	29.6	0.893718	1.22E-03
07B	ACOLITE	6.6	0.986113	2.71E-04
	ATCOR	11.7	0.981915	3.16E-04
	iCOR	10.4	0.989948	3.70E-04
	Sen2Cor	29.9	0.938893	1.25E-03
07C	ACOLITE	6.6	0.877007	4.20E-04
	ATCOR	10.4	0.844808	4.55E-04
	iCOR	9.5	0.815684	4.98E-04
	Sen2Cor	29.6	0.758376	1.35E-03
09A	ACOLITE	6.6	0.99323	1.38E-04
	ATCOR	12.5	0.995584	1.45E-04
	iCOR	11.4	0.993827	1.35E-04
	Sen2Cor	29.8	0.94577	9.98E-04
15A	ACOLITE	6.6	0.990641	1.98E-04
	ATCOR	12.4	0.994046	2.41E-04
	iCOR	12.7	0.985452	2.95E-04
	Sen2Cor	29.8	0.938485	1.18E-03
15B	ACOLITE	6.6	0.985177	1.26E-04
	ATCOR	12.2	0.990944	1.64E-04
	iCOR	11.0	0.994962	1.62E-04
	Sen2Cor	30.0	0.943851	1.06E-03
15C	ACOLITE	6.6	0.988243	1.44E-04
	ATCOR	12.2	0.985885	1.49E-04
	iCOR	11.7	0.994527	1.74E-04
	Sen2Cor	29.6	0.927905	1.13E-03
15D	ACOLITE	6.6	0.987401	1.12E-04
	ATCOR	10.5	0.980002	1.69E-04
	iCOR	9.7	0.997854	1.39E-04
	Sen2Cor	29.8	0.937539	1.13E-03
Mean	ACOLITE	6.6	0.975824	1.92E-04
	ATCOR	11.7	0.972840	2.29E-04
	iCOR	10.8	0.970179	2.64E-04
	Sen2Cor	29.8	0.913712	1.17E-03

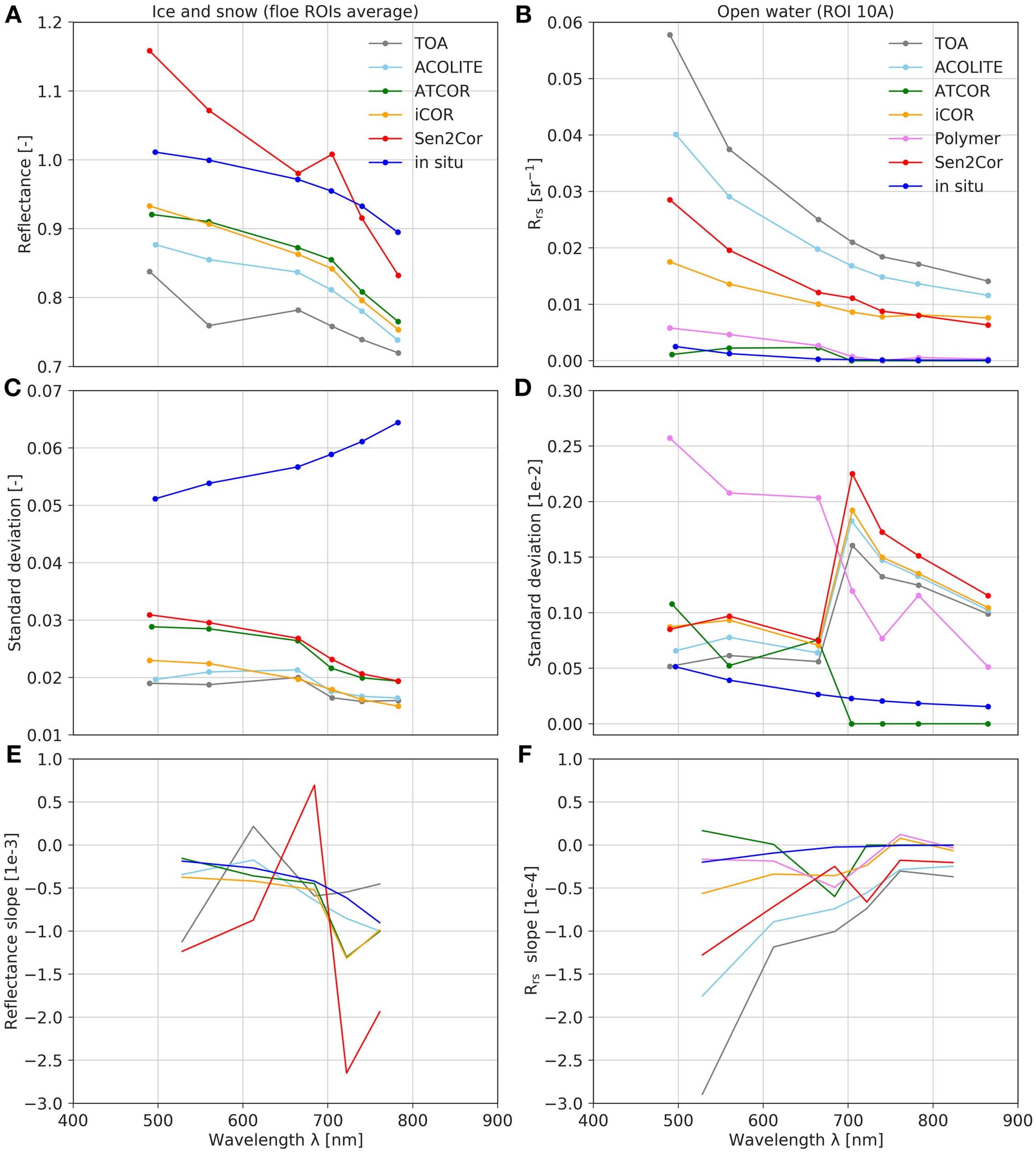

Figure 4.7: Mean resampled *in situ* spectrum, S-2A TOA spectrum and BOA outputs of different AC processors for ice and snow ROIs (A), respective standard deviations (C) and spectral slopes (E). Mean resampled *in situ* spectrum, S-2A TOA and BOA R_{rs} outputs of different AC processors for the open water ROI 10A (B), respective standard deviations (D) and spectral slopes (F).

Table 4.6: Performance measures of resampled mean *in situ* and R_{rs} spectra for respective AC processors in comparison with mean resampled *in situ* spectrum at ROI 10A.

AC Processor	**PBIAS**	**r^2**	**Slope MAE**
ACOLITE	0.0202	0.9613	6.88E-05
ATCOR	0.0007	0.1848	1.78E-05
iCOR	0.0098	0.9709	2.17E-05
Polymer	0.0015	0.8497	1.54E-05
Sen2Cor	0.0128	0.9657	4.90E-05

4.3.3 Application Examples

To illustrate the consequences of different ACs on parameter retrieval, we computed the average BOA reflectance from band 2 to 7 (490–782 nm) as a rough approximation to broadband albedo (Figure 4.8). In addition, we calculated NDMI, which can be used as a proxy for melt pond fraction (Istomina and Heygster, 2017) according to

$$NDMI = \frac{\lambda_{Green} - \lambda_{NIR}}{\lambda_{Green} + \lambda_{NIR}} \tag{4.8}$$

where λ_{Green} is S-2 band 3 (560 nm) and λ_{NIR} is S-2 band 8A (865 nm) from the respective AC product. Theoretically, NDMI values range from –1 to +1. Due to the specific reflectance characteristics of the different sea ice surfaces in these wavelength regions the value range, however, is practically limited to values > 0. Increasing values indicate an increasing melt pond fraction. Figure 8 illustrates that the AC processor influences parameter retrieval and, in reverse, that the application rules the choice of AC processor. Note that median TOA reflectance of the floe surface is 0.75, and BOA reflectances are approximately 0.80 in the ACOLITE product and ~ 0.84 in the ATCOR and iCOR products, reaching 0.97 in the Sen2Cor product. In general, NDMI results show the same pattern, whereas median NDMI values are lowest for TOA (0.06), followed by ACOLITE (0.12), ATCOR (0.13), iCOR (0.14), and Sen2Cor (0.18). This corresponds to the spectral behavior illustrated in Figure 4.7.

4.4 Discussion

4.4.1 Comparability of Field and Satellite Data

The comparison of field spectroscopy and satellite observations involves a number of difficulties, which particularly applies to remote regions such as the Arctic where ideal measurement opportunities and coincident satellite overpasses are rare. We conducted spectral measurements of the floe surface within a period of ±5 days of the satellite overpass un-

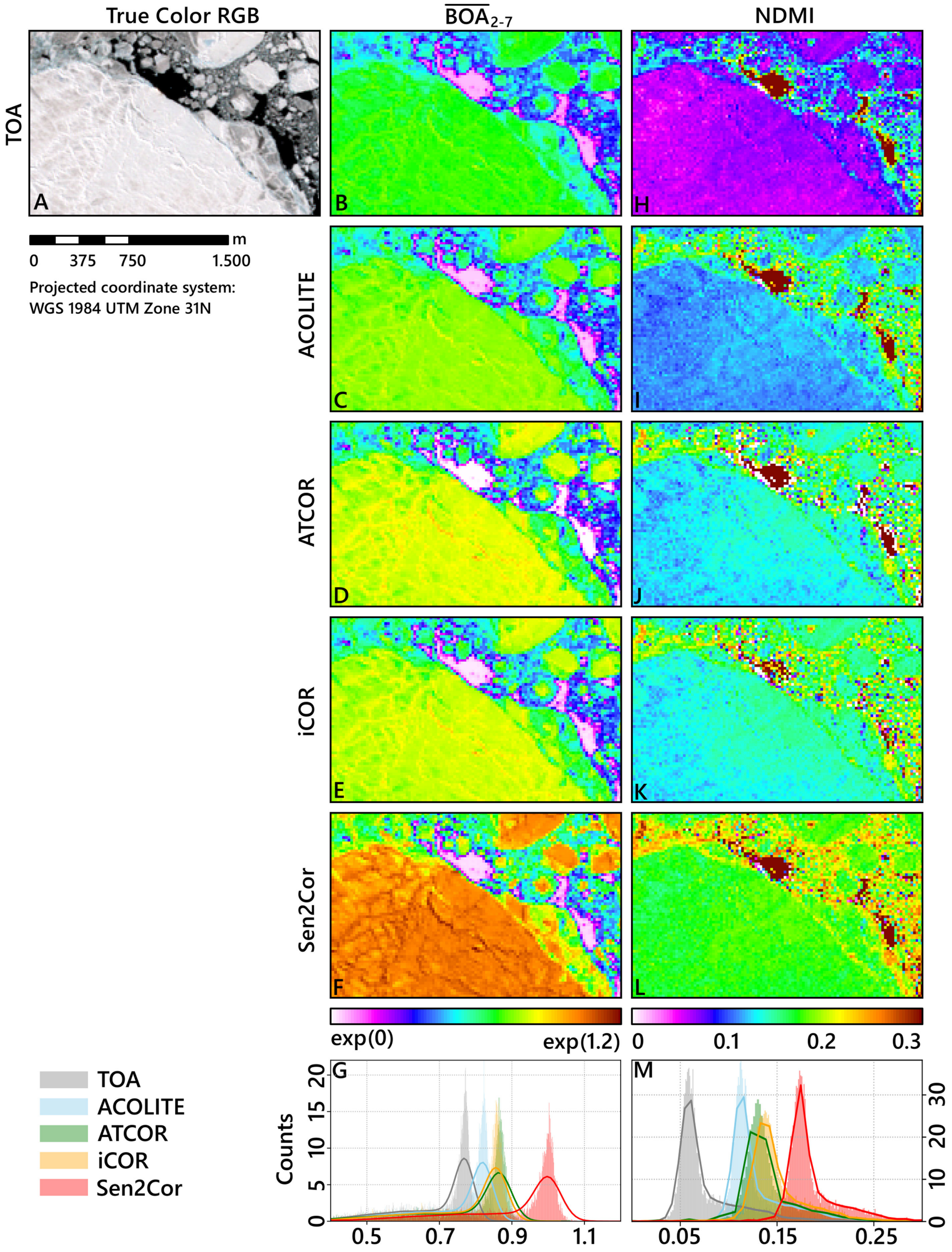

Figure 4.8: True color RGB image (A); band 2–7 average of TOA (B) and BOA (C–F); NDMI results for TOA (H) and BOA (I–L); and histograms of the respective parameters for the image subset (G,M).

der varying illumination conditions and possibly changing surface properties due to the onset of melt. We postulate, however, that an analysis of spectral shapes is reasonable as the anisotropic reflectance factor of snow at nadir is ~ 1 (Perovich and Richter-Menge, 1994) and the shape of the spectral albedo is constant under different illumination angles (Malinka et al., 2016). For snow surfaces, Goyens et al. (2018) and Bourgeois et al. (2006) observed no significant relationship between variations in reflectance anisotropy with illumination conditions for sun zenith angles $< 65°$. In addition, the effect of melt on the spectral shape of nadir reflectance of snow and ice is comparably low in the VIS (Perovich and Richter-Menge, 1994; Perovich, 1998). Nevertheless, we are unable to exclude potential differences in spectral slope due to melt processes. Besides the temporal differences, it is challenging to represent the spatial variability within a 20 m × 20 m area measured by S-2A via field measurements, even when measured at different locations. Moreover, a re-location of the measurement positions on a drifting floe in combination with spatial uncertainties of both GPS devices and satellite image positioning exacerbates a point-by-pixel comparison. For this reason, we included surrounding pixels into the analysis. However, this method is vulnerable to extreme spectral features in a ROI that can have a great impact on the average spectrum. The standard deviations of the ROIs located on the floe, however, are small indicating low spectral variability (Figure 4.7C); we therefore assume the ROI approach to be a valid method for evaluating the AC processors. ROI 10A over open water was defined manually and excluded pixel with unusual shape, presumably resulting from sub-pixel contamination due to floating ice. This pre-selection may substantially influence the outcome of the study, as pixel with expected shape are preselected. The pre-selection, however, avoids integration of extreme spectral features, which may have a major influence on the average spectrum due to sub-pixel contamination.

4.4.2 Quality of *In Situ* Data

For some ROIs, field spectrometer data show reflectances > 1.0, although both field spectrometer setups were calibrated with reflectance standards. The Ocean Optics setup also enabled the correction of illumination changes. For ASD measurements, we surveyed changes in illumination by measuring the reflectance standards before each subsequent calibration. We manually deleted ASD measurements affected by illumination changes, i.e., spectra with unusual shape. Successive spectra with stable shape showing reflectances > 1.0, however, remained in the dataset. In addition to the differences regarding sensitivity to changes in illumination, both setups vary regarding their FOVs. The smaller FOV of the Ocean Optics makes it more vulnerable to twisting of the pole and anisotropic effects due to ice surface topography. An inter-comparison of spectrometers in the field revealed that Ocean Optics reflectance values are ~ 0.1 higher than ASD reflectances, on average, while the spectral shape was very similar. Warren (1982) stated that cloud cover affects both the spectral distribution of irradiance and the effective incident zenith angle, which causes an increase in all-wave snow albedo of up to 11 %. Painter and Dozier (2004) attributed reflectances > 1.0 to anisotropic effects of snow, which depend on the sun zenith angle, the grain size and the viewing geometry. Anisotropic effects may also have influenced the measurements described by Goyens et al. (2018) and Perovich (1998), who report reflectances > 1.0 at approximately 400 nm measured under clear sky conditions. Peltoniemi et al. (2005) included snow wetness as an additional parameter influencing the spectral albedo and anisotropic behavior of snow and ice surfaces. As we evaluate the spectra only regarding to their shape, however, results remain unaffected by values > 1.0. Analysis of water samples in the deep-water polynia show no significant absorption or scattering of the water constituents in the near infrared spectral range (> 700 nm). Accordingly, beyond the visible range, measured R_{rs} is smaller than 1.5×10^{-4}, i.e., near zero (black) in the near infrared. Measurements influenced by ice floating into the FOV of the RAMSES spectrometer were excluded from the evaluation. The AERONET AOT values (~ 0.02) are within the range reported for typical Arctic background aerosol concentrations, with values between 0.02 and 0.08 (Tomasi et al., 2012; IOCCG, 2015).

4.4.3 AC Processors

Differences between BOA or R_{rs} products may originate from the different processors, the integrated LUTs, different parameterization and image-based parameter retrieval regarding WV content, aerosol type and AOT, or different adjacency correction schemes, and the interplay of these components. Varying options for the user to modify the parameterization further complicate a direct comparison. Moreover, some of the processors are still under development and not yet entirely documented which hinders a detailed reasoning.

The LUTs applied in the AC processors have been generated with different radiative transfer models (MODTRAN 5, 6SV, libRadtran, and Successive Order of Scattering). These models differ regarding the implementation of physical equations, approximation of the radiative transfer equation and subroutines which can result in differences (e.g. Callieco and Dell'Acqua, 2011). Evaluating the impact of a certain radiative transfer model on AC, however, is beyond the scope of this study. The aerosol models covered by the precalculated LUTs cover common aerosol types. The options, however, differ between the AC processors (Section 7.2.3.2). It is questionable how well these models represent Arctic aerosol components, e.g., mineral dust, sulfate aerosols and sea salt (at Barrow, Alaska Tomasi et al., 2012; IOCCG, 2015). In late spring and summer, a phenomenon known as Arctic Haze results from anthropogenic aerosol accumulation in winter is common and occasionally aerosols from forest fires or volcanic eruptions are observed (IOCCG, 2015). To analyze the impact of the aerosol model we conducted a sensitivity analysis with different aerosol models in ATCOR. For the desert, maritime and rural aerosol models, differences in the VIS bands for the bright snow and ice surfaces were ~ 2 %, while the urban aerosol model resulted in an increase of $\sim$ 5–10 % reflectance.

ACOLITE is designed for aquatic applications; the main differences compared to other AC processors are the AOT retrieval by the dark spectrum fitting algorithm and the consideration of skyglint. Its performance over ice surfaces, however, is good regarding the shape of BOA reflectance spectra. For sea ice surfaces differences in surface reflectance due to skyglint correction are < 0.02. No water vapor and ozone values could be obtained from ancillary data, which might due to the developmental state of the processor; thus, the default values were used for AC and it remains unclear if the retrieval of water vapor and ozone in the Arctic from ancillary data is possible. Given the applied parameterization, the dark spectrum fitting algorithm results in the application of a continental aerosol model and an AOT of 0.0084 at 550 nm, i.e., comparably close to the measured value of 0.02 (AERONET-MAN reports uncertainties 0.02 per band NASA Goddard Space Flight Center, 2017). We assume that the high R_{rs} values over water result from adjacency effects, which are not addressed by ACOLITE.

ATCOR performs well over ice surfaces while its performance over open water is poor as the spectral shapes of BOA and *in situ* data do not correspond. Due to the lack of dark pixels in the S2-A data set we defined AOT by visibility (65 km), illustrating that the dark vegetation method is unsuitable for AOT retrieval in this image. For WV, image-based retrieval resulted in an overestimation of WV ($\sim$ 1.8 cm). We therefore defined a default value (1.0 cm) referring to the AERONET data. Few pixels (1.2–1.4 %) of bands 5–9 show negative reflectance values at open water areas, which may be caused by underestimated visibility, the aerosol type or calibration issues. Application of haze removal was not possible due to the small amount of clear pixels ($<$ 4 %). Increasing the visibility parameter (up to 120 km) only had negligible consequences for the snow and ice surfaces and did not improve the spectral shape of open water pixels. This corresponds to Huck et al. (2007) who found that increasing visibility in a 6S forward simulation for AVHRR only affects open water surfaces. Changing the WV content from 1.8 to 1.0 cm had a significant influence, especially in S-2 bands that cover WV absorption features, i.e., band 8 (842 nm), band 9 (940 nm), and also band 5 (705 nm). For simulated Sea-viewing Wide Field-of-view Sensor (SeaWiFS) like spectra at the edge between sea ice and open water, Bélanger et al. (2007) found contaminations due to the adjacency effect up to 24 km off the ice edge resulting in unreliable results in derived chlorophyll concentrations and optical properties of open ocean water. Bulgarelli and Zibordi (2018) found that for S-2/MSI adjacency effects caused by highly reflecting surfaces (e.g., snow) are theoretically detectable at least 20 km off the coast in mid-latitude coastal environments. In contrast to these simulations, the area of interest is characterized by a small-scale mixture of snow, ice, melt ponds and open water, where spatial patterns and average reflectance are similar on different spatial scales. To check whether this statement applies for sea ice, we tested different ranges (1, 3, 5, and 10 km) and results confirmed that the influence is negligible for the spectral shape of the snow surface and intensity of open water pixels.

iCOR addresses the requirements for aquatic and terrestrial surfaces including a correction of adjacency effects. iCOR was unable to assess AOT from the image as the retrieval algorithm relies on vegetation and soil pixels (De Keukelaere et al., 2018), questioning the suitability of this approach for the Arctic sea ice in the absence of *in situ* AOT values. Even though, the fixed WV column height of 2.0 cm showed good results over ice, iCOR's unknown sensitivity to WV aggravates AC processor inter-comparison. The good performance over water compared to ACOLITE and Sen2Cor is probably attributed to the correction of adjacency effects using the SIMEC algorithm. For the application of SIMEC, Sterckx et al. (2015b) point out that aerosol information (AOT and aerosol model) should be either estimated using a land-based aerosol retrieval or from sun photometer data. While we used AERONET data to set the default AOT, we could not parameterize the aerosol type. Further, SIMEC is based on the assumption that reflectance differences between water and surrounding surfaces are strongest in the NIR, which is true for vegetated surfaces but not for ice, where differences are strongest in the VIS. We found that iCOR is very sensitive to changes in AOT. Increasing AOT from 0.02 to 0.1 resulted in an overcorrection and, consequently, a decrease of the spectrum matching the *in situ* measurements very well (slope MAE $\sim$ 8.49E-06).

Polymer performs best over water and produces reasonable results even in the high contrast Arctic sea ice matching findings of Steinmetz and Ramon (2018). It is robust to adjacency effects because the atmospheric model fits any spectrally smooth non-water component (Steinmetz and Ramon, 2018). The manual definition of ROI 10A guaranteed that we only considered deep-water pixels, which may also be important for the good performance of Polymer. Nevertheless, we observe a high spectral variability in the VIS bands. Moreover, some negative values appear in the red-edge and NIR regions. Sub-pixel contamination due to floating ice should be corrected due to its spectrally-flat contribution to the reflectance signal.

Usually, Sen2Cor applies image-based retrievals to generate maps of AOT and WV. The lack of dark pixels in the S-2A image, however, prohibited an AOT retrieval based on the DDV method; thus, AOT was estimated from the provided visibility (65 km). Values for scene average WV and AOT at 550 nm are 1.51 cm and 0.132, respectively. Compared to the AERONET data, however, both values are very high. A further test with a fixed visibility of 120 km, corresponding to an AOT of $\sim$ 0.0780, as proposed by Pflug et al. (2016) as a good practice for clear air and low AOT over Antarctica, did not improve the results for BOA reflectance and R_{rs} significantly. The increased BOA reflectance in comparison to the other processors fit findings of Li et al. (2018) who report that surface reflectance derived with Sen2Cor is generally overestimated, in particular for bright pixels. The high values over water may be attributed to the lacking correction of skyglint and adjacency effects or the provided LUTs.

A general challenge in high latitudes is the low sun elevation throughout long periods of the year. Huck et al. (2007) found that the solar zenith angle has a major influence on the retrieved TOA reflectance of a nadir-viewing sensor. The low reflectance levels of water bodies further increase this effect, because atmospheric path length increases with decreasing sun elevation. Consequently, the amount of energy absorbed in the atmosphere increases while the amount that arrives at the Earth's surface decreases. At the same time, the amount of light that is specularly reflected at the water surface increases with decreasing sun elevation, while a lower amount is transmitted into the water body. As a consequence, the water body scatters less light toward the sensor (Hieronymi, 2013). Further, the influence of surface roughness on the transmission of light into the waterbody increases with sun zenith angle which challenge wind speed-dependent AC (Hieronymi, 2016). When the sun is close to the horizon, adjacent ice floes may also have a shading effect. The same applies for ice floes, where shadows of ridges increase with lower sun elevation and anisotropic effects increase for sun zenith angles $> 65°$ (Bourgeois et al., 2006). Another issue regarding low sun elevation is the limitation of most processors to sun zenith angles $\leq 70°$. The reason is that the LUTs are generated with radiative transfer models that base on the assumption of a plane parallel atmosphere rather than an actual spherical-shell atmosphere (IOCCG, 2015). Since in our study the sun zenith angle is 62.5°, we assume that this effect is negligible.

4.4.4 Sentinel-2A Data

Typically, reflectance spectra of snow and ice (like *in situ* spectra) are characterized by a steady decrease from the blue domain toward longer wavelength regions. S-2A TOA spectra, however, show a steep decrease from band 2 to 3 (490 and 560 nm, respectively), followed by an increase from band 3 to 4 (560–665 nm; Figure 4.7A). A comparison of BOA reflectance spectra with typical spectra found in literature (e.g., Perovich and Richter-Menge, 1994; Perovich, 1998) indicates that ACOLITE, ATCOR and iCOR produce realistic results. As described in (Section 7.4.1), however, melt processes may have caused reflectance changes between *in situ* and satellite data. Thus, the evaluation of BOA spectral shape is challenging. In general, however, BOA shapes of ACOLITE, ATCOR, and iCOR are similar to the shape of the *in situ* spectra, i.e., the differences in slope MAE and r^2 are small. The shapes of Sen2Cor BOA reflectances do not resemble the typical shapes of snow and ice spectra as they show a steep decrease from the blue wavelength region toward longer wavelengths, interrupted by a local peak in band 5 at 705 nm. Furthermore, Sen2Cor is the only processor that produces reflectance values > 1.0. Nadir reflectances of snow and white ice may exceed 1.0 in the blue part of the electromagnetic spectrum (e.g., Perovich and Richter-Menge, 1994; Goyens et al., 2018) but Sen2Cor BOA reflectances exceed 1.0 even in bands 3 and 4 (560 and 665 nm, respectively). This may result from anisotropic effects due to snow parameters or floe topography and matches observations of Li et al. (2018) who found that Sen2Cor overestimates BOA reflectance; ACOLITE, ATCOR, and iCOR BOA reflectance values, however, are < 1.0 in all bands.

4.4.4.1 Application Examples

As indicated in Section 7.3.3, the choice of AC processor influences parameter retrieval. The differences in BOA reflectance illustrated in Figure 4.7 have a great impact on NDMI and surface albedo (Figure 4.8), which is roughly approximated here by the mean BOA reflectance of bands 2–7 (490–783 nm). The shifted peaks in the histograms refer to the offset-like behavior of the spectra from different AC processors illustrated in Figure 4.7. The example illustrates well that the application of a certain AC processor and resulting BOA reflectances affects the retrieval of geophysical parameters from S-2A imagery.

4.5 Conclusion

ESA's S-2 mission shows high potential to assist sea ice research. The high spatial resolution allows detailed observation of small-scale sea ice features such as ridges and melt ponds. Thus, S-2 can be used to bridge the spatial scale between *in situ* observations and very high spatial resolution imagery, e.g., from airborne sensors, to coarse resolution sensors such as Sentinel-3. Even though geographical coverage in the Arctic Ocean is currently limited to areas close to the shore, coverage may be extended on request (European Space Agency, 2015). The temporal scale may be bridged either by comparison of identical granules from multiple dates or by multiple images of the same floe. For all subsequent applications such as change detection and time series analysis, however, AC is a crucial step in the processing chain of S-2 data as it is a requirement for an accurate retrieval of geophysical parameters.

We applied five AC processors for S-2 (i.e., ACOLITE, ATCOR, iCOR, Polymer, and Sen2Cor) to a S-2A dataset acquired north of Svalbard on June 10, 2017 and analyzed the results for snow and ice surfaces as well as for deep-water areas. For this dataset, the ACOLITE dark spectrum fitting algorithm resembled the shape of the mean resampled *in situ* spectra of the floe surface in the wavelength region 490–783 nm most accurately, closely followed by ATCOR and iCOR. Considering potential influences of melt on the spectral slope, a conclusive assessment, however, is challenging as ACOLITE, ATCOR and iCOR resembled the typical shape of snow reflectance. Results of this study, however, indicate that the present version of Sen2Cor is unsuitable for applications in the Arctic sea ice.

Due to the field measurement setup, our study was incapable of evaluating AC quality in terms of absolute intensities. Hence, future validation measurements on sea ice are necessary. Field measurements of the water surface concurrent to the S-2A overpass allowed a direct comparison of *in situ* data and AC products. Coefficients of determination indicate a strong linear relationship between the mean resampled *in situ* spectrum and ACOLITE, iCOR, and Sen2Cor BOA reflectances, respectively; their spectral slope, however, differs and intensities are one order of magnitude higher. Regarding absolute intensities and slope MAE, Polymer produced the best results, while ATCOR performed poorly over open-water areas. At the time of the S-2A overpass, existing ponds were too small to be included in this study. Future investigations should therefore also address the applicability of AC processors on optically shallow melt pond water.

We further demonstrated the influence of different AC processors on the retrieval of geophysical parameters. Depending on the processor, medians of average reflectances and NDMI for an image subset range from 0.80 to 0.97, and 0.12 to 0.18, respectively. Medians of average reflectance and NDMI are 0.75 and 0.06, respectively. We expect the impact on models that rely on absolute intensities instead of ratios to be even higher. In our study, the retrieval of AOT was critical. The absence of surface types such as dense dark vegetation (which are relevant for image-based retrieval of atmospheric parameters such as AOT) turned out as a general issue for all processors. ATCOR, Sen2Cor, and iCOR failed to retrieve aerosol information from the image, AOT estimated by the new ACOLITE dark spectrum fitting algorithm, however, was in the margin of uncertainty of the AERONET data. Sensitivity analyses with ATCOR and Sen2Cor, however, indicate that AOT, i.e., visibility, is not a limiting factor regarding bright ice surface BOA reflectance. Apparently, the influence of AOT on the spectral shape is negligible if some threshold ($\leq$ 65 km) is exceeded. Image-based retrieval of WV by ATCOR and Sen2Cor and sun photometer data also discorded. With lacking sun photometer data, information about total columnar WV and ozone for processor parameterization, we therefore recommend using predefined aerosol models over ice; nevertheless, we strongly underline the need for image-based retrievals for scenes only containing Arctic sea ice. We further encourage the implementation of an Arctic Background aerosol model (Tomasi et al., 2007) as done by Zege et al. (2015) into existing processors. Until then, the integration of ancillary data might improve BOA retrieval. Yet, further tests are necessary to estimate the quality and availability of ancillary data in the Arctic.

Our study showed that AOT has a large impact on optically deep water. Since Polymer is independent from AOT and aerosol type estimation and insensitive to adjacency effects, it shows a huge potential for the Arctic Ocean. Further field studies, however, should be carried out to explore its capabilities, e.g., for the detection of algae blooms; and extrapolation of the atmospheric signal to adjacent ice floes may also enable AC of ice and snow surfaces. Similarly to Bélanger et al. (2007) and Huck et al. (2007), a sensitivity analysis based on forward modeling of atmospheric transfer to generate S-2A like TOA signals from *in situ* measurements may also support the improvement of existing processors.

Acknowledgements

We acknowledge the support of captain Wunderlich, the crew and the chief scientists Andreas Macke and Hauke Flores of RV *Polarstern* cruise AWI_PS106_00. We want to thank Peter Gege, Gerit Birnbaum and Niels Fuchs for their contributions to the field measurements. We are grateful to Marcel Nicolaus and the AWI Sea Ice Physics team for providing stationary GPS measurements on the floe and Rüdiger Röttgers from Helmholtz-Zentrum Geesthacht for helping with the analysis of optical water properties. We also thank François Steinmetz from HYGEOS for providing Polymer data, Quinten Vanhellemont from RBINS for his help with ACOLITE, Sindy Sterckx from VITO for her explanations regarding iCOR and Sebastian Riedel for his support regarding AOT data. We acknowledge the efforts of the AERONET-MAN and the colleagues from TROPOS for the sun photometer measurements and thank ESA for providing Sentinel-2 data. We further thank Marco Zanatta and the AC^3 project for providing IceCube data and three reviewers for their thorough examination and helpful comments. MH was partly funded by the EnMAP scientific preparation program (FKZ: 50EE1718). We acknowledge financial support by Land Schleswig-Holstein within the funding programme Open Access Publikationsfonds.

Chapter 5

Synthesis

Inconsistencies between different sea ice and climate models and limited forecast capabilities indicate that certain sea ice processes are not yet understood, calling for further observations. Field observations on the Arctic sea ice are spatially and temporally limited and, thus, only portray a limited portion of the regional and inter-annual variability. Remote sensing is the only technique that enables regular, intercomparable observations on large spatial scales, which may serve for model calibration and validation. Melt pond observations by means of remote sensing imagery were previously limited to melt pond fraction, distribution or two-dimensional morphology. A comprehensive understanding of the spatio-temporal evolution of melt ponds on Arctic sea ice, however, also requires information about pond depth, which is an important parameter in the treatment of radiative transfer in sea ice models.

The main goal of the thesis therefore was to develop a methodology for accurately deriving the depth of melt ponds on Arctic sea ice from passive optical measurements that is potentially scalable to air- and spaceborne systems. This goal was reached by achieving the three research objectives itemized in Section 1.4. The foundation of this work is an exceptionally comprehensive melt pond data set including field measurements, hyperspectral airborne imagery and Sentinel-2 satellite data acquired on RV *Polarstern* cruise PS106 in summer 2017.

Firstly, a new method to derive melt pond depth from field-based hyperspectral reflectance data was developed. We used an analytical model to simulate the way meltwater changes the spectral reflectance of bare ice. In the process, we addressed a range of pond bottom optical properties, water depths and solar elevations. Using the simulated data, we developed a model based on the slope of the log-scaled remote sensing reflectance at 710 nm as a function of depth, and sun zenith angle. This new model is particularly convenient for estimating pond depth by means of passive optical remote sensing because it is largely independent from the optical properties of the pond bottom and accounts for the influence of varying solar elevation. We validated the model on independent melt pond field data from dark and bright ponds and were able to retrieve pond depth with a previously unprecedented accuracy of less than 3 cm (König and Oppelt, 2020).

Secondly, we mapped melt pond bathymetry by successfully applying the new method to hyperspectral airborne melt pond imagery, likewise acquired on PS106. Chapter 2 represents the first analysis of airborne hyperspectral imagery of Arctic sea ice. Because the method rests upon reflectance data acquired at the bottom of atmosphere (BOA), it is essential to correct remotely sensed data for effects of atmospheric scattering and absorption, which modulate the electromagnetic radiation on its transfer through the atmosphere. This was achieved by calibrating the remote sensing data on the well-known bottom of atmosphere reflectance of reference image features. Subsequently, the atmospherically corrected imagery enabled accurately mapping melt pond bathymetry by pixel-wise application of the newly developed method (König et al., 2020b).

Because precise atmospheric correction (AC) is an important prerequisite for accurately deriving bottom of atmosphere reflectance, we thirdly evaluated the performances of five AC algorithms using the example of Sentinel-2 satellite imagery. This was achieved by comparing outputs of the algorithms to on-site reflectance measurements of snow/ice and deep ocean water acquired during PS106, intercomparison of algorithm outputs, and comparison to top of atmosphere reflectance. Chapter 4 is the first performance evaluation of AC algorithms in the Arctic sea ice environment (König et al., 2019).

The following paragraphs summarize and discuss the main results, and present options for future investigations and developments.

5.1 Main Achievements

5.1.1 A Linear Model to Derive Melt Pond Depth

> **Research objective 1:** Development of a method to accurately derive the depth of melt ponds on Arctic sea ice from optical data.

Chapter 2 describes the successful development and validation of a robust new method to estimate the depth of melt ponds on Arctic sea ice from optical data with unprecedented accuracy compared to previous approaches.

The model rests upon the log-scaled remote sensing reflectance at 710 nm as a function of depth depending on sun zenith angle. It is based on simulated melt pond spectra covering a wide range of optical properties of the pond bottom ice, pond depths and sun zenith angles. Model testing on independent field data from three different ponds including dark and bright bottoms resulted in good agreement between measured and retrieved pond depth indicating that the newly developed method allows an accurate retrieval of melt pond depth from spectral field measurements.

Deriving the depth of a water body from optical measurements requires knowledge about the apparent optical properties (AOPs) of its bottom. Melt pond bottom AOPs are defined by the ambient light field, and the specific inherent optical properties (IOPs) and thickness of the underlying ice. These parameters may differ on small spatial scales and are temporally variable, which poses a formidable challenge for accurately deriving melt pond depth from optical measurements. Because bottom ice AOPs are usually unknown, we were aiming to minimize their influence on the newly developed method to derive water depth. The good agreement of measured and estimated pond depth in melt ponds with bright and dark bottoms indicates that the new model is largely independent of bottom AOPs.

In agreement with Lu et al. (2016), Malinka et al. (2018), Podgorny and Grenfell (1996) and based on the analysis of pond water samples, we assumed that influences of absorbing or scattering contaminants in the pond water are negligible. Observations of an algae bloom in a closed melt pond (Lin et al., 2016), however, indicate that melt pond water AOPs may be more complex and possibly require more attention in the context of the changing Arctic. Testing the new model on corresponding field data or simulated spectra may help to assess the method's vulnerability to the presence of optically active water constituents.

Remaining uncertainties between measured and estimated pond depths may be attributed to the measurement design, influences of reflections at the water surface, or bare ice field spectra used for model development. Comparing data from different measurement techniques is complicated by the experimental framework conditions. Hitting the same spot with two different instruments is challenging and small scale pond bottom variability may easily introduce considerable errors given shallow depths. Respective uncertainties may be reduced by installation of cord systems at pond sites or upgrading measurement setups with laser pointers for position determination. In addition, measurement repetitions may help estimating uncertainties in future surveys. Due to uncertainties regarding the parameterization of reflections at the water surface, associated effects were not considered during model development. Considering the influences of skyglint and possible reflections of the spectrometer housing at the water surface may presumably result in further improvement. Uncertainties may further be attributed to the bare ice field spectrum used during model development. Future investigations need to assess the influence of sun zenith angle on the reflectance of bare ice measured at nadir. The new method presented in Chapter 2 has been developed for clear sky measurements, because it should potentially be transferable to optical satellite data. Tests on field data acquired under cloud cover indicate that the model is not appropriate for diffuse illumination conditions, which we attribute to the considerable influence of cloud reflections at the water surface and differences in the optical path length of incoming light. The majority of field and airborne melt pond observations, however, is acquired under diffuse overcast conditions. Future research should, therefore, focus on advancing the proposed method to harness the large amount of optical melt pond data acquired under overcast conditions during PS106.

Although results indicate that the newly developed method is capable to accurately derive melt pond depth from reflectance data in bright and dark melt ponds, test data originated from only three different ponds on the same sea ice floe. The model is calibrated on pond depths between 0 and 100 cm and sun zenith angles between 0 and 90°. Test data, however, only covered the depth range between 6 and 25 cm with an average of 17.60 cm and spectral measurements were acquired on a single day under similar illumination conditions and corresponding solar zenith angles between 58.9 and 61°. Consequently, the test data only represent a limited portion of the natural variability of melt pond AOPs. We, therefore, emphasize that more testing is required to investigate the model's applicability to a larger variety of melt pond AOPs.

5.1.2 Mapping Melt Pond Bathymetry Using Hyperspectral Imagery

> **Research objective 2:** Scaling of the new method to airborne imaging sensors to map melt pond bathymetry.

In Chapter 2, we tested the new method on single melt pond spectra and corresponding pond depths. Chapter 3 subsequently describes the scaling of the method to airborne hyperspectral imagery. Results illustrate that accurate mapping of melt pond bathymetry on Arctic sea ice is possible by means of airborne remote sensing subject to accurate atmospheric correction. This study represents the first description of processing and analysis of airborne hyperspectral imagery of Arctic sea ice.

The accurate retrieval of reflectance at the bottom of atmosphere (BOA) from remotely sensed radiances requires atmospheric correction (AC). We evaluated the performance of two AC approaches: empirical line calibration and ATCOR-4, which is a widely used physics-based AC algorithm for hyperspectral airborne imagery.

Empirical line calibration requires spectral information of surface features present in the imagery to estimate apparent optical properties of the atmosphere on site. We used the known reflectances of a black artificial target and a bright ice surface located in the imagery. AC performance was evaluated by comparing four melt pond field spectra to image pixels at the corresponding measurement locations. Resulting BOA spectra are smoothly shaped and widely match ground truth field spectra. Slight overestimation of BOA reflectance in the blue-green wavelength region may be attributed to reflections at the water surface, adjacency effects, or sensor calibration issues. Other than that, uncertainties regarding the spectra used for the empirical line calibration, e.g., resulting from different illumination conditions between acquisitions, may have contributed to the disparities.

ATCOR-4 does not require field spectra for calibration. Instead, AC relies on image-based estimation of atmospheric parameters and pre-computed look up tables (LUTs) of specific aerosol and water vapor AOPs. Yet, many features of the ATCOR workflow were unavailable due to environmental conditions and flight altitude or resulted in misassessments of the actual environmental situation. Estimation of atmospheric AOPs relies on a basic scene classification and the presence of features of known reflectance behavior. Classification results, however, were incorrect and the image did not feature appropriate reference surfaces. The workflow was further challenged by the low flight altitude exceeding the lower limit represented in the LUTs. Consequently, estimated water vapor and AOT did not match sun photometer measurements. Resulting BOA reflectances likewise were compared to melt pond field spectra and, in addition, to the spectra of the dark and bright targets used for the empirical line calibration. Despite the described complications, resulting BOA spectra roughly matched the shape of ground truth spectra but surface reflectances were overestimated by ~ 0.1 and exhibited unusual spectral features. Results indicate that basic assumptions for image-based estimations of atmospheric AOPs are violated in the Arctic sea ice environment. We further assume that atmospheric AOPs described in the pre-processed LUTs do not well represent the Arctic atmosphere characteristics present at site.

We then applied the model described in Chapter 2 to the processed remote sensing images. However, pond depths retrieved from ATCOR outputs were out of scope and only results of the empirical line calibration allowed accurately mapping melt pond bathymetry. Discrepancies between measured and modeled pond depth may be attributed to the described differences between field and pixel spectra. After offset correction, performance was similar to results of the field data experiment in Chapter 2 and melt pond bathymetries were in good agreement with field observations. Results confirm that the new method is largely independent from pond bottom AOPs. This is particularly supported by the results at Pond 1, which was split into a bright and a dark half (Figure 5.1). Note that field spectra from Pond 1 could not be integrated into Chapter 2 due to cloud cover at the time of the survey. Yet, results likewise indicate that the new method described in Chapter 2 requires accurate BOA spectra as input.

Unfortunately, empirical line calibration is impractical for regular observations on large spatial scales. Installation of spectral targets on the ice or simultaneous acquisition of ground truth spectra is logistically challenging and the method relies on the assumption of constant atmospheric AOPs throughout the imagery. This assumption is increasingly challenged with increasing distance to spectral reference targets, and does not address changes in flight altitude. An alternative would be to exploit pseudo-invariant features but appropriate surfaces are seldom available on Arctic sea ice. Consequently, regular melt pond observations on large spatial scales require improved physics-based AC of airborne remote sensing data of Arctic sea ice. This may be achieved by developing image-based estimations and generating LUTs customized for the Arctic sea ice environment. Consid-

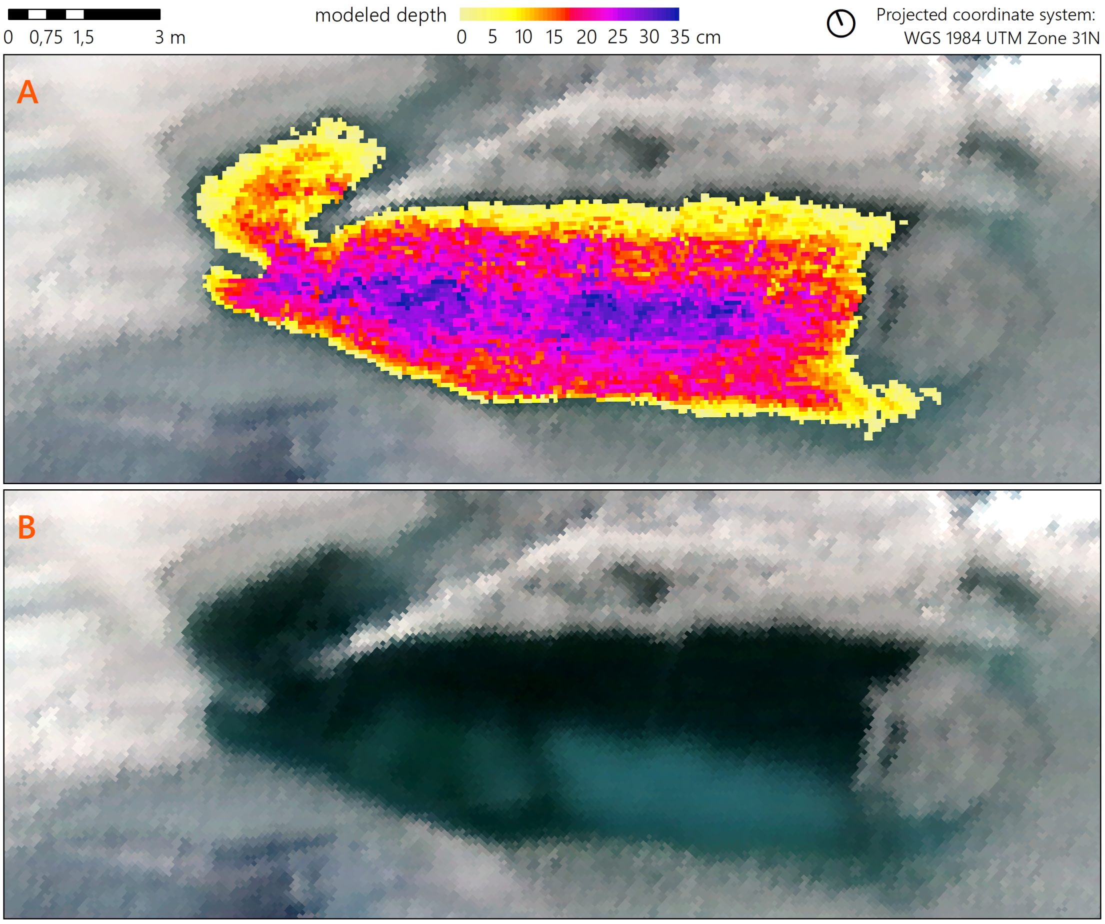

Figure 5.1: Comparison of pond depth retrieved with the new model (A) and true color RGB image (B) of Pond 1.

ering the technical development in the field of UAVs it may be worth investigating the need to extend LUTs to flight altitudes below 0.1 km. In addition, we recommend characterizing sensor behavior under operation conditions, vicarious sensor calibration and extending setups with downwelling irradiance sensors to account for illumination changes and to compute at-sensor remote sensing reflectance.

A major challenge for the comparison of measured and modeled pond depth was the accurate localization of field measurements in the very high spatial resolution imagery. Complications resulted from low accuracy of GPS positioning and constant drift of the ice floe. Considering that pond depth can be highly variable on small spatial scales, these uncertainties may result in large errors when comparing measured and estimated pond depths. We minimized spatial uncertainties by thoroughly analyzing survey protocols and field photographs from multiple cameras, and manual co-registration of hyperspectral imagery with ultra-high resolution airborne photographs. Located measurement points were then buffered with radii corresponding to estimated remaining spatial uncertainties to assess per-buffer spatial variability and compute average depth for comparison. This procedure, however, influences assessing pond depth retrieval by means of performance metrics. We therefore extended the analysis by a qualitative assessment. The described complications point to the need for high accuracy, drift-invariant positioning systems for sea ice research, e.g., by means of ultra-wideband positioning or optical triangulation. In addition, increasing both the number of measurement locations and the number of measurements per location may improve estimating uncertainties. In sufficiently deep ponds this may be achieved by sonar equipped unmanned surface vehicles subject to accurate positioning. Other than that, effects of sea ice drift on progressive scanner imagery may be worth investigating.

AC including image-based estimates of atmospheric AOPs may facilitate exploitation of hyperspectral airborne imagery of Arctic sea ice for monitoring melt pond bathymetry on regional scales. Prior to that, we highly recommend the deployment of spectral targets and acquisition of ground truth field data concurrent to hyperspectral image acquisitions.

5.1.3 Performance Evaluation of Atmospheric Correction Approaches for Sentinel-2 Over Arctic Sea Ice

> **Research objective 3:** Suitability assessment of existing atmospheric correction approaches for optical satellite imagery for deriving bottom of atmosphere reflectance of Arctic sea ice.

In Chapter 3, we showed that the new method described in Chapter 2 enables reliable estimation of melt pond bathymetry from hyperspectral remote sensing imagery subject to accurate AC. Although satellite remote sensing today is the main tool for observations of Arctic sea ice, sea ice surface classifications and estimates of melt pond fraction, little effort has been made to assess the influence of AC on the accuracy of remote sensing products. Chapter 4 represents the first evaluation of atmospheric correction approaches for satellite imagery of Arctic sea ice. We compared five different AC algorithms for Sentinel-2 (ACOLITE, ATCOR, iCOR, Polymer, and Sen2Cor) and evaluated their performance by comparing estimated BOA spectra to resampled ground truth spectra acquired on PS106. The present results question the suitability of existing AC processors for the Arctic sea ice environment, which is a problem for the derivation of geophysical parameters at this point.

Most image-based retrievals of atmospheric parameters (aerosol type, aerosol optical thickness (AOT), water vapor) failed due to the absence of adequate reference surfaces (e.g., dense dark vegetation, bare soil) in the Arctic sea ice environment. Only ACOLITE-estimated AOT was within the uncertainty range of atmospheric measurements, indicating that the dark spectrum fitting approach may potentially be suitable to estimate AOT in the Arctic sea ice environment in the presence of dark ocean pixels. Yet, more case studies are required to investigate its suitability for sea ice imagery. In addition, alternative methods to estimate atmospheric parameters from imagery that specifically address the spectral characteristics of the sea ice environment are desirable. Alternatively, atmospheric parameters may be derived from auxiliary data.

Manual parameterization based on field data improved AC but results suggest that atmospheric AOPs present at site are not well-represented by the respective LUTs used in the applied processors. Intercomparison of AC algorithm outputs, top of atmosphere reflectance and resampled field spectra illustrates that atmospheric correction with the ACOLITE, ATCOR and iCOR algorithms improved the shape of white ice and snow spectra. For open water pixels, BOA reflectance estimated by the Polymer algorithm resembled *in situ* spectra most accurately. Results indicate that the choice of algorithm impacts shape and intensity of spectra with corresponding influences on the derivation of geophysical parameters from remote sensing imagery.

For white ice and snow surfaces we performed measurement surveys five, three and one day prior to and five days after the satellite overpass. Field measurements were mostly performed under diffuse illumination conditions with the solar disk visible or under variable illumination conditions and melt has occurred within the eleven days period with likely influences on the optical properties of white ice and snow. This setup is far from ideal and prevented evaluating AC by comparing absolute intensities as done in the previous chapter. Assuming that changes introduced by melt processes and changing illumination conditions do not show wavelength-dependent behavior, we evaluated algorithm outputs in terms of spectral shapes instead. While we believe that this approach is more appropriate than comparing intensities, conclusive evaluation of AC performance in terms of spectral intensities warrants quasi-simultaneous acquisition of ground truth data. Unfortunately, melt ponds sampled during satellite transit were smaller than the spatial resolution of Sentinel-2 bands, which prevented evaluating the suitability of the selected AC algorithms for melt ponds on Arctic sea ice.

Different setting options, aerosol types and LUTs of the applied algorithms complicated the comparison. Future investigations should, therefore, focus on the relative impact of single parameters. Preliminary sensitivity studies suggest that the influence of visibility is negligible after some threshold is exceeded, while the choice of aerosol type is more important for AC in the Arctic sea ice environment.

Comparing field spectroscopy and Sentinel-2 satellite imagery is aggravated by the large pixel size compared to the footprint of a handheld spectrometer and spatial uncertainties regarding the location of field measurements in the satellite image. However, numerous field measurements were conducted to cover the spatial and spectral variability present at site, and both are considered to be small, indicated by the average standard deviation of less than 5-7 % in each band of the resampled field data. GPS positions were corrected for sea ice drift but low spatial accuracy of GPS positioning in the Arctic sea ice exacerbates accurate localization of measurements in the imagery. Yet, inaccuracies are believed to be small compared to the pixel size of Sentinel-2 imagery and small standard deviations of less than 3 % in each band of the remote sensing data indicate little spectral variability within the region of interests.

Findings from Chapters 3 and 4 show that efforts should focus on the development of a robust atmospheric correction procedure that addresses the special environmental and atmospheric conditions of the Arctic sea ice environment. A robust atmospheric correction is the principal requirement for an accurate retrieval of melt pond depth from remote sensing imagery by means of the newly developed method.

5.2 Outlook

Results of this dissertation indicate that the newly developed method based on the slope of the log-scaled remote sensing reflectance at 710 nm enables calculating melt pond depth from passive optical data with unprecedented accuracy. We showed that the method is scalable to remotely sensed imagery to map melt pond bathymetry but critically depends on accurate preprocessing of the data. The findings presented may serve as a first step towards a regular operational large-scale monitoring of melt pond depth by means of air- and spaceborne remote sensing, which will enhance our understanding of the spatio-temporal evolution of melt ponds on Arctic sea ice and improve predictions of sea ice and climate models.

More field observations covering a larger variety of sea ice and atmospheric conditions may help to further assess and to improve the newly developed method to estimate pond depth. We made suggestions for improvements which were partly implemented on the MOSAiC expedition. Considering future ice work, best practices for melt pond observations should be discussed in the sea ice community. New approaches for localization and spatio-temporal synchronization of measurements need to be engineered. In view of the strong spatio-temporal limitations of field measurements on Arctic sea ice, cooperation across disciplines and more holistic sampling protocols may partially compensate for logistical restrictions and increase the amount of comparable data with benefits for the entire sea ice community.

Limitations of existing atmospheric correction algorithms over Arctic sea ice may be addressed through the integration of Arctic-specific aerosol models (e.g., Tomasi et al., 2007, 2012) and image-based retrievals of atmospheric parameters may be optimized for the Arctic sea ice environment. The high spatio-temporal variability of the sea ice surface does not feature pseudo-invariant targets but our findings indicate that open water surfaces may serve as potential candidates for image-based retrievals of atmospheric parameters, and extrapolation to adjacent areas may improve atmospheric correction over sea ice floes. Alternatively, sea ice radiative transfer models (e.g., Zege et al., 2015; Malinka et al., 2016, 2018) may be coupled with atmospheric radiative transfer models (e.g., MODTRAN, 6SV, SOS) to compute extensive LUTs, which may be used to train neural networks for inversion (compare Hieronymi et al., 2017).

An alternative approach to evaluate atmospheric correction may be comparing the atmospherically corrected Sentinel-2 satellite data presented in Chapter 4 to the atmospherically corrected airborne imagery presented in Chapter 3. This approach has two virtues: (1) airborne and satellite data were recorded on the same day only two hours apart; and (2) pixel by pixel comparisons include the spatial variability at site. Additional flight stripes recorded on the same day in different altitudes may further assist spatial scaling of pixel values for comparison. This approach requires spatial co-registration of airborne and satellite data. An appropriate methodology for ice drift correction based on image features has already been developed. Preliminary results are promising (Figure 5.2) but a quantitative evaluation is still pending. In addition, it may be worth estimating the limits of commonly used plane-parallel atmospheric correction approaches regarding high sun zenith angles and investigating alternative representations that address the Earth's curvature.

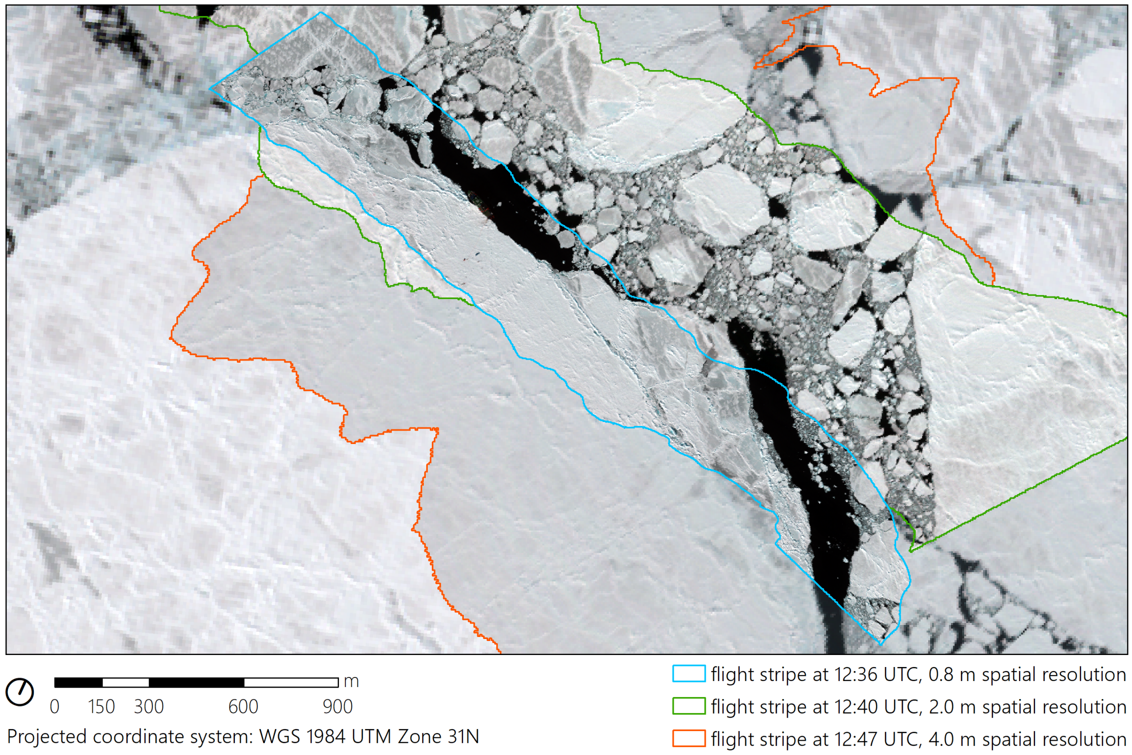

Figure 5.2: Co-registration of three AisaEAGLE flight stripes acquired at different times and altitudes and S-2A imagery (10 m spatial resolution) acquired at 14:58:01 UTC (background). All data are stretched pseudo-true color RGB representations.

Technical developments in the fields of airborne and satellite remote sensing, multi-sensor data fusion and combination with auxiliary data may open possibilities to improve monitoring of melt ponds on Arctic sea ice by means of remote sensing.

In contrast to true color RGB imagery, which is frequently used for airborne observations of melt ponds, the high spectral resolution of hyperspectral sensors increases the amount of information per pixel, opening new possibilities to derive geophysical sea ice information such as melt pond bathymetry from imagery. Disadvantages are increased technical effort, e.g., regarding sensor calibration and atmospheric correction, and comparably high cost. Recent advances in the field of unmanned aerial vehicles and the development of small and lightweight hyperspectral imaging sensors (e.g., Zhong et al., 2018), however, lower the impediments for local and regional sea ice observations with high spectral resolution. Flexibility of airborne sensors in terms of flight patterns and viewing geometry may enable studying reflection distribution geometries of sea ice features. Survey flights with aircraft carrying multiple instruments (e.g., hyperspectral imaging, FODIS and LiDAR sensors) may improve the estimation of geophysical sea ice parameters from imagery on local and regional scales. Consecutive survey flights in different altitudes may be used to bridge spatial scales from field-based to airborne and satellite remote sensing observations, and synchronized observations with satellite overpasses may help improving satellite remote sensing products.

The potential of a satellite sensor to map melt pond depth is defined by its spectral, spatial and radiometric resolution, and signal-to-noise ratio. An operational monitoring of the seasonal evolution of melt ponds on large spatial scales is restricted by a mission's temporal resolution and spatial coverage.

Passive optical satellite missions with moderate spatial resolution (e.g., MODIS) enable regular Arctic-wide observations but their coarse spatial resolution of hundreds of meters prohibits monitoring individual ponds. Existing approaches to map melt pond fraction by pixel-wise unmixing suffer from ambiguities of different surface type mixtures (Wright and Polashenski, 2020). Pond depth may feature a considerable variability on subpixel scale, thus, introducing additional complexity, which presumably prevents estimating pond depth from these data.

Higher spatial resolution multispectral optical satellite missions like Sentinel-2 enable observations of individual sea ice features subject to their spatial dimension. The potential of these missions to be used in sea ice research, however, has been identified only very recently, e.g., for estimating melt pond fraction (Wang et al., 2020) and for the improvement of moderate resolution melt pond fraction products (Wright and Polashenski, 2020), ICESat-2 data interpretation (Farrell et al., 2020; Petty et al., 2021), or ice floe tracking (König et al., 2020a). Although the orbital setups of these missions limit spatial coverage and prohibit Arctic-wide observations, large areas of seasonal and perennial sea ice may be sensed, and wide swaths that overlap at high latitudes enable frequent observations. Contemporary multispectral sensors have improved radiometric resolutions but more research is necessary to assess potential limitations regarding low solar elevations and correspondingly low reflectances over long periods of the year, which may challenge signal-to-noise ratios (compare Gleeson et al., 2010).

The feasibility of these missions to estimate melt pond depth is limited by the number, width and location of spectral bands. The new method to derive melt pond depth from the slope of the log-scaled remote sensing reflectance requires a suitable spectral resolution in the wavelength region around 710 nm. However, the MultiSpectral Instrument (MSI) on the Sentinel-2 satellites features a high number of narrow spectral bands in the far red wavelength region, with bands located at 705 nm and 740 nm, respectively. Future studies should therefore investigate the potential of MSI for estimating melt pond depth, e.g., by spectral resampling of the melt pond LUTs generated in Chapter 2. An alternative worth investigating may be the reconstruction of hyperspectral information from multispectral data as suggested by Banerjee and Shanmugam (2020).

A potentially solvable restriction for mapping sea ice with higher spatial resolution are geographical restrictions of acquisitions to land masses and coastal zones. The high spatial variability in these regions reasons a correspondingly high spatial resolution, while moderate resolution sensors are usually adequate for observations of the open oceans. The ice-covered Arctic Ocean, however, is an exception and the sea ice remote sensing community should therefore emphasize the need for higher spatial resolution sea ice imagery, including off-shore regions of the Arctic Ocean in summer.

Observations with very high spatial resolution multispectral satellite missions such as WorldView increase the number of pure pond pixels. Spectral band settings of contemporary missions presumably exacerbate the estimation of melt pond depth with the newly developed method but it may be worth assessing the potential of these sensors in future studies. An operational monitoring is limited by narrow swaths and small spatial coverage resulting from large data volumes but occasional regional observations are possible. This issue, however, may be solved by increasing the number of instruments. Planet's Dove satellite fleet, for example, counts more than 150 sensors with up to eight spectral bands, which enables complete daily coverage of the Earth's surface (Planet, 2021a,b).

Hyperspectral imaging sensors enable observations with high spectral detail making these sensors particular promising for monitoring melt pond depth by means of the new method. The number of these instruments in space, however, is small mainly due to technical constraints, including challenging SNR, sensor cost, and high data volume (Transon et al., 2017). Consequently, the number of sea ice studies involving hyperspectral satellite imagery is extremely scarce. Yuan et al. (2017) used data from NASA's decommissioned Hyperion sensor to estimate sea ice thickness in the Bohai Sea and Han et al. (2019) carried out a sea ice classification experiment using two data sets from the same sensor from Baffin Bay and Bohai Bay. Gleeson et al. (2010) faced problems regarding Hyperion's signal-to-noise ratio due to low reflectance resulting from low sun elevation in high latitudes.

Today a series of new hyperspectral satellite sensors with potential to support Arctic research and melt pond depth retrieval is already in space or currently under development and soon to be launched. Most sensors offer high spectral resolutions of ~ 10 nm in combination with high spatial resolutions between 30 and 8 m, which facilitates detailed observations of sea ice features from space (Transon et al., 2017, 2018). Some missions are further equipped with panchromatic sensors that may aid sharpening of hyperspectral images (e.g., Loncan et al., 2015). Improved signal-to-noise ratios promise to be useful for observations at low solar elevation. Orbital configurations limit observations of the PRecursore IperSpettrale della Missione Applicativa (PRISMA) and the Space-borne Hyperspectral Applicative Land and Ocean Mission (SHALOM) to seasonal sea ice latitudes below 70° North but the Compact High Resolution Imaging Spectrometer (CHRIS), the Environmental Mapping and Analysis Program (EnMAP), the Hyperspectral InfraRed Imager (HyspIRI) and the Copernicus Hyperspectral Imaging Mission for the Environment (CHIME/Sentinel-10) (will) have increased coverage up to 84° North.

Constraints regarding the usage of hyperspectral spaceborne sensors for regular, large scale sea ice observations are narrow swaths, long revisit times and limitations resulting from high data volume. Swath widths of most sensors are 30 km but HyspIRI will offer a substantially wider swath and increased spatial coverage making it particularly interesting for sea ice observations. Low temporal resolutions up to 27 days (Transon et al., 2018) reduce the chances for cloud-free observations. Some sensors enable changing view zenith angle to increase temporal resolution but associated influences may complicate data processing. Overlapping of swaths in high latitudes theoretically allows multiple observations per day but the huge data volume of hyperspectral imagery strongly restricts average daily coverage (Feingersh and Dor, 2015) and sea ice research competes for acquisitions with other disciplines, which reduces the chances for cloud-free sea ice observations.

A possible solution to overcome limitations of single satellite missions, e.g., regarding spatio-temporal coverage or spectral resolution, is the synergistic use of multiple sensors. For example, the comparable and complementary hyperspectral imaging satellites to be launched in the near future may compensate for a single missions small spatio-temporal coverage in high latitudes if used in synergy. Wright and Polashenski (2020) promote the combination of higher and moderate resolution satellite data to improve estimating MPF. Transon et al. (2018) suggest that pan-sharpening based on Sentinel-2 imagery may alleviate the constraint of revisit time of hyperspectral satellite missions. Ma et al. (2020) showed the potential to use ICESat-2 bathymetric points and Sentinel-2 imagery to fit empirical models for estimating water depth. Buckley et al. (2020) suggest combining LiDAR derived pond depth with digital imagery from Operation IceBridge to assess melt pond volume, and Farrell et al. (2020) and Tilling et al. (2020) used Sentinel-2 imagery in combination with ICESat-2 for melt pond localization. Merging ICESat-2 with higher and very high optical imagery may provide new insights into both the variability of melt pond AOPs and pond depth, and potentially enables comparison of different methods and further development. Other than that, data interpretation and modeling efforts may be improved by combining satellite data with auxiliary information, e.g., on air temperature or sea ice characteristics (e.g., Istomina and Heygster, 2017).

Combining imagery of sea ice from multiple satellite sensors, however, requires a sensor-bridging drift correction. Monitoring of melt pond evolution on individual drifting sea ice floes requires ice floe tracking and co-registration. Radar imagery may help to overcome long periods between subsequent acquisitions with higher resolution passive optical sensors. Methods that identify sea ice floes based on geometrical descriptors (e.g., König et al., 2020a) may serve as a basis for floe tracking and co-registration of imagery from different sensors.

Findings of this dissertation and the long list of opportunities for coming research and development points out the large potential for future advances in sea ice remote sensing, which will further improve our understanding of melt pond evolution on different spatio-temporal scales and how the Arctic sea ice is changing. Observations may be used for the calibration and validation of sea ice, ecosystem and global climate models, which will help predicting future development of Arctic sea ice and associated consequences on a global scale.

Bibliography

Adão, T., Hruška, J., Pádua, L., Bessa, J., Peres, E., Morais, R., and Sousa, J.: Hyperspectral Imaging: A Review on UAV-Based Sensors, Data Processing and Applications for Agriculture and Forestry, Remote Sensing, 9, 1110, https://doi.org/10.3390/rs9111110, 2017.

Albert, A. and Mobley, C.: An analytical model for subsurface irradiance and remote sensing reflectance in deep and shallow case-2 waters, Optics Express, 11, 2873, https://doi.org/10.1364/OE.11.002873, 2003.

Ammari, H. M.: Mission-Oriented Sensor Networks and Systems: Art and Science, vol. 164 of *Studies in Systems, Decision and Control*, Springer International Publishing, Cham, https://doi.org/10.1007/978-3-319-92384-0, 2019.

Andreas, E. L.: Near-surface water vapor over polar sea ice is always near ice saturation, Journal of Geophysical Research, 107, 8033, https://doi.org/10.1029/2000JC000411, 2002.

Arrigo, K. R.: Sea Ice Ecosystems, Annual Review of Marine Science, 6, 439–467, https://doi.org/10.1146/annurev-marine-010213-135103, 2014.

Arrigo, K. R., Perovich, D. K., Pickart, R. S., Brown, Z. W., van Dijken, G. L., Lowry, K. E., Mills, M. M., Palmer, M. A., Balch, W. M., Bahr, F., Bates, N. R., Benitez-Nelson, C., Bowler, B., Brownlee, E., Ehn, J. K., Frey, K. E., Garley, R., Laney, S. R., Lubelczyk, L., Mathis, J., Matsuoka, A., Mitchell, B. G., Moore, G. W. K., Ortega-Retuerta, E., Pal, S., Polashenski, C. M., Reynolds, R. A., Schieber, B., Sosik, H. M., Stephens, M., and Swift, J. H.: Massive Phytoplankton Blooms Under Arctic Sea Ice, Science, 336, 1408–1408, https://doi.org/10.1126/science.1215065, 2012.

Banerjee, S. and Shanmugam, P.: Novel method for reconstruction of hyperspectral resolution images from multispectral data for complex coastal and inland waters, Advances in Space Research, 67, 266–289, https://doi.org/10.1016/j.asr.2020.09.045, 2020.

Barber, D. G. and Yackel, J.: The physical, radiative and microwave scattering characteristics of melt ponds on Arctic landfast sea ice, International Journal of Remote Sensing, 20, 2069–2090, https://doi.org/10.1080/014311699212353, 1999.

Bélanger, S., Ehn, J. K., and Babin, M.: Impact of sea ice on the retrieval of water-leaving reflectance, chlorophyll a concentration and inherent optical properties from satellite ocean color data, Remote Sensing of Environment, 111, 51–68, https://doi.org/10.1016/j.rse.2007.03.013, 2007.

Berk, A., Anderson, G. P., Acharya, P. K., and Shettle, E. P.: MODTRAN 5.2.0.0 User's Manual, 2008.

Bindschadler, R., Vornberger, P., Fleming, A., Fox, A., Mullins, J., Binnie, D., Paulsen, S. J., Granneman, B., and Gorodetzky, D.: The Landsat Image Mosaic of Antarctica, Remote Sensing of Environment, 112, 4214–4226, https://doi.org/10.1016/j.rse.2008.07.006, 2008.

Birnbaum, G., Dierking, W., Hartmann, J., Lüpkes, C., Ehrlich, A., Garbrecht, T., and Sellmann, M.: The Campaign MELTEX with Research Aircraft "POLAR 5" in the Arctic in 2008, Berichte zur Polar- und Meeresforschung/Reports on Polar and Marine Research, 593, 3–85, https://doi.org/hdl:10013/epic.32677, 2009.

Black, M., Fleming, A., Riley, T., Ferrier, G., Fretwell, P., McFee, J., Achal, S., and Diaz, A.: On the Atmospheric Correction of Antarctic Airborne Hyperspectral Data, Remote Sensing, 6, 4498–4514, https://doi.org/10.3390/rs6054498, 2014.

Bliss, A. C. and Anderson, M. R.: Snowmelt onset over Arctic sea ice from passive microwave satellite data: 1979–2012, The Cryosphere, 8, 2089–2100, https://doi.org/10.5194/tc-8-2089-2014, 2014.

Bourgeois, C. S., Calanca, P., and Ohmura, A.: A field study of the hemispherical directional reflectance factor and spectral albedo of dry snow, Journal of Geophysical Research Atmospheres, 111, 1–13, https://doi.org/10.1029/2006JD007296, 2006.

Box, J. E. and Ski, K.: Remote sounding of Greenland supraglacial melt lakes: implications for subglacial hydraulics, Journal of Glaciology, 53, 257–265, https://doi.org/10.3189/172756507782202883, 2007.

Buckley, E. M., Farrell, S. L., Duncan, K., Connor, L. N., Kuhn, J. M., and Dominguez, R. A. T.: Classification of Sea Ice Summer Melt Features in High-Resolution Ice-Bridge Imagery, Journal of Geophysical Research: Oceans, 125, https://doi.org/10.1029/2019JC015738, 2020.

Bulgarelli, B. and Zibordi, G.: On the detectability of adjacency effects in ocean color remote sensing of mid-latitude coastal environments by SeaWiFS, MODIS-A, MERIS, OLCI, OLI and MSI, Remote Sensing of Environment, 209, 423–438, https://doi.org/10.1016/j.rse.2017.12.021, 2018.

Callieco, F. and Dell'Acqua, F.: A comparison between two radiative transfer models for atmospheric correction over a wide range of wavelengths, International Journal of Remote Sensing, 32, 1357–1370, https://doi.org/10.1080/01431160903547999, 2011.

Comiso, J. C.: Large decadal decline of the arctic multiyear ice cover, Journal of Climate, 25, 1176–1193, https://doi.org/10.1175/JCLI-D-11-00113.1, 2012.

Crary, A.: Arctic Ice Island and Ice Shelf Studies: Part I, ARCTIC, 11, 2, https://doi.org/10.14430/arctic3731, 1958.

Curry, J. a., Schramm, J. L., and Ebert, E. E.: Sea Ice-Albedo Climate Feedback Mechanism, Journal of Climate, 8, 240–247, https://doi.org/10.1175/1520-0442(1995)008⟨0240:SIACFM⟩2.0.CO;2, 1995.

Curry, J. A., Schramm, J. L., Perovich, D. K., and Pinto, J. O.: Applications of SHEBA/FIRE data to evaluation of snow/ice albedo parameterizations, Journal of Geophysical Research: Atmospheres, 106, 15 345–15 355, https://doi.org/10.1029/2000JD900311, 2001.

Dai, A., Luo, D., Song, M., and Liu, J.: Arctic amplification is caused by sea-ice loss under increasing CO 2, Nature Communications, 10, 1–13, https://doi.org/10.1038/s41467-018-07954-9, 2019.

De Abreu, R., Yackel, J., Barber, D., and Arkett, M.: Operational Satellite Sensing of Arctic First-Year Sea Ice Melt, Canadian Journal of Remote Sensing, 27, 487–501, https://doi.org/10.1080/07038992.2001.10854889, 2001.

De Keukelaere, L., Sterckx, S., Adriaensen, S., Knaeps, E., Reusen, I., Giardino, C., Bresciani, M., Hunter, P., Neil, C., Van der Zande, D., and Vaiciute, D.: Atmospheric correction of Landsat-8/OLI and Sentinel-2/MSI data using iCOR algorithm: validation for coastal and inland waters, European Journal of Remote Sensing, 51, 525–542, https://doi.org/10.1080/22797254.2018.1457937, 2018.

Derksen, C., Piwowar, J., and LeDrew, E.: Sea-Ice Melt-Pond Fraction as Determined from Low Level Aerial Photographs, Arctic and Alpine Research, 29, 345, https://doi.org/10.2307/1552150, 1997.

Ding, Y., Cheng, X., Liu, J., Hui, F., Wang, Z., and Chen, S.: Retrieval of melt pond fraction over Arctic sea ice during 2000-2019 using an ensemble-based deep neural network, Remote Sensing, 12, 6–8, https://doi.org/10.3390/RS12172746, 2020.

Divine, D. V., Granskog, M. A., Hudson, S. R., Pedersen, C. A., Karlsen, T. I., Divina, S. A., Renner, A. H. H., and Gerland, S.: Regional melt-pond fraction and albedo of thin Arctic first-year drift ice in late summer, The Cryosphere, 9, 255–268, https://doi.org/10.5194/tc-9-255-2015, 2015.

Divine, D. V., Pedersen, C. A., Karlsen, T. I., Aas, H. F., A. Granskog, M., R. Hudson, S., and Gerland, S.: Photogrammetric retrieval and analysis of small scale sea ice topography during summer melt, Cold Regions Science and Technology, 129, 77–84, https://doi.org/10.1016/j.coldregions.2016.06.006, 2016.

Donlon, C., Berruti, B., Buongiorno, A., Ferreira, M. H., Féménias, P., Frerick, J., Goryl, P., Klein, U., Laur, H., Mavrocordatos, C., Nieke, J., Rebhan, H., Seitz, B., Stroede, J., and Sciarra, R.: The Global Monitoring for Environment and Security (GMES) Sentinel-3 mission, Remote Sensing of Environment, 120, 37–57, https://doi.org/10.1016/j.rse.2011.07.024, 2012.

Dörnhöfer, K. and Oppelt, N.: Remote sensing for lake research and monitoring - Recent advances, Ecological Indicators, 64, 105–122, https://doi.org/10.1016/j.ecolind.2015.12.009, 2016.

Dörnhöfer, K., Göritz, A., Gege, P., Pflug, B., and Oppelt, N.: Water Constituents and Water Depth Retrieval from Sentinel-2A—A First Evaluation in an Oligotrophic Lake, Remote Sensing, 8, 941, https://doi.org/10.3390/rs8110941, 2016.

Doxani, G., Vermote, E., Roger, J.-c., Gascon, F., Adriaensen, S., Frantz, D., Hagolle, O., Hollstein, A., and Kirches, G.: Atmospheric Correction Inter-Comparison Exercise, Remote Sensing, 10, 1–18, https://doi.org/10.3390/rs10020352, 2018.

Ebert, E. E. and Curry, J. A.: An intermediate one-dimensional thermodynamic sea ice model for investigating ice-atmosphere interactions, Journal of Geophysical Research, 98, https://doi.org/10.1029/93jc00656, 1993.

Ebert, E. E., Schramm, J. L., and Curry, J. A.: Disposition of solar radiation in sea ice and the upper ocean, Journal of Geophysical Research, 100, https://doi.org/10.1029/95jc01672, 1995.

Ehn, J. K., Mundy, C. J., Barber, D. G., Hop, H., Rossnagel, A., and Stewart, J.: Impact of horizontal spreading on light propagation in melt pond covered seasonal sea ice in the Canadian Arctic, Journal of Geophysical Research, 116, C00G02, https://doi.org/10.1029/2010JC006908, 2011.

Eicken, H.: Structure of under-ice melt ponds in the central Arctic and their effect on, the sea-ice cover, Limnology and Oceanography, 39, 682–693, https://doi.org/10.4319/lo.1994.39.3.0682, 1994.

Eicken, H.: Tracer studies of pathways and rates of meltwater transport through Arctic summer sea ice, Journal of Geophysical Research, 107, 8046, https://doi.org/10.1029/2000JC000583, 2002.

Eicken, H., Grenfell, T. C., Perovich, D. K., Richter-Menge, J. A., and Frey, K.: Hydraulic controls of summer Arctic pack ice albedo, Journal of Geophysical Research: Oceans, 109, n/a–n/a, https://doi.org/10.1029/2003JC001989, 2004.

El Naggar, S., Garrity, C., and Ramseier, R. O.: The modelling of sea ice melt-water ponds for the High Arctic using an Airborne line scan camera, and applied to the Satellite Special Sensor Microwave/Imager (SSM/I), International Journal of Remote Sensing, 19, 2373–2394, https://doi.org/10.1080/014311698214785, 1998.

European Space Agency: Sentinel-2 User Handbook, 2015.

European Space Agency: Resolution and Swath, URL `https://sentinel.esa.int/web/sentinel/missions/sentinel-2/instrument-payload/resolution-and-swath`, [Date accessed: 2018-05-28], 2018a.

European Space Agency: Revisit and Coverage, URL `https://sentinel.esa.int/web/sentinel/user-guides/sentinel-2-msi/revisit-coverage`, [Date accessed: 2018-11-01], 2018b.

European Space Agency: Sentinel-2 Spectral Response Functions (S2-SRF), URL `https://earth.esa.int/web/sentinel/user-guides/sentinel-2-msi/document-library/-/asset_publisher/Wk0TKajiISaR/content/sentinel-2a-spectral-responses`, [Date accessed: 2018-05-03], 2018c.

Fair, Z., Flanner, M., Brunt, K., Fricker, H. A., and Gardner, A.: Using ICESat-2 and Operation IceBridge altimetry for supraglacial lake depth retrievals, The Cryosphere Discussions, pp. 1–21, https://doi.org/10.5194/tc-2020-136, 2020.

Farrell, S. L., Duncan, K., Buckley, E. M., Richter-Menge, J., and Li, R.: Mapping Sea Ice Surface Topography in High Fidelity with ICESat-2, Geophysical Research Letters, https://doi.org/10.1029/2020GL090708, 2020.

Feingersh, T. and Dor, E. B.: SHALOM - A Commercial Hyperspectral Space Mission, in: Optical Payloads for Space Missions, pp. 247–263, John Wiley & Sons, Ltd, Chichester, UK, https://doi.org/10.1002/9781118945179.ch11, 2015.

Fetterer, F. and Untersteiner, N.: Observations of melt ponds on Arctic sea ice, Journal of Geophysical Research: Oceans, 103, 24 821–24 835, https://doi.org/10.1029/98JC02034, 1998.

Flato, G. M. and Brown, R. D.: Variability and climate sensitivity of landfast Arctic sea ice, Journal of Geophysical Research: Oceans, 101, 25 767–25 777, https://doi.org/10.1029/96JC02431, 1996.

Flocco, D. and Feltham, D. L.: A continuum model of melt pond evolution on Arctic sea ice, Journal of Geophysical Research, 112, C08 016, https://doi.org/10.1029/2006JC003836, 2007.

Flocco, D., Feltham, D. L., and Turner, A. K.: Incorporation of a physically based melt pond scheme into the sea ice component of a climate model, Journal of Geophysical Research, 115, C08 012, https://doi.org/10.1029/2009JC005568, 2010.

Flocco, D., Schroeder, D., Feltham, D. L., and Hunke, E. C.: Impact of melt ponds on Arctic sea ice simulations from 1990 to 2007, Journal of Geophysical Research: Oceans, 117, n/a–n/a, https://doi.org/10.1029/2012JC008195, 2012.

Flocco, D., Feltham, D. L., Bailey, E., and Schroeder, D.: The refreezing of melt ponds on Arctic sea ice, Journal of Geophysical Research: Oceans, 120, 647–659, https://doi.org/10.1002/2014JC010140, 2015.

Frey, K. E., Perovich, D. K., and Light, B.: The spatial distribution of solar radiation under a melting Arctic sea ice cover, Geophysical Research Letters, 38, n/a–n/a, https://doi.org/10.1029/2011GL049421, 2011.

Gaffey, C. and Bhardwaj, A.: Applications of Unmanned Aerial Vehicles in Cryosphere: Latest Advances and Prospects, Remote Sensing, 12, 948, https://doi.org/10.3390/rs12060948, 2020.

Gao, J.: Bathymetric mapping by means of remote sensing: Methods, accuracy and limitations, Progress in Physical Geography, 33, 103–116, https://doi.org/10.1177/0309133309105657, 2009.

Gege, P.: The water color simulator WASI: an integrating software tool for analysis and simulation of optical in situ spectra, Computers & Geosciences, 30, 523–532, https://doi.org/10.1016/j.cageo.2004.03.005, 2004.

Gege, P.: WASI-2D: A software tool for regionally optimized analysis of imaging spectrometer data from deep and shallow waters, Computers & Geosciences, 62, 208–215, https://doi.org/10.1016/j.cageo.2013.07.022, 2014.

Gege, P.: The Water Colour Simulator WASI User manual for WASI version 4.1, Tech. rep., 2015.

Gege, P. and Albert, A.: A Tool for Inverse Modeling of Spectral Measurements in Deep and Shallow Waters, in: Remote Sensing of Aquatic Coastal Ecosystem Processes - Science and Management Applications, edited by Richardson, L. L. and LeDrew, E. F., chap. 4, pp. 81–109, Springer, 2006.

Gege, P. and König, M.: HCRF measurements (Ibsen Freedom VIS FSV-305) of bare Arctic sea ice acquired during POLARSTERN cruise PS106/2, https://doi.org/doi.pangaea.de/10.1594/PANGAEA.908073, 2019.

Gege, P., König, M., and Oppelt, N.: Reflectance measurements (Ocean Optics STS-VIS) of bare ice and melt ponds on Arctic sea ice acquired during POLARSTERN cruise PS106/1, https://doi.org/doi.pangaea.de/10.1594/PANGAEA.908074, 2019.

Georgiou, S., Shepherd, A., McMillan, M., and Nienow, P.: Seasonal evolution of supraglacial lake volume from ASTER imagery, Annals of Glaciology, 50, 95–100, https://doi.org/10.3189/172756409789624328, 2009.

Giardino, C., Bresciani, M., Valentini, E., Gasperini, L., Bolpagni, R., and Brando, V. E.: Airborne hyperspectral data to assess suspended particulate matter and aquatic vegetation in a shallow and turbid lake, Remote Sensing of Environment, 157, 48–57, https://doi.org/10.1016/j.rse.2014.04.034, 2015.

Gleeson, D. F., Pappalardo, R. T., Grasby, S. E., Anderson, M. S., Beauchamp, B., Castaño, R., Chien, S. A., Doggett, T., Mandrake, L., and Wagstaff, K. L.: Characterization of a sulfur-rich Arctic spring site and field analog to Europa using hyperspectral data, Remote Sensing of Environment, 114, 1297–1311, https://doi.org/10.1016/j.rse.2010.01.011, 2010.

Goyens, C., Marty, S., Leymarie, E., Antoine, D., Babin, M., and Bélanger, S.: High Angular Resolution Measurements of the Anisotropy of Reflectance of Sea Ice and Snow, Earth and Space Science, 5, 30–47, https://doi.org/10.1002/2017EA000332, 2018.

Grenfell, C. G. and Maykut, G. a.: The optical properties of ice and snow in the Arctic Basin, Journal of Glaciology, 18, 445–463, 1977.

Grenfell, T. C.: A radiative transfer model for sea ice with vertical structure variations, Journal of Geophysical Research, 96, 16 991, https://doi.org/10.1029/91JC01595, 1991.

Grenfell, T. C. and Perovich, D. K.: Seasonal and spatial evolution of albedo in a snow-ice-land-ocean environment, Journal of Geophysical Research, 109, C01 001, https://doi.org/10.1029/2003JC001866, 2004.

Guanter, L.: New algorithms for atmospheric correction and retrieval of biophysical parameters in Earth Observation . Application to ENVISAT / MERIS data, Ph.D. thesis, Universitat de València, 2006.

Guanter, L., Kaufmann, H., Foerster, S., Brosinsky, A., Wulf, H., Bochow, M., Boesche, N., Brell, M., Buddenbaum, H., Chabrillat, S., Hank, T., Heiden, U., Heim, B., Heldens, W., Hill, J., Hollstein, A., Hostert, P., Krasemann, H., Leitão, P. J., van der Linden, S., Mauser, W., Mielke, C., Müller, A., Oppelt, N., Roessner, S., Röttgers, R., Schneiderhan, T., Staenz, K., and Segl, K.: EnMAP Science Plan. EnMAP Technical Report., Tech. rep., GFZ Data Services, https://doi.org/doi.org/10.2312/enmap.2016.006, 2016.

Han, H., Im, J., Kim, M., Sim, S., Kim, J., Kim, D.-j., and Kang, S.-H.: Retrieval of Melt Ponds on Arctic Multiyear Sea Ice in Summer from TerraSAR-X Dual-Polarization Data Using Machine Learning Approaches: A Case Study in the Chukchi Sea with Mid-Incidence Angle Data, Remote Sensing, 8, 57, https://doi.org/10.3390/rs8010057, 2016.

Han, Y., Gao, Y., Zhang, Y., Wang, J., and Yang, S.: Hyperspectral Sea Ice Image Classification Based on the Spectral-Spatial-Joint Feature with Deep Learning, Remote Sensing, 11, 2170, https://doi.org/10.3390/rs11182170, 2019.

Hanesiak, J. M., Barber, D. G., De Abreu, R. a., and Yackel, J. J.: Local and regional albedo observations of arctic first-year sea ice during melt ponding, Journal of Geophysical Research, 106, 1005, https://doi.org/10.1029/1999JC000068, 2001.

Hanson, K. J.: The Albedo of Sea-Ice and Ice Islands in the Arctic Ocean Basin, ARCTIC, 14, 188–196, https://doi.org/10.14430/arctic3673, 1961.

Harris Geospatial Solutions Inc.: Fast Line-of-sight Atmospheric Analysis of Hypercubes (FLAASH), URL `https://www.harrisgeospatial.com/docs/FLAASH.html`, [Date accessed: 2018-05-03], 2018.

Hattersley-Smith, G., Koenig, L., Greenaway, K., and Dunbar, M.: Arctic Ice Islands, ARCTIC, 5, https://doi.org/10.14430/arctic3901, 1952.

Heege, T., Hausknecht, P., and Kobryn, H.: Hyperspectral Seafloor Mapping and Direct Bathymetry Calculation Using Hymap Data From the Ningaloo Reef and Rottnest Island Areas in Western Australia, Imaging, pp. 1–8, 2007.

Heygster, G., Istomina, L., Zege, E., Malinka, A., and Prikhach, A.: H2020-EO-1-2014 New ideas for Earth-relevant space applications - SPICES - Space-borne observations for detecting and forecasting sea ice cover extremes - Deliverable: D5.5 - Albedo and MPF retrieval methodology using PM observations, Tech. Rep. Ref. Ares(2018)3690811 - 11/07/2018, University of Bremen, Bremen, 2020.

Hieronymi, M.: Monte Carlo code for the study of the dynamic light field at the wavy atmosphere-ocean interface, Journal of the European Optical Society: Rapid Publications, 8, 13 039, https://doi.org/10.2971/jeos.2013.13039, 2013.

Hieronymi, M.: Polarized reflectance and transmittance distribution functions of the ocean surface, Optics Express, 24, A1045, https://doi.org/10.1364/OE.24.0A1045, 2016.

Hieronymi, M., Müller, D., and Doerffer, R.: The OLCI Neural Network Swarm (ONNS): A Bio-Geo-Optical Algorithm for Open Ocean and Coastal Waters, Frontiers in Marine Science, 4, 1–18, https://doi.org/10.3389/fmars.2017.00140, 2017.

Hohenegger, C., Alali, B., Steffen, K. R., Perovich, D. K., and Golden, K. M.: Transition in the fractal geometry of Arctic melt ponds, The Cryosphere, 6, 1157–1162, https://doi.org/10.5194/tc-6-1157-2012, 2012.

Holben, B., Eck, T., Slutsker, I., Tanré, D., Buis, J., Setzer, A., Vermote, E., Reagan, J., Kaufman, Y. J., Nakajima, T., Lavenu, F., Jankowiak, I., and Smirnov, A.: AERONET—A Federated Instrument Network and Data Archive for Aerosol Characterization, Remote Sensing of Environment, 66, 1–16, https://doi.org/10.1016/S0034-4257(98)00031-5, 1998.

Holland, M. M., Bailey, D. A., Briegleb, B. P., Light, B., and Hunke, E.: Improved sea ice shortwave radiation physics in CCSM4: The impact of melt ponds and aerosols on Arctic sea ice, Journal of Climate, 25, 1413–1430, https://doi.org/10.1175/JCLI-D-11-00078.1, 2012.

Holt, B. and Digby, S. A.: Processes and imagery of first-year fast sea ice during the melt season, Journal of Geophysical Research, 90, 5045, https://doi.org/10.1029/JC090iC03p05045, 1985.

Horner, R., Ackley, S., Dieckmann, G., Gulliksen, B., Hoshiai, T., Legendre, L., Melnikov, I., Reeburgh, W., Spindler, M., and Sullivan, C.: Ecology of sea ice biota, Polar Biology, 12, 63–86, https://doi.org/10.1007/BF00243113, 1992.

Horvat, C., Jones, D. R., Iams, S., Schroeder, D., Flocco, D., and Feltham, D.: The frequency and extent of sub-ice phytoplankton blooms in the Arctic Ocean, Science Advances, 3, e1601 191, https://doi.org/10.1126/sciadv.1601191, 2017.

Horvat, C., Flocco, D., Rees Jones, D. W., Roach, L., and Golden, K. M.: The Effect of Melt Pond Geometry on the Distribution of Solar Energy Under First-Year Sea Ice, Geophysical Research Letters, 47, 1–10, https://doi.org/10.1029/2019GL085956, 2020.

Howell, S. E. L., Tivy, A., Yackel, J. J., and Scharien, R. K.: Application of a SeaWinds/QuikSCAT sea ice melt algorithm for assessing melt dynamics in the Canadian Arctic Archipelago, Journal of Geophysical Research, 111, C07 025, https://doi.org/10.1029/2005JC003193, 2006.

Howell, S. E. L., Scharien, R. K., Landy, J., and Brady, M.: Spring melt pond fraction in the Canadian Arctic Archipelago predicted from RADARSAT-2, The Cryosphere Discussions, pp. 1–24, https://doi.org/10.5194/tc-2020-171, 2020.

Huang, W., Lu, P., Lei, R., Xie, H., and Li, Z.: Melt pond distribution and geometry in high Arctic sea ice derived from aerial investigations, Annals of Glaciology, 57, 105–118, https://doi.org/10.1017/aog.2016.30, 2016.

Huck, P., Light, B., Eicken, H., and Haller, M.: Mapping sediment-laden sea ice in the Arctic using AVHRR remote-sensing data: Atmospheric correction and determination of reflectances as a function of ice type and sediment load, Remote Sensing of Environment, https://doi.org/10.1016/j.rse.2006.10.002, 2007.

Hunke, E. C., Hebert, D. A., and Lecomte, O.: Level-ice melt ponds in the Los Alamos sea ice model, CICE, Ocean Modelling, 71, 26–42, https://doi.org/10.1016/j.ocemod.2012.11.008, 2013.

Ibsen Photonics: FREEDOM VIS Product Sheet, URL `https://ibsen.com/wp-content/uploads/Ibsen-Product-Sheets-FREEDOM-VIS.pdf`, [Date accessed: 2019-06-04], 2019.

Inoue, J., Curry, J. A., and Maslanik, J. A.: Application of Aerosondes to Melt-Pond Observations over Arctic Sea Ice, Journal of Atmospheric and Oceanic Technology, 25, 327–334, https://doi.org/10.1175/2007JTECHA955.1, 2008a.

Inoue, J., Kikuchi, T., and Perovich, D. K.: Effect of heat transmission through melt ponds and ice on melting during summer in the Arctic Ocean, Journal of Geophysical Research: Oceans, 113, 1–13, https://doi.org/10.1029/2007JC004182, 2008b.

IOCCG: Atmospheric correction for remotely-sensed ocean-colour products, in: Reports of the International Ocean-Colour Coordinating Group, No. 10, edited by Wang, M., 10, Dartmouth, Canada, 2010.

IOCCG: Ocean Colour Remote Sensing in Polar Seas, in: Reports of the International Ocean-Colour Coordinating Group, No. 16, edited by Babin, M., Arrigo, K., Bélanger, S., and Forget, M.-H., 16, Dartmouth, Canada, 2015.

Istomina, L. and Heygster, G.: H2020-EO-1-2014 New ideas for Earth-relevant space applications - SPICES- Space-borne observations for detecting and forecasting sea ice cover extremes - Deliverable: D5.1 - Retrieval algorithm for albedo and meld pond fraction from Sentinel-3 observation, Tech. Rep. Ref. Ares(2017)1337082 - 15/03/2017, University of Bremen, Bremen, 2017.

Istomina, L., Heygster, G., Huntemann, M., Marks, H., Melsheimer, C., Zege, E., Malinka, A., Prikhach, A., and Katsev, I.: Melt pond fraction and spectral sea ice albedo retrieval from MERIS data - Part 2: Case studies and trends of sea ice albedo and melt ponds in the Arctic for years 2002-2011, Cryosphere, 9, 1567–1578, https://doi.org/10.5194/tc-9-1567-2015, 2015a.

Istomina, L., Heygster, G., Huntemann, M., Schwarz, P., Birnbaum, G., Scharien, R., Polashenski, C., Perovich, D., Zege, E., Malinka, A., Prikhach, A., and Katsev, I.: Melt pond fraction and spectral sea ice albedo retrieval from MERIS data - Part 1: Validation against in situ, aerial, and ship cruise data, Cryosphere, 9, 1551–1566, https://doi.org/10.5194/tc-9-1551-2015, 2015b.

Istomina, L., Melsheimer, C., Huntemann, M., and Nicolaus, M.: Retrieval of Sea Ice Thickness During Melt Season From in Situ , Airborne and Satellite Imagery, pp. 7678–7681, 2016.

Itoh, M., Inoue, J., Shimada, K., Zimmermann, S., Kikuchi, T., Hutchings, J., McLaughlin, F., and Carmack, E.: Acceleration of sea-ice melting due to transmission of solar radiation through ponded ice area in the Arctic Ocean: Results of in situ observations from icebreakers in 2006 and 2007, Annals of Glaciology, 52, 249–260, https://doi.org/10.3189/172756411795931471, 2011.

Jing, E. and Datt, B.: Detection of coastal bathymetry using hyperspectral imagery, in: OCEANS'10 IEEE SYDNEY, August 2008, pp. 1–4, IEEE, https://doi.org/10.1109/OCEANSSYD.2010.5603864, 2010.

Kim, D. J., Hwang, B., Chung, K. H., Lee, S. H., Jung, H. S., and Moon, W. M.: Melt pond mapping with high-resolution SAR: The first view, Proceedings of the IEEE, 101, 748–758, https://doi.org/10.1109/JPROC.2012.2226411, 2013.

Knust, R., Rex, M., Haas, C., Kanzow, T., and Wolf-Gladrow, D.: Expeditionsprogramm PS122 MOSAiC, p. 126, 2019.

Koenig, L., Martin, S., Studinger, M., and Sonntag, J.: Polar Airborne Observations Fill Gap in Satellite Data, Eos, Transactions American Geophysical Union, 91, 333–334, https://doi.org/10.1029/2010EO380002, 2010.

König, M. and Oppelt, N.: Optical measurements of bare ice and melt ponds on Arctic sea ice acquired during POLARSTERN cruise PS106, https://doi.org/doi.pangaea.de/10.1594/PANGAEA.908075, 2019.

König, M. and Oppelt, N.: A linear model to derive melt pond depth on Arctic sea ice from hyperspectral data, The Cryosphere, 14, 2567–2579, https://doi.org/10.5194/tc-14-2567-2020, 2020.

König, M., Hieronymi, M., and Oppelt, N.: Application of Sentinel-2 MSI in Arctic Research: Evaluating the Performance of Atmospheric Correction Approaches Over Arctic Sea Ice, Frontiers in Earth Science, 7, 1–18, https://doi.org/10.3389/feart.2019.00022, 2019.

König, M., Birnbaum, G., and Oppelt, N.: Mapping the Bathymetry of Melt Ponds on Arctic Sea Ice Using Hyperspectral Imagery, Remote Sensing, 12, 2623, https://doi.org/10.3390/rs12162623, 2020a.

König, M., Wagner, M. P., and Oppelt, N.: Ice floe tracking with Sentinel-2, in: Remote Sensing of the Ocean, Sea Ice, Coastal Waters, and Large Water Regions 2020, edited by Bostater, C. R., Neyt, X., and Viallefont-Robinet, F., vol. 1152908, p. 6, SPIE, https://doi.org/10.1117/12.2573427, 2020b.

Kupiszewski, P., Leck, C., Tjernström, M., Sjogren, S., Sedlar, J., Graus, M., Müller, M., Brooks, B., Swietlicki, E., Norris, S., and Hansel, A.: Vertical profiling of aerosol particles and trace gases over the central Arctic Ocean during summer, Atmospheric Chemistry and Physics, 13, 12 405–12 431, https://doi.org/10.5194/acp-13-12405-2013, 2013.

Kutner, M. H., Li, W., Nachtsheim, C. J., and Neter, J.: Applied Linear Statistical Models, fifth edit edn., 2004.

Kvålseth, T. O.: Cautionary Note about R 2, The American Statistician, 39, 279–285, https://doi.org/10.1080/00031305.1985.10479448, 1985.

Kwok, R.: Arctic sea ice thickness, volume, and multiyear ice coverage: Losses and coupled variability (1958-2018), Environmental Research Letters, 13, https://doi.org/10.1088/1748-9326/aae3ec, 2018.

Kwok, R. and Untersteiner, N.: The thinning of Arctic sea ice, Physics Today, 64, 36–41, https://doi.org/10.1063/1.3580491, 2011.

Kwok, R., Cunningham, G. F., Wensnahan, M., Rigor, I., Zwally, H. J., and Yi, D.: Thinning and volume loss of the Arctic Ocean sea ice cover: 2003-2008, Journal of Geophysical Research: Oceans, 114, 1–16, https://doi.org/10.1029/2009JC005312, 2009.

Labsphere: Spectralon Targets, URL `https://www.labsphere.com/labsphere-products-solutions/materials-coatings-2/targets-standards/test-child/`, [Date accessed: 2018-05-24].

Landy, J., Ehn, J., Shields, M., and Barber, D.: Surface and melt pond evolution on landfast first-year sea ice in the Canadian Arctic Archipelago, Journal of Geophysical Research: Oceans, 119, 3054–3075, https://doi.org/10.1002/2013JC009617, 2014.

Landy, J. C., Ehn, J. K., and Barber, D. G.: Albedo feedback enhanced by smoother Arctic sea ice, Geophysical Research Letters, 42, 10 714–10 720, https://doi.org/10.1002/2015GL066712, 2015.

Langleben, M.: Albedo of Melting Sea Ice in the Southern Beaufort Sea, Journal of Glaciology, 10, 101–104, https://doi.org/10.3189/S0022143000013022, 1971.

Langleben, M. P.: Albedo and Degree of Puddling of a Melting Cover of Sea Ice, Journal of Glaciology, 8, 407–412, https://doi.org/10.3189/S002214300002699X, 1969.

Lecomte, O., Fichefet, T., Vancoppenolle, M., and Nicolaus, M.: A new snow thermodynamic scheme for large-scale sea-ice models, Annals of Glaciology, 52, 337–346, https://doi.org/10.3189/172756411795931453, 2011.

Lecomte, O., Fichefet, T., Flocco, D., Schroeder, D., and Vancoppenolle, M.: Interactions between wind-blown snow redistribution and melt ponds in a coupled ocean–sea ice model, Ocean Modelling, 87, 67–80, https://doi.org/10.1016/j.ocemod.2014.12.003, 2015.

Lee, S., Stroeve, J., Tsamados, M., and Khan, A. L.: Machine learning approaches to retrieve pan-Arctic melt ponds from visible satellite imagery, Remote Sensing of Environment, 247, 111 919, https://doi.org/10.1016/j.rse.2020.111919, 2020.

Lee, S. H., Joo, H. M., Liu, Z., Chen, J., and He, J.: Phytoplankton productivity in newly opened waters of the Western Arctic Ocean, Deep-Sea Research Part II: Topical Studies in Oceanography, 81-84, 18–27, https://doi.org/10.1016/j.dsr2.2011.06.005, 2012.

Legleiter, C. J., Roberts, D. A., and Lawrence, R. L.: Spectrally based remote sensing of river bathymetry, Earth Surface Processes and Landforms, 34, 1039–1059, https://doi.org/10.1002/esp.1778, 2009.

Legleiter, C. J., Tedesco, M., Smith, L. C., Behar, A. E., and Overstreet, B. T.: Mapping the bathymetry of supraglacial lakes and streams on the Greenland ice sheet using field measurements and high-resolution satellite images, The Cryosphere, 8, 215–228, https://doi.org/10.5194/tc-8-215-2014, 2014.

Legleiter, C. J., Overstreet, B. T., Glennie, C. L., Pan, Z., Fernandez-Diaz, J. C., and Singhania, A.: Evaluating the capabilities of the CASI hyperspectral imaging system and Aquarius bathymetric LiDAR for measuring channel morphology in two distinct river environments, Earth Surface Processes and Landforms, 41, 344–363, https://doi.org/10.1002/esp.3794, 2016.

Li, Q., Zhou, C., Zheng, L., Liu, T., and Yang, X.: Monitoring evolution of melt ponds on first-year and multiyear sea ice in the Canadian Arctic Archipelago with optical satellite data, Annals of Glaciology, https://doi.org/10.1017/aog.2020.24, 2020.

Li, Y., Chen, J., Ma, Q., Zhang, H. K., and Liu, J.: Evaluation of Sentinel-2A Surface Reflectance Derived Using Sen2Cor in North America, IEEE Journal of Selected Topics in Applied Earth Observations and Remote Sensing, 11, 1997–2021, https://doi.org/10.1109/JSTARS.2018.2835823, 2018.

Light, B., Eicken, H., Maykut, G. a., and Grenfell, T. C.: The effect of included particulates on the spectral albedo of sea ice, Journal of Geophysical Research, 103, 27 739–27 752, https://doi.org/10.1029/98jc02587, 1998.

Light, B., Grenfell, T. C., and Perovich, D. K.: Transmission and absorption of solar radiation by Arctic sea ice during the melt season, Journal of Geophysical Research: Oceans, 113, 1–19, https://doi.org/10.1029/2006JC003977, 2008.

Light, B., Perovich, D. K., Webster, M. A., Polashenski, C., and Dadic, R.: Optical properties of melting first-year Arctic sea ice, Journal of Geophysical Research: Oceans, 120, 7657–7675, https://doi.org/10.1002/2015JC011163, 2015.

Lin, L., He, J., Zhang, F., Cao, S., and Zhang, C.: Algal bloom in a melt pond on Canada Basin pack ice, Polar Record, 52, 114–117, https://doi.org/10.1017/S0032247415000510, 2016.

Liu, J., Song, M., Horton, R. M., and Hu, Y.: Revisiting the potential of melt pond fraction as a predictor for the seasonal Arctic sea ice extent minimum, Environmental Research Letters, 10, 054 017, https://doi.org/10.1088/1748-9326/10/5/054017, 2015.

Liu, Q., Zhang, Y., Lv, Q., and Shang, L.: Applying High-Resolution Visible Imagery to Satellite Melt Pond Fraction Retrieval: A Neural Network Approach, Satellite Oceanography and Meteorology, 3, 1–5, https://doi.org/10.18063/som.v3i3.692, 2017.

Liu, Y., Key, J. R., and Wang, X.: Influence of changes in sea ice concentration and cloud cover on recent Arctic surface temperature trends, Geophysical Research Letters, 36, 1–6, https://doi.org/10.1029/2009GL040708, 2009.

Loncan, L., De Almeida, L. B., Bioucas-Dias, J. M., Briottet, X., Chanussot, J., Dobigeon, N., Fabre, S., Liao, W., Licciardi, G. A., Simoes, M., Tourneret, J. Y., Veganzones, M. A., Vivone, G., Wei, Q., and Yokoya, N.: Hyperspectral Pansharpening: A Review, IEEE Geoscience and Remote Sensing Magazine, 3, 27–46, https://doi.org/10.1109/MGRS.2015.2440094, 2015.

Lu, P., Li, Z., Cheng, B., Lei, R., and Zhang, R.: Sea ice surface features in Arctic summer 2008: Aerial observations, Remote Sensing of Environment, 114, 693–699, https://doi.org/10.1016/j.rse.2009.11.009, 2010.

Lu, P., Leppäranta, M., Cheng, B., and Li, Z.: Influence of melt-pond depth and ice thickness on Arctic sea-ice albedo and light transmittance, Cold Regions Science and Technology, 124, 1–10, https://doi.org/10.1016/j.coldregions.2015.12.010, 2016.

Lu, P., Leppäranta, M., Cheng, B., Li, Z., Istomina, L., and Heygster, G.: The color of melt ponds on Arctic sea ice, The Cryosphere, 12, 1331–1345, https://doi.org/10.5194/tc-12-1331-2018, 2018.

Lyzenga, D. R.: Shallow-water bathymetry using combined lidar and passive multispectral scanner data, International Journal of Remote Sensing, 6, 115–125, https://doi.org/10.1080/01431168508948428, 1985.

Ma, S., Tao, Z., Yang, X., Yu, Y., Zhou, X., and Li, Z.: Bathymetry Retrieval From Hyperspectral Remote Sensing Data in Optical-Shallow Water, IEEE Transactions on Geoscience and Remote Sensing, 52, 1205–1212, https://doi.org/10.1109/TGRS.2013.2248372, 2014.

Ma, Y., Xu, N., Liu, Z., Yang, B., Yang, F., Wang, X. H., and Li, S.: Satellite-derived bathymetry using the ICESat-2 lidar and Sentinel-2 imagery datasets, Remote Sensing of Environment, 250, 112 047, https://doi.org/10.1016/j.rse.2020.112047, 2020.

Macdonald, R. W., Carmack, E. C., McLaughlin, F. A., Falkner, K. K., and Swift, J. H.: Connections among ice, runoff and atmospheric forcing in the Beaufort Gyre, Geophysical Research Letters, 26, 2223–2226, https://doi.org/10.1029/1999GL900508, 1999.

Macke, A. and Flores, H.: The Expeditions PS106/1 and 2 of the Research Vessel POLARSTERN to the Arctic Ocean in 2017, Reports on Polar and Marine Research, 719, https://doi.org/doi.org/10.2312/BzPM{_}0719{_}2018, 2018.

Magruder, L., Neumann, T., Fricker, H., Farrell, S., Brunt, K., Gardner, A., Hancock, D., Harbeck, K., Jasinski, M., Kwok, R., Kurtz, N., Lee, J., Markus, T., Morison, J., Neuenschwander, A., Palm, S., Popescu, S., Smith, B., and Yang, Y.: New Earth Orbiter Provides a Sharper Look at a Changing Planet, Eos, 100, https://doi.org/10.1029/2019EO133233, 2019.

Mahiny, A. S. and Turner, B. J.: A Comparison of Four Common Atmospheric Correction Methods, Photogrammetric Engineering & Remote Sensing, 73, 361–368, https://doi.org/10.14358/PERS.73.4.361, 2007.

Makshtas, A. P. and Podgorny, I. A.: Calculation of melt pond albedos on Arctic sea ice, Polar Research, 15, 43–52, https://doi.org/10.3402/polar.v15i1.6635, 1996.

Makynen, M., Kern, S., Rosel, A., and Pedersen, L. T.: On the Estimation of Melt Pond Fraction on the Arctic Sea Ice With ENVISAT WSM Images, IEEE Transactions on Geoscience and Remote Sensing, 52, 7366–7379, https://doi.org/10.1109/TGRS.2014.2311476, 2014.

Mäkynen, M., Haapala, J., Aulicino, G., Balan-Sarojini, B., Balmaseda, M., Gegiuc, A., Girard-Ardhuin, F., Hendricks, S., Heygster, G., Istomina, L., Kaleschke, L., Karvonen, J., Krumpen, T., Lensu, M., Mayer, M., Parmiggiani, F., Ricker, R., Rinne, E., Schmitt, A., Similä, M., Tietsche, S., Tonboe, R., Wadhams, P., Winstrup, M., and Zuo, H.: Satellite Observations for Detecting and Forecasting Sea-Ice Conditions: A Summary of

Advances Made in the SPICES Project by the EU's Horizon 2020 Programme, Remote Sensing, 12, 1214, https://doi.org/10.3390/rs12071214, 2020.

Malenovský, Z., Rott, H., Cihlar, J., Schaepman, M. E., García-Santos, G., Fernandes, R., and Berger, M.: Sentinels for science: Potential of Sentinel-1, -2, and -3 missions for scientific observations of ocean, cryosphere, and land, Remote Sensing of Environment, 120, 91–101, https://doi.org/10.1016/j.rse.2011.09.026, 2012.

Malinka, A., Zege, E., Heygster, G., and Istomina, L.: Reflective properties of white sea ice and snow, The Cryosphere, 10, 2541–2557, https://doi.org/10.5194/tc-10-2541-2016, 2016.

Malinka, A., Zege, E., Istomina, L., Heygster, G., Spreen, G., Perovich, D., and Polashenski, C.: Reflective properties of melt ponds on sea ice, The Cryosphere, 12, 1921–1937, https://doi.org/10.5194/tc-12-1921-2018, 2018.

Markelin, L., Honkavaara, E., Takala, T., Schläpfer, D., Suomalainen, J., and Pellikka, P.: A Novel Approach for the Radiometric Correction of Airborne Hyperspectral Image Data, ISPRS, 3, 1451–1460, https://doi.org/10.5167/uzh-75102, 2012.

Markus, T., Cavalieri, D. J., and Ivanoff, A.: The potential of using Landsat 7 ETM+ for the classification of sea-ice surface conditions during summer, Annals of Glaciology, 34, 415–419, https://doi.org/10.3189/172756402781817536, 2002.

Markus, T., Cavalieri, D. J., Tschudi, M. A., and Ivanoff, A.: Comparison of aerial video and Landsat 7 data over ponded sea ice, Remote Sensing of Environment, 86, 458–469, https://doi.org/10.1016/S0034-4257(03)00124-X, 2003.

Markus, T., Stroeve, J. C., and Miller, J.: Recent changes in Arctic sea ice melt onset, freezeup, and melt season length, Journal of Geophysical Research: Oceans, 114, 1–14, https://doi.org/10.1029/2009JC005436, 2009.

Martins, V. S., Barbosa, C. C. F., de Carvalho, L. A. S., Jorge, D. S. F., Lobo, F. d. L., and de Moraes Novo, E. M. L.: Assessment of atmospheric correction methods for sentinel-2 MSI images applied to Amazon floodplain lakes, Remote Sensing, 9, https://doi.org/10.3390/rs9040322, 2017.

Maslanik, J., Curry, J., Drobot, S., and Holland, G.: Observations of sea ice using a low cost unpiloted aerial vehicle, 16th IAHR International Symposium on Ice, p. 6, 2002.

Maslanik, J., Drobot, S., Fowler, C., Emery, W., and Barry, R.: On the Arctic climate paradox and the continuing role of atmospheric circulation in affecting sea ice conditions, Geophysical Research Letters, 34, 2–5, https://doi.org/10.1029/2006GL028269, 2007.

Maslanik, J., Stroeve, J., Fowler, C., and Emery, W.: Distribution and trends in Arctic sea ice age through spring 2011, Geophysical Research Letters, 38, 2–7, https://doi.org/10.1029/2011GL047735, 2011.

Maslowski, W., Clement Kinney, J., Higgins, M., and Roberts, A.: The Future of Arctic Sea Ice, Annual Review of Earth and Planetary Sciences, 40, 625–654, https://doi.org/10.1146/annurev-earth-042711-105345, 2012.

McIntyre, M. L., Naar, D. F., Carder, K. L., Donahue, B. T., and Mallinson, D. J.: Coastal Bathymetry from Hyperspectral Remote Sensing Data: Comparisons with High Resolution Multibeam Bathymetry, Marine Geophysical Researches, 27, 129–136, https://doi.org/10.1007/s11001-005-0266-y, 2006.

Meier, W. N. and Markus, T.: Remote sensing of sea ice, in: Remote Sensing of the Cryosphere, edited by Tedesco, M., chap. 11, John Wiley & Sons, Ltd, Chichester, UK, https://doi.org/10.1002/9781118368909, 2015.

Miao, X., Xie, H., Ackley, S. F., Perovich, D. K., and Ke, C.: Object-based detection of Arctic sea ice and melt ponds using high spatial resolution aerial photographs, Cold Regions Science and Technology, 119, 211–222, https://doi.org/10.1016/j.coldregions.2015.06.014, 2015.

Mingfeng, W., Jie, S. U., Tao, L. I., Xiaoyu, W., Qing, J. I., and Yong, C. A. O.: Determination of Arctic melt pond fraction and sea ice roughness from Unmanned Aerial Vehicle (UAV) imagery, Advances in Polar Science, 29, 181–189, https://doi.org/10.13679/j.advps.2018.3.00181, 2018.

Mishra, D. R., Ogashawara, I., and Gitelson, A. A.: Bio-optical Modeling and Remote Sensing of Inland Waters, Elsevier, Oxford, 2017.

Mobley, C. D.: Estimation of the remote-sensing reflectance from above-surface measurements, Applied Optics, 38, 7442, https://doi.org/10.1364/AO.38.007442, 1999.

Mobley, C. D.: Polarized reflectance and transmittance properties of windblown sea surfaces, Applied Optics, 54, 4828, https://doi.org/10.1364/AO.54.004828, 2015.

Mobley, C. D., Boss, E., and Roesler, C.: Ocean Optics Web Book, URL `http://www.oceanopticsbook.info/`, [Date accessed: 2018-05-17], 2018.

Morassutti, M. P. and Ledrew, E. F.: Albedo and depth of melt ponds on sea-ice, International Journal of Climatology, 16, 817–838, 1996.

Mortin, J., Howell, S. E., Wang, L., Derksen, C., Svensson, G., Graversen, R. G., and Schrøder, T. M.: Extending the QuikSCAT record of seasonal melt-freeze transitions over arctic sea ice using ASCAT, Remote Sensing of Environment, 141, 214–230, https://doi.org/10.1016/j.rse.2013.11.004, 2014.

Moussavi, M., Pope, A., Halberstadt, A. R. W., Trusel, L. D., Cioffi, L., and Abdalati, W.: Antarctic Supraglacial Lake Detection Using Landsat 8 and Sentinel-2 Imagery: Towards Continental Generation of Lake Volumes, Remote Sensing, 12, 134, https://doi.org/10.3390/rs12010134, 2020.

Moussavi, M. S., Abdalati, W., Pope, A., Scambos, T., Tedesco, M., MacFerrin, M., and Grigsby, S.: Derivation and validation of supraglacial lake volumes on the Greenland Ice Sheet from high-resolution satellite imagery, Remote Sensing of Environment, 183, 294–303, https://doi.org/10.1016/j.rse.2016.05.024, 2016.

Müller-Wilm, U.: Sentinel-2 MSI – Level-2A Prototype Processor Installation and User Manual, European Space Agency, (Special Publication) ESA SP, 49, 1–51, 2016.

NASA Goddard Space Flight Center: AERONET MARITIME AEROSOL NETWORK, URL `https://aeronet.gsfc.nasa.gov/new_web/maritime_aerosol_network.html`, [Date accessed: 2018-11-19], 2017.

Nasonova, S., Scharien, R., Haas, C., and Howell, S.: Linking Regional Winter Sea Ice Thickness and Surface Roughness to Spring Melt Pond Fraction on Landfast Arctic Sea Ice, Remote Sensing, 10, 37, https://doi.org/10.3390/rs10010037, 2017.

National Snow & Ice Data Center: Lingering seashore days, URL `https://nsidc.org/arcticseaicenews/2020/10/lingering-seashore-days/`, [Date accessed: 2020-11-05], 2020a.

National Snow & Ice Data Center: Arctic sea ice decline stalls out at second lowest minimum, URL `https://nsidc.org/arcticseaicenews/2020/09/arctic-sea-ice-decline-stalls-out-at-second-lowest-minimum/`, [Date accessed: 2020-08-21], 2020b.

Nghiem, S. V., Rigor, I. G., Perovich, D. K., Clemente-Colón, P., Weatherly, J. W., and Neumann, G.: Rapid reduction of Arctic perennial sea ice, Geophysical Research Letters, 34, 1–6, https://doi.org/10.1029/2007GL031138, 2007.

Nicolaus, M., Gerland, S., Hudson, S. R., Hanson, S., Haapala, J., and Perovich, D. K.: Seasonality of spectral albedo and transmittance as observed in the Arctic Transpolar Drift in 2007, Journal of Geophysical Research: Oceans, 115, 1–21, https://doi.org/10.1029/2009JC006074, 2010.

Nicolaus, M., Katlein, C., Maslanik, J., and Hendricks, S.: Changes in Arctic sea ice result in increasing light transmittance and absorption, Geophysical Research Letters, 39, 2012GL053 738, https://doi.org/10.1029/2012GL053738, 2012.

Niroumand-Jadidi, M., Bovolo, F., Bruzzone, L., and Gege, P.: Physics-based Bathymetry and Water Quality Retrieval Using PlanetScope Imagery: Impacts of 2020 COVID-19

Lockdown and 2019 Extreme Flood in the Venice Lagoon, Remote Sensing, 12, 2381, https://doi.org/10.3390/rs12152381, 2020.

Notz, D. and Stroeve, J.: Observed Arctic sea-ice loss directly follows anthropogenic CO2 emission, Science, 354, 747–750, https://doi.org/10.1126/science.aag2345, 2016.

Notz, D. and Stroeve, J.: The Trajectory Towards a Seasonally Ice-Free Arctic Ocean, Current Climate Change Reports, 4, 407–416, https://doi.org/10.1007/s40641-018-0113-2, 2018.

Ocean Optics: STS-VIS SPECS, URL `https://oceanoptics.com/product/sts-vis-microspectrometer/#tab-specifications`, [Date accessed: 2019-03-26], 2019.

Ogashawara, I., Mishra, D. R., and Gitelson, A. A.: Remote Sensing of Inland Waters: Background and Current State-of-the-Art, in: Bio-optical Modeling and Remote Sensing of Inland Waters, edited by Mishra, D. R., Ogashawara, I., and Gitelson, A. A., chap. 1, Elsevier, Oxford, 2017.

Olsen, M. S., Callaghan, T. V., Reist, J. D., Reiersen, L. O., Dahl-Jensen, D., Granskog, M. A., Goodison, B., Hovelsrud, G. K., Johansson, M., Kallenborn, R., Key, J., Klepikov, A., Meier, W., Overland, J. E., Prowse, T. D., Sharp, M., Vincent, W. F., and Walsh, J.: The changing arctic cryosphere and likely consequences: An overview, Ambio, 40, 111–118, https://doi.org/10.1007/s13280-011-0220-y, 2011.

Painter, T. H. and Dozier, J.: The effect of anisotropic reflectance on imaging spectroscopy of snow properties, Remote Sensing of Environment, 89, 409–422, https://doi.org/10.1016/j.rse.2003.09.007, 2004.

Palmer, M. A., Saenz, B. T., and Arrigo, K. R.: Impacts of sea ice retreat, thinning, and melt-pond proliferation on the summer phytoplankton bloom in the Chukchi Sea, Arctic Ocean, Deep Sea Research Part II: Topical Studies in Oceanography, 105, 85–104, https://doi.org/10.1016/j.dsr2.2014.03.016, 2014.

Parrish, C. E., Magruder, L. A., Neuenschwander, A. L., Forfinski-Sarkozi, N., Alonzo, M., and Jasinski, M.: Validation of ICESat-2 ATLAS bathymetry and analysis of ATLAS's bathymetric mapping performance, Remote Sensing, 11, https://doi.org/10.3390/rs11141634, 2019.

Pedersen, C. A., Roeckner, E., Lüthje, M., and Winther, J.: A new sea ice albedo scheme including melt ponds for ECHAM5 general circulation model, Journal of Geophysical Research, 114, D08 101, https://doi.org/10.1029/2008JD010440, 2009.

Pedregosa, F., Varoquaux, G., Gramfort, A., Michel, V., Thirion, B., Grisel, O., Blondel, M., Prettenhofer, P., Weiss, R., Dubourg, V., Vanderplas, J., Passos, A., Cournapeau, D., Brucher, M., Perrot, M., and Duchesnay, E.: Scikit-learn: Machine Learning in {P}ython, Journal of Machine Learning Research, 12, 2825–2830, 2011.

Peltoniemi, J. I., Kaasalainen, S., Näränen, J., Matikainen, L., and Piironen, J.: Measurement of directional and spectral signatures of light reflectance by snow, IEEE Transactions on Geoscience and Remote Sensing, 43, 2294–2304, https://doi.org/10.1109/TGRS.2005.855131, 2005.

Perovich, D. K.: Optical Properties of Sea Ice, Physics of ice-covered seas, 1, 195–230, 1998.

Perovich, D. K.: Seasonal evolution of the albedo of multiyear Arctic sea ice, Journal of Geophysical Research, 107, 1–13, https://doi.org/10.1029/2000JC000438, 2002.

Perovich, D. K. and Grenfell, T. C.: A Theoretical Model of Radiative Transfer in Young Sea Ice, Journal of Glaciology, 28, 341–356, https://doi.org/10.1017/S0022143000011680, 1982.

Perovich, D. K. and Polashenski, C.: Albedo evolution of seasonal Arctic sea ice, Geophysical Research Letters, 39, 1–6, https://doi.org/10.1029/2012GL051432, 2012.

Perovich, D. K. and Richter-Menge, J. A.: Surface characteristics of lead ice, Journal of Geophysical Research, 99, 16 341–16 350, https://doi.org/10.1029/94JC01194, 1994.

Perovich, D. K. and Tucker, W. B.: Arctic sea-ice conditions and the distribution of solar radiation during summer, Annals of Glaciology, 25, 445–450, https://doi.org/10.3189/S0260305500014439, 1997.

Perovich, D. K., Roesler, C. S., and Pegau, W. S.: Variability in Arctic sea ice optical properties, Journal of Geophysical Research: Oceans, 103, 1193–1208, https://doi.org/10.1029/97JC01614, 1998.

Perovich, D. K., Tucker, W. B., and Ligett, K. A.: Aerial observations of the evolution of ice surface conditions during summer, Journal of Geophysical Research: Oceans, 107, 8048, https://doi.org/10.1029/2000JC000449, 2002.

Perovich, D. K., Grenfell, T. C., Light, B., Elder, B. C., Harbeck, J., Polashenski, C., Tucker, W. B., and Stelmach, C.: Transpolar observations of the morphological properties of Arctic sea ice, Journal of Geophysical Research, 114, C00A04, https://doi.org/10.1029/2008JC004892, 2009.

Perovich, D. K., Jones, K. F., Light, B., Eicken, H., Markus, T., Stroeve, J., and Lindsay, R.: Solar partitioning in a changing Arctic sea-ice cover, Annals of Glaciology, 52, 192–196, https://doi.org/10.3189/172756411795931543, 2011.

Petrich, C., Eicken, H., Polashenski, C. M., Sturm, M., Harbeck, J. P., Perovich, D. K., and Finnegan, D. C.: Snow dunes: A controlling factor of melt pond distribution on Arctic sea ice, Journal of Geophysical Research: Oceans, 117, n/a–n/a, https://doi.org/10.1029/2012JC008192, 2012.

Petty, A. A., Bagnardi, M., Kurtz, N., Tilling, R., Fons, S., Armitage, T., Horvat, C., and Kwok, R.: Assessment of ICESat-2 sea ice surface classification with Sentinel-2 imagery: implications for freeboard and new estimates of lead and floe geometry, Earth and Space Science, 2, https://doi.org/10.1029/2020EA001491, 2021.

Pflug, B., Bieniarz, J., Debaecker, V., Louis, J., and Müller-Wilm, U.: Some Experience Using SEN2COR Mission Performance Centre, 2016.

Philpot, W. D.: Bathymetric mapping with passive multispectral imagery, Applied Optics, 28, 1569, https://doi.org/10.1364/ao.28.001569, 1989.

Pithan, F. and Mauritsen, T.: Arctic amplification dominated by temperature feedbacks in contemporary climate models, Nature Geoscience, 7, 181–184, https://doi.org/10.1038/ngeo2071, 2014.

Planet: New Year, New Launches: 48 SuperDoves To Launch With SpaceX, URL `https://www.planet.com/pulse/new-year-new-launches-48-superdoves-to-launch-with-spacex/`, [Date accessed: 2021-02-02], 2021a.

Planet: Why Planet?, URL `https://www.planet.com/why-planet/`, [Date accessed: 2021-01-30], 2021b.

Podgorny, I. A. and Grenfell, T. C.: Partitioning of solar energy in melt ponds from measurements of pond albedo and depth, Journal of Geophysical Research: Oceans, 101, 22 737–22 748, https://doi.org/10.1029/96JC02123, 1996.

Polashenski, C., Perovich, D., and Courville, Z.: The mechanisms of sea ice melt pond formation and evolution, Journal of Geophysical Research: Oceans, 117, 1–23, https://doi.org/10.1029/2011JC007231, 2012.

Pope, A., Rees, W. G., Fox, A. J., and Fleming, A.: Open access data in polar and cryospheric remote sensing, Remote Sensing, 6, 6183–6220, https://doi.org/10.3390/rs6076183, 2014.

Pope, A., Scambos, T. A., Moussavi, M., Tedesco, M., Willis, M., Shean, D., and Grigsby, S.: Estimating supraglacial lake depth in West Greenland using Landsat 8 and comparison with other multispectral methods, The Cryosphere, 10, 15–27, https://doi.org/10.5194/tc-10-15-2016, 2016.

Pope, R. M. and Fry, E. S.: Absorption spectrum (380–700 nm) of pure water II Integrating cavity measurements, Applied Optics, 36, 8710, https://doi.org/10.1364/AO.36.008710, 1997.

Pozyx NV: Pozyx, URL `https://www.pozyx.io/`, [Date accessed: 2020-05-26], 2020.

Richards, F. J.: A Flexible Growth Function for Empirical Use, Journal of Experimental Botany, 10, 290–301, https://doi.org/10.1093/jxb/10.2.290, 1959.

Richter, R. and Schläpfer, D.: Atmospheric / Topographic Correction for Airborne Imagery, 2015.

Richter, R. and Schläpfer, D.: Atmospheric / Topographic Correction for Satellite Imagery (ATCOR - 2/3 User Guide), in: ATCOR-2/3 User Guide, Version 9.1.2, January, pp. 1–71, 2017.

Richter, R., Bachmann, M., Dorigo, W., and Müller, A.: Influence of the adjacency effect on ground reflectance measurements, IEEE Geoscience and Remote Sensing Letters, 3, 565–569, https://doi.org/10.1109/LGRS.2006.882146, 2006.

Roeckner, E., Mauritsen, T., Esch, M., and Brokopf, R.: Impact of melt ponds on Arctic sea ice in past and future climates as simulated by MPI-ESM, Journal of Advances in Modeling Earth Systems, 4, 1989–1995, https://doi.org/10.1029/2012MS000157, 2012.

Rösel, A.: Detection of Melt Ponds on Arctic Sea Ice with Optical Satellite Data, vol. 25 of *Hamburg Studies on Maritime Affairs*, Springer Berlin Heidelberg, Berlin, Heidelberg, https://doi.org/10.1007/978-3-642-37033-5, 2013.

Rösel, A. and Kaleschke, L.: Comparison of different retrieval techniques for melt ponds on Arctic sea ice from Landsat and MODIS satellite data, Annals of Glaciology, 52, 185–191, https://doi.org/10.3189/172756411795931606, 2011.

Rösel, A., Kaleschke, L., and Birnbaum, G.: Melt ponds on Arctic sea ice determined from MODIS satellite data using an artificial neural network, The Cryosphere, 6, 431–446, https://doi.org/10.5194/tc-6-431-2012, 2012.

Rösel, A., King, J., Doulgeris, A. P., Wagner, P. M., Johansson, A. M., and Gerland, S.: Can we extend local sea-ice measurements to satellite scale? An example from the N-ICE2015 expedition, Annals of Glaciology, pp. 1–10, https://doi.org/10.1017/aog.2017.37, 2017.

Röttgers, R. and Doerffer, R.: Measurements of optical absorption by chromophoric dissolved organic matter using a point-source integrating-cavity absorption meter, Limnology and Oceanography: Methods, 5, 126–135, https://doi.org/10.4319/lom.2007.5.126, 2007.

Röttgers, R., Doxaran, D., and Dupouy, C.: Quantitative filter technique measurements of spectral light absorption by aquatic particles using a portable integrating cavity absorption meter (QFT-ICAM), Optics Express, 24, A1, https://doi.org/10.1364/OE.24.0000A1, 2016.

Rozell, N.: Encounters with Northern Sea Ice, in: Field Techniques for Sea Ice Research, edited by Eicken, H., Gradinger, R., Salganek, M., Shirasawa, K., Perovich, D., and Leppäranta, M., chap. Foreword, University of Alaska Press, Fairbanks, 2010.

Sankelo, P., Haapala, J., Heiler, I., and Rinne, E.: Melt pond formation and temporal evolution at the drifting station Tara during summer 2007, Polar Research, 29, 311–321, https://doi.org/10.1111/j.1751-8369.2010.00161.x, 2010.

Scharien, R. and Yackel, J.: Analysis of surface roughness and morphology of first-year sea ice melt ponds: implications for microwave scattering, IEEE Transactions on Geoscience and Remote Sensing, 43, 2927–2939, https://doi.org/10.1109/TGRS.2005.857896, 2005.

Scharien, R. K., Hochheim, K., Landy, J., and Barber, D. G.: First-year sea ice melt pond fraction estimation from dual-polarisation C-band SAR – Part 2: Scaling in situ to Radarsat-2, The Cryosphere, 8, 2163–2176, https://doi.org/10.5194/tc-8-2163-2014, 2014.

Scharien, R. K., Segal, R., Yackel, J. J., Howell, S. E., and Nasonova, S.: Linking winter and spring thermodynamic sea-ice states at critical scales using an object-based image analysis of Sentinel-1, Annals of Glaciology, 59, 148–162, https://doi.org/10.1017/aog.2017.43, 2018.

Schmithüsen, H.: Continuous meteorological surface measurement during POLARSTERN cruise PS106.1 (ARK-XXXI/1.1), https://doi.org/10.1594/PANGAEA.886302, 2018.

Schröder, D., Feltham, D. L., Flocco, D., and Tsamados, M.: September Arctic sea-ice minimum predicted by spring melt-pond fraction, Nature Climate Change, 4, 353–357, https://doi.org/10.1038/nclimate2203, 2014.

scikit-learn developers: Mean squared error, URL `https://scikit-learn.org/stable/modules/model_evaluation.html#mean-squared-error`, [Date accessed: 2019-02-13], 2018a.

scikit-learn developers: R^2 score, the coefficient of determination, URL `https://scikit-learn.org/stable/modules/model_evaluation.html#r2-score`, [Date accessed: 2019-02-13], 2018b.

Scott, F. and Feltham, D. L.: A model of the three-dimensional evolution of Arctic melt ponds on first-year and multiyear sea ice, Journal of Geophysical Research: Oceans, https://doi.org/10.1029/2010JC006156, 2010.

Seabold, S. and Perktold, J.: Statsmodels: Econometric and statistical modeling with python, in: 9th Python in Science Conference, 2010.

Serreze, M. C., Holland, M. M., and Stroeve, J.: Perspectives on the Arctic's Shrinking Sea-Ice Cover, Science, 315, 1533–1536, https://doi.org/10.1126/science.1139426, 2007.

Shokr, M. and Sinha, N.: Sea Ice, vol. 209 of *Geophysical Monograph Series*, John Wiley & Sons, Inc, Hoboken, NJ, https://doi.org/10.1002/9781119028000, 2015.

Skyllingstad, E. D., Paulson, C. A., and Perovich, D. K.: Simulation of melt pond evolution on level ice, Journal of Geophysical Research: Oceans, 114, 1–15, https://doi.org/10.1029/2009JC005363, 2009.

Sneed, W. A. and Hamilton, G. S.: Evolution of melt pond volume on the surface of the Greenland Ice Sheet, Geophysical Research Letters, 34, 4–7, https://doi.org/10.1029/2006GL028697, 2007.

Sneed, W. A. and Hamilton, G. S.: Validation of a method for determining the depth of glacial melt ponds using satellite imagery, Annals of Glaciology, 52, 15–22, https://doi.org/10.3189/172756411799096240, 2011.

Specim Spectral Imaging Ltd.: , URL `https://www.specim.fi/`, [Date accessed: 2020-08-07].

Steinmetz, F. and Ramon, D.: Sentinel-2 MSI and Sentinel-3 OLCI consistent ocean colour products using POLYMER, in: Remote Sensing of the Open and Coastal Ocean and Inland Waters, edited by Frouin, R. J. and Murakami, H., p. 13, SPIE, https://doi.org/10.1117/12.2500232, 2018.

Steinmetz, F., Deschamps, P.-Y., and Ramon, D.: Atmospheric correction in presence of sun glint: application to MERIS, Optics Express, 19, 9783, https://doi.org/10.1364/OE.19.009783, 2011.

Sterckx, S., Knaeps, E., Adriaensen, S., Reusen, I., Keukelaere, L. D., and Hunter, P.: Opera : an Atmospheric Correction for Land and Water, Proceedings of the Sentinel-3 for Science Workshop, pp. 3–6, 2015a.

Sterckx, S., Knaeps, S., Kratzer, S., and Ruddick, K.: SIMilarity Environment Correction (SIMEC) applied to MERIS data over inland and coastal waters, Remote Sensing of Environment, 157, 96–110, https://doi.org/10.1016/j.rse.2014.06.017, 2015b.

Stroeve, J. and Notz, D.: Changing state of Arctic sea ice across all seasons, Environmental Research Letters, 13, https://doi.org/10.1088/1748-9326/aade56, 2018.

Stroeve, J., Holland, M. M., Meier, W., Scambos, T., and Serreze, M.: Arctic sea ice decline: Faster than forecast, Geophysical Research Letters, 34, 1–5, https://doi.org/10.1029/2007GL029703, 2007.

Studinger, M., Koenig, L., Martin, S., and Sonntag, J.: Operation icebridge: Using instrumented aircraft to bridge the observational gap between icesat and icesat-2, in: 2010 IEEE International Geoscience and Remote Sensing Symposium, pp. 1918–1919, IEEE, https://doi.org/10.1109/IGARSS.2010.5650555, 2010.

Sturm, M.: Winter snow cover on the sea ice of the Arctic Ocean at the Surface Heat Budget of the Arctic Ocean (SHEBA): Temporal evolution and spatial variability, Journal of Geophysical Research, 107, 8047, https://doi.org/10.1029/2000JC000400, 2002.

Sturm, M., Holmgren, J., and Perovich, D. K.: Winter snow cover on the sea ice of the Arctic Ocean at the Surface Heat Budget of the Arctic Ocean (SHEBA): Temporal evolution and spatial variability, J. Geophys. Res, 107, https://doi.org/10.1029/2000JC000400, 2000.

Tanaka, Y.: Estimating Meltwater Drainage Onset Timing and Duration of Landfast Ice in the Canadian Arctic Archipelago Using AMSR-E Passive Microwave Data, Remote Sensing, 12, 1033, https://doi.org/10.3390/rs12061033, 2020.

Tanaka, Y., Tateyama, K., Kameda, T., and Hutchings, J. K.: Estimation of melt pond fraction over high-concentration Arctic sea ice using AMSR-E passive microwave data, Journal of Geophysical Research: Oceans, 121, 7056–7072, https://doi.org/10.1002/2016JC011876, 2016.

Taskjelle, T., Hudson, S. R., Granskog, M. A., and Hamre, B.: Modelling radiative transfer through ponded first-year Arctic sea ice with a plane-parallel model, Cryosphere, 11, 2137–2148, https://doi.org/10.5194/tc-11-2137-2017, 2017.

Taylor, P. D.: A model of melt pond evolution on sea ice, Journal of Geophysical Research, 109, C12 007, https://doi.org/10.1029/2004JC002361, 2004.

Tedesco, M. and Steiner, N.: In-situ multispectral and bathymetric measurements over a supraglacial lake in western Greenland using a remotely controlled watercraft, Cryosphere, https://doi.org/10.5194/tc-5-445-2011, 2011.

The Scipy community: scipy.optimize.curve_fit, URL `https://docs.scipy.org/doc/scipy/reference/generated/scipy.optimize.curve_fit.html`, [Date accessed: 2019-07-11], 2019a.

The Scipy community: scipy.signal.savgol_filter, URL `https://docs.scipy.org/doc/scipy/reference/generated/scipy.signal.savgol_filter.html?highlight=savgol#scipy.signal.savgol_filter`, [Date accessed: 2019-06-26], 2019b.

The Scipy community: scipy.stats.pearsonr, URL `https://docs.scipy.org/doc/scipy/reference/generated/scipy.stats.pearsonr.html`, [Date accessed: 2019-02-13], 2019c.

Thomas, D. N., Cottier, F. R., and Brandon, M. A.: Sea Ice, Ice Drift, and Oceanic Circulation, in: International Encyclopedia of Geography, pp. 1–10, Wiley, https://doi.org/10.1002/9781118786352.wbieg0395.pub2, 2019.

Thompson, D. R., Seidel, F. C., Gao, B. C., Gierach, M. M., Green, R. O., Kudela, R. M., and Mouroulis, P.: Optimizing irradiance estimates for coastal and inland water imaging spectroscopy, Geophysical Research Letters, 42, 4116–4123, https://doi.org/10.1002/2015GL063287, 2015.

Tilling, R., Kurtz, N. T., Bagnardi, M., Petty, A. A., and Kwok, R.: Detection of Melt Ponds on Arctic Summer Sea Ice From ICESat-2, Geophysical Research Letters, 47, 1–10, https://doi.org/10.1029/2020GL090644, 2020.

Tomasi, C., Vitale, V., Lupi, A., Di Carmine, C., Campanelli, M., Herber, A., Treffeisen, R., Stone, R. S., Andrews, E., Sharma, S., Radionov, V., von Hoyningen-Huene, W., Stebel, K., Hansen, G. H., Myhre, C. L., Wehrli, C., Aaltonen, V., Lihavainen, H., Virkkula, A., Hillamo, R., Ström, J., Toledano, C., Cachorro, V. E., Ortiz, P., de Frutos, A. M., Blindheim, S., Frioud, M., Gausa, M., Zielinski, T., Petelski, T., and Yamanouchi, T.: Aerosols in polar regions: A historical overview based on optical depth and in situ observations, Journal of Geophysical Research Atmospheres, 112, https://doi.org/10.1029/2007JD008432, 2007.

Tomasi, C., Lupi, A., Mazzola, M., Stone, R. S., Dutton, E. G., Herber, A., Radionov, V. F., Holben, B. N., Sorokin, M. G., Sakerin, S. M., Terpugova, S. A., Sobolewski, P. S., Lanconelli, C., Petkov, B. H., Busetto, M., and Vitale, V.: An update on polar aerosol optical properties using POLAR-AOD and other measurements performed during the International Polar Year, Atmospheric Environment, 52, 29–47, https://doi.org/10.1016/j.atmosenv.2012.02.055, 2012.

Transon, J., D'Andrimont, R., Maugnard, A., and Defourny, P.: Survey of current hyperspectral Earth observation applications from space and synergies with Sentinel-2, in: 2017 9th International Workshop on the Analysis of Multitemporal Remote Sensing Images (MultiTemp), December 2016, pp. 1–8, IEEE, https://doi.org/10.1109/Multi-Temp.2017.8035244, 2017.

Transon, J., D'Andrimont, R., Maugnard, A., and Defourny, P.: Survey of Hyperspectral Earth Observation Applications from Space in the Sentinel-2 Context, Remote Sensing, 10, 157, https://doi.org/10.3390/rs10020157, 2018.

Tsamados, M., Feltham, D., Petty, A., Schroeder, D., and Flocco, D.: Processes controlling surface, bottom and lateral melt of Arctic sea ice in a state of the art sea icemodel, Philosophical Transactions of the Royal Society A: Mathematical, Physical and Engineering Sciences, 373, https://doi.org/10.1098/rsta.2014.0167, 2015.

Tschudi, M. A., Curry, J. A., and Maslanik, J. A.: Determination of areal surface-feature coverage in the Beaufort Sea using aircraft video data, Annals of Glaciology, 25, 434–438, https://doi.org/10.3189/S0260305500014415, 1997.

Tschudi, M. A., Curry, J. A., and Maslanik, J. A.: Airborne observations of summertime surface features and their effect on surface albedo during FIRE/SHEBA, Journal of Geophysical Research: Atmospheres, 106, 15 335–15 344, https://doi.org/10.1029/2000JD900275, 2001.

Tschudi, M. A., Maslanik, J. A., and Perovich, D. K.: Derivation of melt pond coverage on Arctic sea ice using MODIS observations, Remote Sensing of Environment, 112, 2605–2614, https://doi.org/10.1016/j.rse.2007.12.009, 2008.

Tucker, W. B., Gow, A. J., Meese, D. A., Bosworth, H. W., and Reimnitz, E.: Physical characteristics of summer sea ice across the Arctic Ocean, Journal of Geophysical Research: Oceans, 104, 1489–1504, https://doi.org/10.1029/98JC02607, 1999.

Untersteiner, N.: On the mass and heat budget of arctic sea ice, Archiv für Meteorologie, Geophysik und Bioklimatologie Serie A, 12, 151–182, https://doi.org/10.1007/BF02247491, 1961.

Uttal, T., Curry, J. A., Mcphee, M. G., Perovich, D. K., Moritz, R. E., Maslanik, J. A., Guest, P. S., Stern, H. L., Moore, J. A., Turenne, R., Heiberg, A., Serreze, M. C., Wylie, D. P., Persson, O. G., Paulson, C. A., Halle, C., Morison, J. H., Wheeler, P. A., Makshtas, A., Welch, H., Shupe, M. D., Intrieri, J. M., Stamnes, K., Lindsey, R. W., Pinkel, R., Pegau, W. S., Stanton, T. P., and Grenfeld, T. C.: Surface Heat Budget of the Arctic Ocean, Bulletin of the American Meteorological Society, 83, 255–275, https://doi.org/10.1175/1520-0477(2002)083⟨0255:SHBOTA⟩2.3.CO;2, 2002.

Vanhellemont, Q.: ACOLITE Python User Manual, RBINS, 2018.

Vanhellemont, Q.: Adaptation of the dark spectrum fitting atmospheric correction for aquatic applications of the Landsat and Sentinel-2 archive, Remote Sensing of Environment, 225, submitted, https://doi.org/10.1016/j.rse.2019.03.010, 2019.

Vanhellemont, Q. and Ruddick, K.: Advantages of high quality SWIR bands for ocean colour processing: Examples from Landsat-8, Remote Sensing of Environment, 161, 89–106, https://doi.org/10.1016/j.rse.2015.02.007, 2015.

Vanhellemont, Q. and Ruddick, K.: Atmospheric correction of metre-scale optical satellite data for inland and coastal water applications, Remote Sensing of Environment, 216, 586–597, https://doi.org/10.1016/j.rse.2018.07.015, 2018.

Vermote, E. F., Tanré, D., Deuzé, J. L., Herman, M., and Morcrette, J.-J.: Second {S}imulation of the {S}atellite {S}ignal in the {S}olar {S}pectrum, 6{S}: an overview, IEEE Transactions on Geoscience and Remote Sensing, 35, 675–686, https://doi.org/10.1109/36.581987, 1997.

Vihma, T.: Effects of Arctic Sea Ice Decline on Weather and Climate: A Review, vol. 35, https://doi.org/10.1007/s10712-014-9284-0, 2014.

Vihma, T., Tisler, P., and Uotila, P.: Atmospheric forcing on the drift of Arctic sea ice in 1989-2009, Geophysical Research Letters, 39, 1–6, https://doi.org/10.1029/2011GL050118, 2012.

VITO: iCOR plugin for SNAP toolbox, SOFTWARE USER MANUAL, VERSION 1.0, 2017.

Wang, M., Su, J., Landy, J., Leppäranta, M., and Guan, L.: A New Algorithm for Sea Ice Melt Pond Fraction Estimation From High-Resolution Optical Satellite Imagery, Journal of Geophysical Research: Oceans, 125, 1–14, https://doi.org/10.1029/2019JC015716, 2020.

Warren, S. G.: Optical Properties of Snow, Review of Geophysics and Space Physics, 20, 67–89, 1982.

Watts, A. C., Ambrosia, V. G., and Hinkley, E. A.: Unmanned Aircraft Systems in Remote Sensing and Scientific Research: Classification and Considerations of Use, Remote Sensing, 4, 1671–1692, https://doi.org/10.3390/rs4061671, 2012.

Webster, M. A., Rigor, I. G., Perovich, D. K., Richter-Menge, J. A., Polashenski, C. M., and Light, B.: Seasonal evolution of melt ponds on Arctic sea ice, Journal of Geophysical Research: Oceans, 120, 5968–5982, https://doi.org/10.1002/2015JC011030, 2015.

Wright, N. C. and Polashenski, C. M.: Open-source algorithm for detecting sea ice surface features in high-resolution optical imagery, The Cryosphere, 12, 1307–1329, https://doi.org/10.5194/tc-12-1307-2018, 2018.

Wright, N. C. and Polashenski, C. M.: How Machine Learning and High-Resolution Imagery Can Improve Melt Pond Retrieval From MODIS Over Current Spectral Unmixing Techniques, Journal of Geophysical Research: Oceans, 125, 1–17, https://doi.org/10.1029/2019JC015569, 2020.

Wright, N. C., Polashenski, C. M., McMichael, S. T., and Beyer, R. A.: Observations of sea ice melt from Operation IceBridge imagery, The Cryosphere, 14, 3523–3536, https://doi.org/10.5194/tc-14-3523-2020, 2020.

Yackel, J. J., Barber, D. G., and Hanesiak, J. M.: Melt ponds on sea ice in the Canadian Archipelago: 1. Variability in morphological and radiative properties, Journal of Geophysical Research, 105, 22 049, https://doi.org/10.1029/2000JC900075, 2000.

Yackel, J. J., Nandan, V., Mahmud, M., Scharien, R., Kang, J. W., and Geldsetzer, T.: A spectral mixture analysis approach to quantify Arctic first-year sea ice melt pond fraction using QuickBird and MODIS reflectance data, Remote Sensing of Environment, 204, 704–716, https://doi.org/10.1016/j.rse.2017.09.030, 2017.

Yuan, S., Gu, W., Liu, C., and Xie, F.: Towards a semi-empirical model of the sea ice thickness based on hyperspectral remote sensing in the Bohai Sea, Acta Oceanologica Sinica, 36, 80–89, https://doi.org/10.1007/s13131-017-0996-0, 2017.

Zege, E., Malinka, A., Katsev, I., Prikhach, A., Heygster, G., Istomina, L., Birnbaum, G., and Schwarz, P.: Algorithm to retrieve the melt pond fraction and the spectral albedo of Arctic summer ice from satellite optical data, Remote Sensing of Environment, 163, 153–164, https://doi.org/10.1016/j.rse.2015.03.012, 2015.

Zhang, J., Schweiger, A., Webster, M., Light, B., Steele, M., Ashjian, C., Campbell, R., and Spitz, Y.: Melt Pond Conditions on Declining Arctic Sea Ice Over 1979–2016: Model Development, Validation, and Results, Journal of Geophysical Research: Oceans, 123, 7983–8003, https://doi.org/10.1029/2018JC014298, 2018.

Zhong, Y., Wang, X., Xu, Y., Wang, S., Jia, T., Hu, X., Zhao, J., Wei, L., and Zhang, L.: Mini-UAV-Borne Hyperspectral Remote Sensing: From Observation and Processing to Applications, IEEE Geoscience and Remote Sensing Magazine, 6, 46–62, https://doi.org/10.1109/MGRS.2018.2867592, 2018.

Declaration of Authorship

Hiermit erkläre ich an Eides statt, dass ich die vorliegende Dissertation, abgesehen von der Beratung durch meine Betreuer*innen, nach Inhalt und Form selbständig verfasst habe und keine weiteren Quellen und Hilfsmittel als die hier angegebenen verwendet habe. Diese Arbeit hat weder ganz noch in Teilen bereits an anderer Stelle im Rahmen eines Prüfungsverfahrens vorgelegen. Als kumulative Dissertation sind Kapitel 2 bis 4 wie zu Beginn der Kapitel vermerkt in den genannten Zeitschriften veröffentlicht. Ich erkläre, dass die vorliegende Arbeit unter Einhaltung der Regeln guter wissenschaftlicher Praxis der Deutschen Forschungsgemeinschaft entstanden ist. Ich versichere, dass mir kein akademischer Grad entzogen wurde.

Kiel, den 15.02.2021